



TECHNISCHE
UNIVERSITÄT
WIEN



TRIGA
CENTER
Atominstitut

DIPLOMARBEIT

Identification, extraction, and analysis of Cs-bearing microparticles from Fukushima

zur Erlangung des akademischen Grades

Diplom-Ingenieur

im Rahmen des Studiums

Physikalische Energie- und Messtechnik

eingereicht von

Matthias Rosezky, BSc BSc

Matrikelnummer 11814559

ausgeführt am TRIGA Center Atominstitut
der Fakultät für Physik der Technischen Universität Wien

Betreuung

Betreuer: Univ.Prof. Mag.rer.nat. Dr.techn. Georg Steinhauser

Mitwirkung: -/-

Wien, 18. Dezember 2024

(Unterschrift Verfasser)

(Unterschrift Betreuer)



Die approbierte gedruckte Originalversion dieser Diplomarbeit ist an der TU Wien Bibliothek verfügbar
The approved original version of this thesis is available in print at TU Wien Bibliothek.

Erklärung zur Verfassung der Arbeit

Matthias Rosezky, BSc BSc

Hiermit erkläre ich, dass ich diese Arbeit selbständig verfasst habe, dass ich die verwendeten Quellen und Hilfsmittel vollständig angegeben habe und dass ich die Stellen der Arbeit – einschließlich Tabellen, Karten und Abbildungen –, die anderen Werken oder dem Internet im Wortlaut oder dem Sinn nach entnommen sind, auf jeden Fall unter Angabe der Quelle als Entlehnung kenntlich gemacht habe.

Wien, 18. Dezember 2024

(Unterschrift Verfasser)

Kurzfassung

Nach mehreren Explosionen im Kernkraftwerk Fukushima Daiichi ([Fukushima Daiichi Nuclear Power Plant \(FDNPP\)](#)) nach dem schweren Erdbeben und Tsunami vom 11. März 2011 wurden große Mengen radioaktiven Materials in der Umwelt verteilt. Dazu gehören die bei einem derartigen Unfall typischerweise erwarteten kurzlebigen und flüchtigen Isotope wie ^{131}I und ^{133}Xe , aber auch ^{134}Cs und ^{137}Cs , die wesentlich längere Halbwertszeiten aufweisen.

Eine besondere Art der Kontamination sind die sogenannten Cs-Mikropartikel ([caesium microparticles \(CsMPs\)](#)). Wie bereits in mehreren Publikationen beschrieben, sind diese Kontaminationen reich an Cäsium, insbesondere an den beiden Isotopen ^{134}Cs und ^{137}Cs , und weisen typischerweise eine abgerundete oder sogar kugelförmige Gestalt auf. Der Ursprung dieser Mikropartikel ist bis heute nicht vollständig geklärt, aber es wird angenommen, dass sie sich in den [high-efficiency particulate air \(HEPA\)](#)- und [pre-HEPA](#)-Filtern der Reaktorgebäude während der Explosionen gebildet haben könnten. Die Fasern dieser Filter könnten zusammen mit dem freigesetzten radioaktiven Cäsium geschmolzen sein, was ihre runde Form erklären würde. Es wurde zudem festgestellt, dass sie zu einem großen Teil aus Silicium bestehen, was durch die mineralischen Fasern der Filter erklärt werden könnte. Außerdem wurden einige Mikropartikel gefunden, die große Mengen an oberflächlichem Kohlenstoff enthalten, der möglicherweise von Aktivkohlefiltern stammt. Ihre genauen Ursprünge sind jedoch noch nicht bestätigt.

Angesichts ihrer geringen Größe (bis maximal wenige hundert Mikrometer) konnten sie große Entfernungen in der japanischen Landschaft von ihrem Ursprung im Kernkraftwerk zurücklegen und sogar verschlossene Gebäude im Innenbereich kontaminieren. Abhängig von den Eigenschaften jedes einzelnen Mikropartikels, wie Größe, Form, Aktivität und dem Verhältnis von $^{134}\text{Cs}/^{137}\text{Cs}$, wurde ein System zur Kategorisierung etabliert und in einigen Veröffentlichungen weiterentwickelt, um die Ursprünge dieser Partikel zu identifizieren. Angesichts der charakteristischen Eigenschaften der Partikel wurde versucht, die genaue Quelle der Partikel im [FDNPP](#) zu bestimmen. Derartige umweltforensische Methoden ermöglichen es, das Ausmaß der Kontamination weiter zu erforschen und die Hintergründe des Unfalls zu entschlüsseln.

In der vorliegenden Arbeit wurden Proben untersucht, die Jahre nach dem Reaktorunfall in [FDNPP](#) gesammelt wurden. Eine Probe ist ein Stück einer Fleecejacke, das 2015 aus einem versperrten Haus innerhalb der Evakuierungszone nordwestlich des [FDNPP](#) entnommen wurde. Die anderen Proben sind mehrere passive Luftprobenehmer, die konzipiert waren, Staub und andere Aerosole ohne Stromzufuhr einzusammeln. Sie wurden speziell dafür entwickelt, radioaktive Partikel aus der Luft zu fangen, die selbst Jahre nach dem Unfall noch resuspendiert werden können. Diese wurden in der Nähe des [FDNPP](#) für mehrere Monate aufgestellt und im Jahr 2023 eingesammelt. In dieser Arbeit werden die Ergebnisse zu den identifizierten Isotopen, der Aktivität und Verteilung der Radionuklide auf diesen Proben anhand von autoradiographischen Aufnahmen und Low-Level-Gammaspektrometrie präsentiert. Zusätzlich wurde in Zusammenarbeit mit der Universitären Serviceeinrichtung für Transmissionselektronenmikroskopie ([University Service Facility for Transmission Electron Microscopy \(USTEM\)](#)) an der TU Wien versucht, Kandidaten für einzelne Cs-Mikropartikel in den Proben zu finden und zu extrahieren.

Abstract

Following several explosions at the [Fukushima Daiichi Nuclear Power Plant \(FDNPP\)](#), after the severe earthquake and tsunami on March 11, 2011, large quantities of radioactive material were dispersed into the environment. This included the short-lived and volatile isotopes typically expected in such an accident, such as ^{131}I and ^{133}Xe , but also ^{134}Cs and ^{137}Cs , which have much longer half-lives.

A special type of contamination are the so-called [caesium microparticles \(CsMPs\)](#). As already described in several publications, these contaminations are rich in cesium, especially in the two isotopes ^{134}Cs and ^{137}Cs , and typically have a rounded or even spherical shape. The origin of these microparticles has not yet been fully clarified, but it is assumed that they could have formed in the [high-efficiency particulate air \(HEPA\)](#) and pre-HEPA filters of the reactor buildings during the explosions. The fibers of these filters could have melted together with the released radioactive cesium, which would explain their round shape. They were also found to be largely made of silicon, which could be explained by the mineral fibers of the filters. In addition, some microparticles were found to contain large amounts of surface carbon, possibly originating from activated carbon filters. However, their exact origins have not yet been confirmed.

Given their small size (up to a few hundred micrometers at most), they could travel great distances in the Japanese landscape from their origin in the nuclear power plant and even contaminate sealed buildings indoors. Depending on the characteristics of each microparticle, such as size, shape, activity and the ratio of $^{134}\text{Cs}/^{137}\text{Cs}$, a system of categorization was established and further developed in some publications to identify the origins of these particles. Given the characteristic properties of the particles, attempts were made to determine the exact source of the particles in the [FDNPP](#). Such environmental forensic methods allow the extent of the contamination to be further investigated and the background to the accident to be deciphered.

In this thesis, samples collected years after the reactor accident at [FDNPP](#) were examined. One sample is a piece of a fleece jacket collected in 2015 from a locked house within the evacuation zone northwest of [FDNPP](#). The other samples are several passive air samplers designed to collect dust and other aerosols without power. They were specifically designed to capture radioactive particles from the air, which can be resuspended even years after the accident. These were placed near [FDNPP](#) for several months and collected in 2023. In this paper, the results of the identified isotopes, the activity and distribution of the radionuclides on these samples are presented on the basis of autoradiographic images and low-level gamma spectrometry. In addition, in collaboration with the [University Service Facility for Transmission Electron Microscopy \(USTEM\)](#) at TU Wien, an attempt was made to find and extract candidates for individual Cs microparticles in the samples.

Acknowledgments

First and foremost, I have to thank my family for supporting me through all of my studies and helping me wherever they can regardless of the circumstances. Without my parents and my sister, I certainly would not have been able to get into the position that I am in now. Thanks for fostering an environment where the pursue of knowledge is valued and thanks for putting up with me over the years, enduring all the weird things that I worked on.

Needless to say, my sincere thanks also go to Georg Steinhauser for allowing me the opportunity to work on this project in the first place, immediately accepting me as a member of his team, and the outstandingly pleasant working atmosphere he always cared for, despite me refusing to call him *sensei*. I can hardly imagine a better environment in which to work on a thesis like this. Who knows where I would be now without finding his course on radioecology by pure chance only a year after him returning to Vienna from Hannover.

I also have to thank Katsumi Shozugawa from the University of Tokyo as well as Bin Feng from Fudan University, and generally known to be a genius, for leaving me the honor to investigate all of the interesting samples that you provided the group with. Being able to investigate a piece of fleece preserved like in a time capsule with the fallout from 2011 after more than a decade is a privilege. After meeting Katsumi personally, I can only appreciate his enthusiasm for the subject, cheerful nature and the help he gives to his fellow citizens. Greetings to both of you in Japan and China!

My thanks are also due to the entire CLIP group at the TRIGA Center Atominstitut for all of their help and guidance, as well as the great environment they provided. I would also like to mentioned the other group members, Dominik, Nedim, Lukas, and Thomas, with whom it was a blast to work with.

Special thanks also go to Dieter Hainz and Monika Veit from the radiation protection of the [Atominstitut \(ATI\)](#) in all the help and assistance they provided me in regards to the gamma spectrometric measurements, as well as allowing me to spontaneously borrow their detector for extended amounts of time. They also endured their fair share of questions about all of the different things they were working on.

In addition to this, I would like to express my gratitude to Johannes Bernardi from the [USTEM](#) for connecting me with Jakob Gruber, who I have spent quite a substantial amount of time with in the search for [CsMPs](#). I cannot appreciate enough all of the work done by Jakob with regard to the competent operation of the devices and the extraction of the samples. Also thanks for all the insights into practical electron microscopy and the great atmosphere during our sessions. It still amazes me to see what kind of precision work is possible with the right people and the right tools.

Last but not least, I want to mention Carl Auer von Welsbach who probably provided the initial spark for my interest in radioactivity by contaminating an area of land close to my home around the year 1900, that was partially re-discovered by my father over a hundred years later. I also want to mention the great CosmicWatch project by Spencer Axani et al. that was the final straw to get into this field by using his device as an inspiration for my own gamma spectrometer and launching a small project of my own in late 2020. The things I have learned through this certainly are invaluable and I want to highlight each and every curious person I have had the pleasure of exchanging ideas and working with over the past years. This applies in particular to Holger Hartmann, Robert Düring, and Kian Shaker.



Die approbierte gedruckte Originalversion dieser Diplomarbeit ist an der TU Wien Bibliothek verfügbar
The approved original version of this thesis is available in print at TU Wien Bibliothek.

Contents

Kurzfassung	iii
Abstract	v
Acknowledgments	vii
Contents	ix
Acronyms	xi
List of Figures	xiii
List of Tables	xv
1 Introduction	1
1.1 Overview of the FDNPP Site and Facility	1
1.2 The 2011 FDNPP Nuclear Accident	6
1.2.1 Onset of the Accident	8
1.2.2 Progression of the Accident	9
1.2.3 Releases of Radionuclides	13
1.3 Radioactive Particles in the Environment	16
1.3.1 Overview	16
1.3.2 Particle Characterization	16
1.3.3 Dosimetric Aspects	19
1.3.4 Nuclear Weapons Tests	20
1.3.5 Nuclear Weapons Accidents	22
1.3.6 Chernobyl Nuclear Accident	23
1.3.7 Fukushima Nuclear Accident	24
1.3.8 Other NPP Accidents	26
1.3.9 Releases from Reprocessing Plants	27
1.3.10 NORM Sources	28
1.4 CsMPs from the FDNPP Nuclear Accident	29
1.4.1 Overview and Types	29
1.4.2 Cs-134/Cs-137 Ratio	34
1.4.3 Assumed Origins	35
1.4.4 Formation Mechanism	36
1.4.5 Current State of Research	39
2 Materials and Methods	41
2.1 Samples	41
2.1.1 Namie Fleece Coat	41
2.1.2 Passive Air Samplers	42
2.2 Experimental Details	44
2.2.1 Experimental Equipment	44
2.2.2 Experimental Procedure	48
2.2.3 Experimental Challenges	52
3 Results	55
3.1 Namie Fleece Coat	56
3.1.1 Sample 1.1.P.1.2 – Part 1/2	60
3.1.2 Sample 1.1.P.1.2 – Part 2/2	63
3.1.3 Sample F.1.3.1.3.1	64

3.1.4	Sample 1.4.P.1.1.1	65
3.1.5	Sample 1.4.P.1.1.2	68
3.1.6	Sample C.2.1.1.2	72
3.2	Passive Air Samplers	73
3.2.1	Sample PS.B.P.1	74
4	Conclusion	80
	References	83
A	Analyses at the USTEM	89
A.1	Namie Fleece Coat	89
A.1.1	Sample 1.1.P.1.2 – Part 1/2	89
A.1.2	Sample 1.1.P.1.2 – Part 2/2	91
A.1.3	Sample F.1.3.1.3.1	94
A.1.4	Sample 1.4.P.1.1.1	96
A.1.5	Sample 1.4.P.1.1.2	100
A.1.6	Sample C.2.1.1.2	101
A.2	Passive Air Samplers	104
A.2.1	Sample PS.B.P.1	104

Acronyms

- AIP** autoradiographic imaging plate. 45–47, 49–51, 53, 55–58, 64, 65, 73–75, 80, 81
- AMAD** activity median aerodynamic diameter. 25
- ATI** Atominstitut. vii, 41, 42, 44–46, 48, 49, 52, 66, 78, 81
- BWR** boiling water reactor. 1–4
- CEZ** Chernobyl exclusion zone. 23, 24
- CsMP** caesium microparticle. iii, v, vii, 1, 25, 26, 29–34, 36, 38–41, 49, 51–55, 57, 60, 61, 65–68, 70, 71, 76, 78, 80–82, 89, 97–99, 104
- DW** dry well. 4, 5, 10, 12
- EDG** emergency diesel generator. 5, 6, 8–12
- EDX** energy-dispersive X-ray spectroscopy. 19, 29, 32, 33, 48, 52–54, 58, 60, 61, 63–66, 68, 70, 72, 76, 78, 79, 81, 89–107
- FDNPP** Fukushima Daiichi Nuclear Power Plant. iii, v, 1–10, 12–15, 24–26, 29–31, 34–41, 44, 52, 80, 82
- FIB** focused ion beam. 19, 46, 48, 52, 58, 60, 63, 74, 81
- GE** General Electric. 2–4
- HEPA** high-efficiency particulate air. iii, v, 29, 30, 35–39, 53, 80
- HPGe** high-purity germanium. 17, 44, 45
- IAEA** International Atomic Energy Agency. 1, 5, 16
- IC** isolation cooler. 8, 9
- INES** International Nuclear Event Scale. 23, 24, 27
- JST** Japan Standard Time. 6, 25, 26
- LOCA** loss of coolant accident. 5, 27, 38
- LOOP** loss of offsite power. 5, 8
- MCCI** molten core concrete interactions. 39, 40
- MDA** minimum detectable activity. 61, 66, 69, 74, 78
- MSIV** main steam isolation valve. 8, 9
- MUWC** make-up water condensate. 9, 11
- NORM** naturally occurring radioactive material. 16, 28
- NPP** nuclear power plant. 8, 12, 14

- PCV** primary containment vessel. 4, 5, 8–12
- PUF** polyurethane foam. 43–45, 55, 73–75, 77, 80, 81
- PWR** pressurized water reactor. 1, 3, 27
- RB** reactor building. 4, 5, 9–12, 29, 30, 35, 38–40, 44, 80
- RCIC** reactor core isolation cooling. 8–10, 12
- RPV** reactor pressure vessel. 3–5, 8, 10, 12, 38, 80
- SBO** station blackout. 5, 6, 9, 10, 12
- SC** suppression chamber. 4, 5, 8, 10–12
- SEM** scanning electron microscope. 19, 23, 24, 27–29, 36, 46, 48, 51–54, 58–60, 63, 64, 74, 81, 89
- SFP** spent fuel pool. 6, 8, 9, 12
- SGTS** standby gas treatment system. 5, 11, 29, 35–40
- SRV** safety relief valve. 10–12
- TEM** transmission electron microscope. 19
- TEPCO** Tokyo Electric Power Company Holdings, Incorporated. 1, 11, 12
- UHS** ultimate heat sink. 9
- USTEM** University Service Facility for Transmission Electron Microscopy. iii, v, vii, 41, 46, 48, 49, 51, 52, 58–60, 63, 64, 72, 74, 81, 89
- WDX** wavelength-dispersive X-ray spectroscopy. 19
- XAS** X-ray absorption spectroscopy. 19
- XRD** X-ray diffraction. 19
- XRF** X-ray fluorescence. 19

List of Figures

1	Overview of all Japanese NPPs and Fukushima Daiichi	1
2	Schematic diagram of the BWR design	2
3	Overview of all Japanese NPPs and Fukushima Daiichi	4
4	Overview of the main accident sequence	7
5	Overview of the isolated core cooling systems	9
6	Schematic of the containment venting system	10
7	Deposition density of ^{137}Cs on land	13
8	Deposition density of ^{137}Cs in the Pacific	14
9	Self-absorption of different Pu particle sizes in tissue	20
10	SEM images of fuel particles found in Chornobyl's Red Forest	23
11	SEM images of fuel particles found in Chornobyl	23
12	Overview of the particle sizes found at FDNPP	25
13	Aerosol emission shortly after the accident	26
14	SEM images of typical Yenisei fuel particles	28
15	Backscatter electron images of representative radioactive CsMPs	31
16	Micro-beam maps of elemental distributions on a CsMP	31
17	EDX spectra of representative particles	32
18	Secondary electron images of three CsMPs	32
19	Secondary electron images of isolated CsMPs	33
20	$^{134}\text{Cs}+^{137}\text{Cs}$ deposition over a 3-km area	34
21	SEM image of a CsMP with fibrous surface feature	36
22	Images of HEPA filters and prefilters	37
23	Type A particle formation mechanism	37
24	HEPA setup in the SGTS lines	38
25	Type A formation process revised	40
26	Geographic origins and extraction pattern of the fleece sample	41
27	Photos of the Namie fleece coat sample	42
28	Passive air sampler schematics	43
29	Photos of passive sampler disks	43
30	Photo of the PUF sampling location	44
31	Photos of the gamma spectrometry and FIB SEM setups	46
32	Selection of imaging plates	47
33	Experimental procedure schematic	49
34	Example of the three-step fractionation process	50
35	Sample AIP self-absorption test	56
36	Rare AIP labeling artifact	56
37	AIP images of the Namie fleece coat sample	57
38	Starting point of the Namie fleece coat fractionation	57
39	Radioactive bundle of fibers detached from the main sample	58
40	Tree diagram of all the investigated samples of the Namie fleece coat	59
41	1.1.P.1.2 – Part 1/2: Overview image of sample	60
42	1.1.P.1.2: Image of the spherical CsMP candidate	61
43	1.1.P.1.2 – Part 2/2: Overview image of sample	63
44	F.1.3.1.3.1: Overview image of sample	64
45	1.4.P.1.1.1: Overview image of sample	65
46	1.4.P.1.1.1: Image of the angular CsMP candidate	66
47	1.4.P.1.1.1: Extraction process of angular CsMP candidate	67
48	1.4.P.1.1.2: Overview image of the top of sample	68
49	1.4.P.1.1.2: Overview image of the bottom of sample	69
50	1.4.P.1.1.2: Image of the spherical CsMP candidate	70
51	1.4.P.1.1.2: Extraction process of spherical CsMP candidate	71

52	C.2.1.1.2: Overview image of sample	72
53	Setup and result of PUF disks A, B, and C AIP exposure	73
54	Setup and result of PUF disks D, E, and G AIP exposure	73
55	Setup and result of PUF disks H, I, and J AIP exposure	74
56	PS.B.P.1: Photos of particle	75
57	PS.B.P.1: Overview image of sample	75
58	PS.B.P.1: Image of the first CsMP candidate	76
59	PS.B.P.1: Extraction process of first CsMP candidate	77
60	PS.B.P.1: Images of the second CsMP candidate	78
61	PS.B.P.1: Extraction process of second CsMP candidate	79
62	1.1.P.1.2 – Part 1/2: Large oval-shaped microparticle	89
63	1.1.P.1.2 – Part 1/2: Round structures on a fiber	90
64	1.1.P.1.2 – Part 2/2: Spherical microparticle	91
65	1.1.P.1.2 – Part 2/2: Irregularly rounded structure	92
66	1.1.P.1.2 – Part 2/2: Ellipsoidal microparticle	93
67	F.1.3.1.3.1: Largely irregular microparticle	94
68	F.1.3.1.3.1: Two small and irregular microparticles	95
69	1.4.P.1.1.1: Couple of irregular microparticles	96
70	1.4.P.1.1.1: Fused particulate structure	97
71	1.4.P.1.1.1: Prominent particle amongst group	98
72	1.4.P.1.1.1: Spherical particle amongst flakes	99
73	1.4.P.1.1.1: Bright irregular microparticle	100
74	C.2.1.1.2: Hidden spherical microparticle	101
75	C.2.1.1.2: Large jagged microparticle	101
76	C.2.1.1.2: Large spherical microparticle	102
77	C.2.1.1.2: Round flake	103
78	PS.B.P.1: Promising spherical microparticle	104
79	PS.B.P.1: Inconspicuous jagged microparticle	105
80	PS.B.P.1: Lone spherical microparticle	105
81	PS.B.P.1: Inconspicuous edged microparticle	106
82	PS.B.P.1: Huge edged microparticle	107

List of Tables

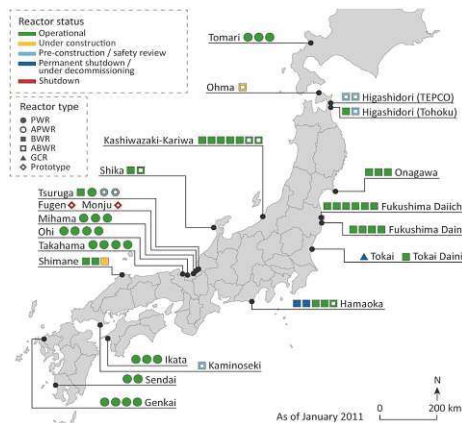
1	Commercial design info for FDNPP	3
2	FDNPP on-site AC power sources	6
3	Estimates of atmospheric radionuclide releases from FDNPP	15
4	Analytical tools available in radioactive particle research	17
5	Radionuclides from atmospheric nuclear testing	21
6	Overview of all identified CsMP types	30
7	FDNPP reactors' radiocaesium concentrations and ratios	35
8	PUF analysis results immediately after pickup	45
9	1.1.P.1.2: EDX data of the spherical CsMP candidate	61
10	1.4.P.1.1.1: EDX data of the angular CsMP candidate	66
11	1.4.P.1.1.2: EDX data of the spherical CsMP candidate	70
12	EDX data of the first CsMP candidate PS.B.P.1	76
13	PS.B.P.1: EDX data of the second CsMP candidate	79
14	1.1.P.1.2 – Part 1/2: EDX data of the oval-shaped particle	89
15	1.1.P.1.2 – Part 1/2: EDX data of round structures on a fiber	90
16	1.1.P.1.2 – Part 2/2: EDX data of a spherical microparticle	91
17	1.1.P.1.2 – Part 2/2: EDX data of the irregularly rounded structure	92
18	1.1.P.1.2 – Part 2/2: EDX data of an ellipsoidal microparticle	93
19	F.1.3.1.3.1: EDX data of a largely irregular microparticle	94
20	F.1.3.1.3.1: EDX data of two small microparticles	95
21	1.4.P.1.1.1: EDX data of a couple of irregular microparticles	96
22	1.4.P.1.1.1: EDX data of a bright irregular microparticles	100
23	C.2.1.1.2: EDX data of a large spherical microparticle	101
24	C.2.1.1.2: EDX data of a large jagged microparticle	102
25	C.2.1.1.2: EDX data of a large spherical microparticle	102
26	C.2.1.1.2: EDX data of a round flake	103
27	PS.B.P.1: EDX data of the promising spherical microparticle	104
28	PS.B.P.1: EDX data of the inconspicuous jagged microparticle	105
29	PS.B.P.1: EDX data of the lone spherical microparticle	106
30	PS.B.P.1: EDX data of the inconspicuous edged microparticle	106
31	PS.B.P.1: EDX data of the huge edged microparticle	107



Die approbierte gedruckte Originalversion dieser Diplomarbeit ist an der TU Wien Bibliothek verfügbar
The approved original version of this thesis is available in print at TU Wien Bibliothek.

1 Introduction

1.1 Overview of the FDNPP Site and Facility



(a) Location and type of all nuclear power plants in Japan as of January 2011. **Source:** [1]



(b) Photo of the FDNPP site in February 2007. **Source:** [2]

Figure 1: Overview of all nuclear power plants in Japan shortly before the accident as well as a photo of FDNPP in the years prior to the nuclear accident.

Most of the information cited in this and the following section 1.2 about the accident are summarized from the *Fukushima Daiichi Accident* report by the [International Atomic Energy Agency \(IAEA\)](#), specifically *Technical Volume 1/5 – Description and Context of the Accident*. It goes a lot more in-depth than needed for this thesis, especially the volumes 2 - 5, but to understand the context of the formation of CsMPs, it is of course important to know about the accident and therefore also the facility pre-accident in general.

As of January 2011, the Fukushima Daiichi Nuclear Power Plant was one of 21 nuclear power stations in Japan with a country-wide total of 54 reactors. It is situated approximately 220 km north-east of the capital Tokyo on Japan's Pacific east coast. A photo of the power plant years before the accident can be seen in figure 1b with the two distinct reactor complexes on the left and right hand sides. Numbered from left to right, Units 4 - 1 are in the left complex and Units 5 and 6 are in the right complex. The six cubical reactor buildings can be seen just behind their respective turbine buildings. Also clearly visible are the red and white stacks next to some of the units.

Bordering the roughly 3.5 km² large site are the two towns of Okuma and Futaba, respectively 5 km west and 4 km north of FDNPP. Around 50,000 people lived within a 15 km radius around the power plant before the accident [1]. The nearest major city to the site is Iwaki with previously around 350,000 inhabitants, now bordering the exclusion zone at about a 40 km distance to the plant.

The locations of all of Japan's power stations can be seen in figure 1a. By far the most used technology at the time was the [boiling water reactor \(BWR\)](#) making up 30 of the total 54 reactors. The majority of the other reactors were built using the [pressurized water reactor \(PWR\)](#) type. Japan also used the newer advanced pressure water reactor (APWR) and advanced boiling water reactor (ABWR) types as well as some gas-cooled reactors (GCR) and two other prototype reactors. All nuclear power stations were situated on the coasts for cooling reasons just as Fukushima Daiichi. Due to this, the site has an oceanic climate just like all of Japan, but with an additionally large dampening effect on the temperature due to the nearby ocean currents [1].

The site's elevation at FDNPP was originally 35 m, however due to the local geology [Tokyo Electric Power Company Holdings, Incorporated \(TEPCO\)](#) (the plant's operator) decided for an elevation of 10 m for reactor Units 1 through 4 and 13 m for Units 5 and 6. This was done in

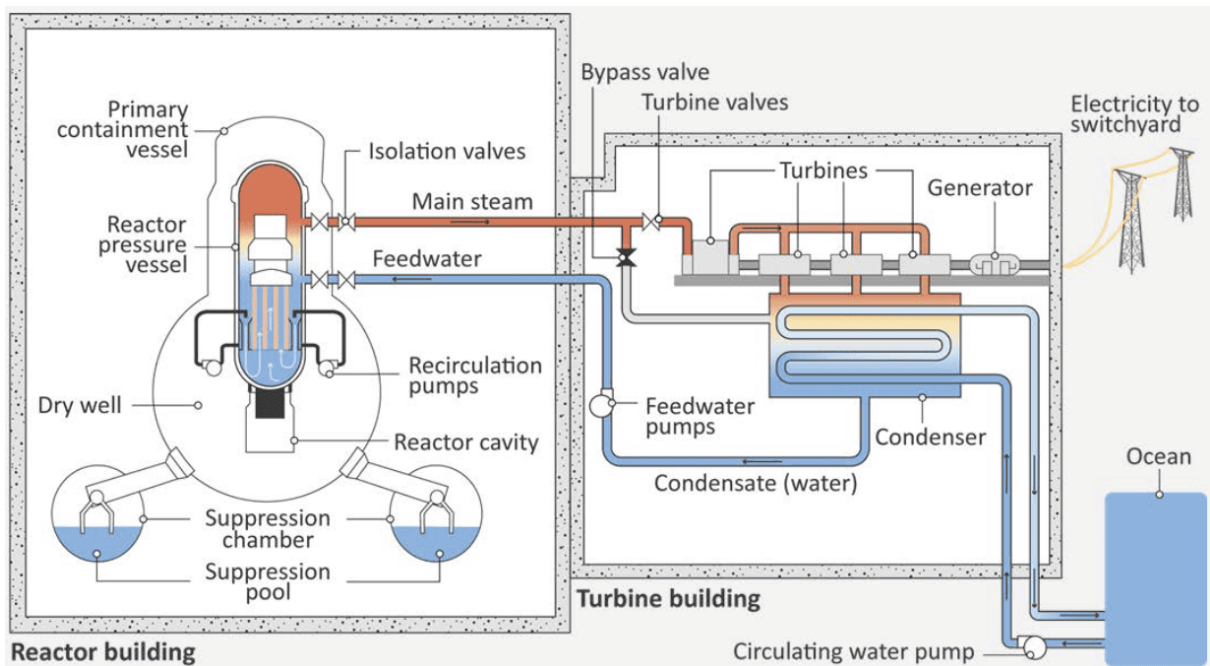


Figure 2: Simplified schematic diagram of the working principle of a BWR type nuclear power plant with access to ocean water like FDNPP. **Source:** [1]

order to build the plant on an acceptable bedrock formation, since most of the material above consisted only of clay mixed with sand and sandstone. Below this, thicker alternating layers of sandstone and mudstone were enough for the stable construction of the primary buildings [1].

In order to cool the individual reactor's condensers as well as other equipment, the nearby sea water from the Pacific Ocean was used. It was pumped to the necessary areas using two pumps per condenser via a special pump room. To protect the vulnerable power plant from high water levels, a special seawall was constructed in front of the site, which can also be seen in figure 1b [1]. It features a set of walls parallel to each complex of the reactor and turbine buildings as well as an additional set of walls protruding into the ocean. Water was drawn in from inside the volume of water protected by the seawalls and eventually discharged to the either side of it.

The seawall was originally designed to withstand a tsunami height of +3.122 m from the mean water level. Due to the lowered elevation of all the units at FDNPP, when compared to the original site elevation, they were obviously more susceptible to high water events of any kind. However, the seawall was thought to provide enough protection for the design requirement, since it was designed for a tsunami resulting from one of the world's largest earthquakes in Chile in 1960. Notably though, a combination of a tsunami with other oceanographic events was not considered while planning. The initial designs for the seawall were re-evaluated several times between 2002 and 2009 and finally resulted in a maximum tsunami height evaluation of +6.1 m – almost double the original requirement. As a result of that, the pump buildings were made watertight and the crucial pumps were raised in elevation twice [1].

In regards to earthquakes, the FDNPP site was ultimately deemed to be in an area of low seismic impact with most of the highest-magnitude seismic events taking place far away enough to be less of an issue. The nuclear power plant was designed and constructed to handle earthquakes directly below the site with a magnitude of up to M7.1 [1].

The first unit to start construction at FDNPP in 1967 was Unit 1. The design was first imported under contract with General Electric (GE) in the US and then licensed to the Japanese reactor manufacturers Toshiba and Hitachi. Units 2 - 6 were then constructed under contracts with either GE, Toshiba, Hitachi, or a combination of the three. For all of the plant's units, different types of the BWR product line by GE was used [1].

Table 1: Commercial design information for the FDNPP reactors. **Source:** [1, 3]

Description	Unit 1	Unit 2	Unit 3
Reactor Type	GE BWR-3	GE BWR-4	GE BWR-4
Gross Electrical Output [MW(e)]	460	784	784
Thermal Output [MW(th)]	1380	2381	2381
Fuel Type	UO ₂	UO ₂	UO ₂
Fuel Weight [t]	69	94	94
No. of Fuel Assemblies	400	548	548
Construction Start	September 1967	May 1969	October 1970
Commercial Operation Start	March 1971	July 1974	March 1976

Description	Unit 4	Unit 5	Unit 6
Reactor Type	GE BWR-4	GE BWR-4	GE BWR-5
Gross Electrical Output [MW(e)]	784	784	1100
Thermal Output [MW(th)]	2381	2381	3293
Fuel Type	UO ₂	UO ₂	UO ₂
Fuel Weight [t]	94	94	132
No. of Fuel Assemblies	548	548	764
Construction Start	September 1972	December 1971	May 1973
Commercial Operation Start	October 1978	April 1978	October 1979

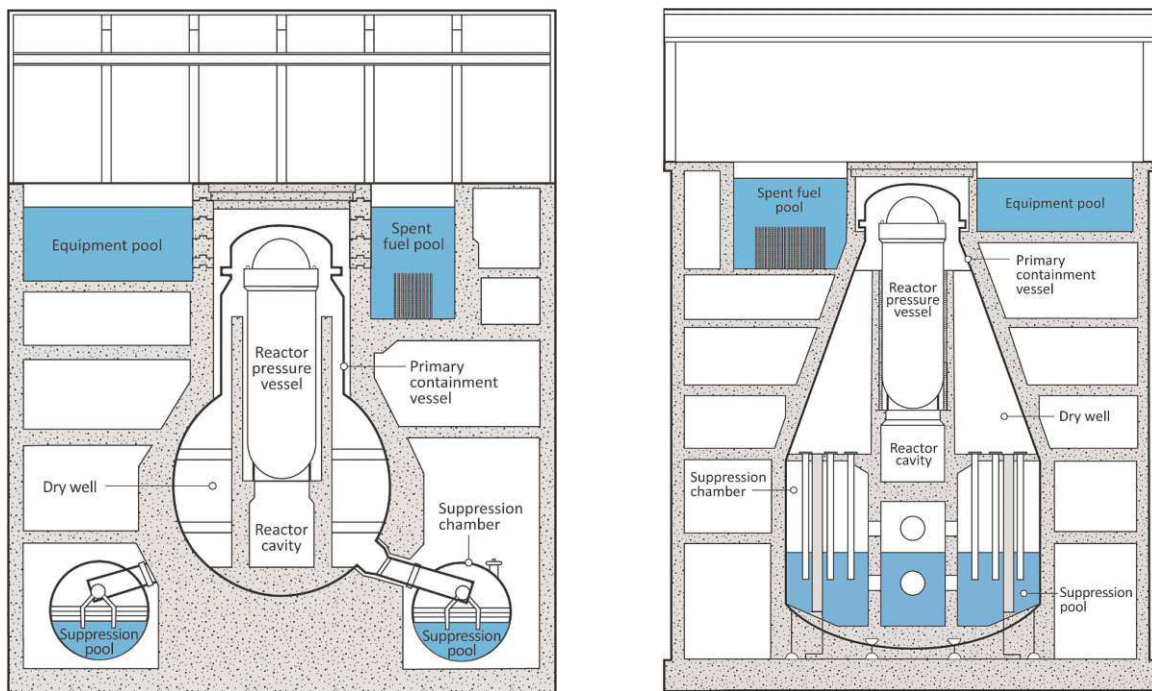
Boiling water reactors in general are used to convert water into steam directly in the core and to drive steam turbines with it to generate electricity. This is what differentiates them from PWRs as they only consist of one closed water/steam cycle and one open coolant cycle. In PWRs, water is never actually boiled in the primary circuit, because they consist of two closed water/steam cycles that are pressurized and one open coolant cycle. The concept of BWRs like the ones used at FDNPP can be seen in figure 2. Demineralized light water (H₂O) is used in this closed cycle loop both to remove the heat and cool the core, as well as to moderate the neutrons coming from the fuel rods and therefore controlling the reactivity of the system. Feedwater is pumped into the core, which then gets evaporated at a pressure of about 70 bar inside the reactor pressure vessel (RPV) [1]. This steam is then directed to a turbine that in turn drives an electric generator in order to generate power. After this, the remaining hot steam is driven through the condenser where it cools down, changes phase back to a fluid and flows back to the reactor's core via the feedwater pump. The condenser is made up of individual condenser tubes that are filled with cold ocean water that acts as the heat sink for the all of the steam's energy. The sea water is collected via pumps inside the perimeters of the seawall and then ejected through the sides like described previously.

Four different types of GE's BWR technology were used at FDNPP as can be seen in table 1. At the start of all construction operations, Unit 1 – the first one of the six – was still planned using the earlier GE BWR-3 type. Units 2 to 5 were then built according to the GE BWR-4 type, and finally the latest reactor, Unit 6, was designed according to the GE BWR-5 type. Therefore, this was also the only reactor at FDNPP with a gross electrical power output of more than 1 GW(e). The last unit to start commercial operations was, again, Unit 6 in October of 1979. There are a number of significant differences between the three utilized BWR types. First and foremost, as can be seen in table 1, each new revision of the technology increased the thermal and therefore the electrical power output. This is due to an increase in RPV volume between all of the types. The RPV inner diameter for Unit 6, for example, was about 33% larger

than that of Unit 1. This larger volume permitted the use of almost twice the fuel assemblies in the core with 400 for Unit 1 and 764 in Unit 6, which is the reason for the increase in power output. With this, the number of control rods also increased from 97 to 185 [1].

Other differences between the BWR reactors types lie in both the high and low pressure heat removal systems, which were crucial for the shutdown cooling of the isolated reactors under high and then low pressure conditions. A reactor is described as *isolated* as soon as the main steam isolation valves are closed and the steam turbines cannot be bypassed like in a normal shutdown cooling [1]. There are also differences between some of the additional safety systems such as the high and low pressure coolant injection systems and the core spray system. Relevant information about these differences and systems will be discussed in more detail in the accident section 1.2.

The containment systems for the GE BWRs at FDNPP were also different between the newer and older models. Units 1 - 5 had the so-called Mark-I containment and the newest unit, Unit 6, already had a Mark-II containment. In general, both designs had two fission product barriers and a common pressure suppression system to relieve pressure in the primary containment vessel (PCV) by condensing the steam in case of too high pressure in the containment vessel. The fission product barriers were twofold: there was the primary containment, i.e., the primary containment vessel (PCV), and the secondary containment, i.e., the reactor building (RB) [1].



(a) Simplified representation of the Mark-I containment configuration like in the GE BWR-3 reactor of Unit 1. The GE BWR-4 reactors of Units 2 - 5 featured the same configuration with only minor differences.

(b) Simplified representation of the Mark-II containment configuration like in the GE BWR-5 reactor of Unit 6 only.

Figure 3: Comparison of the Mark-I and Mark-II containments used at FDNPP. **Source:** [1]

The reactor core and respectively the RPV are both located in the PCV. Mark-I (Fig. 3a) and Mark-II (Fig. 3b) containments mostly differ in their geometry – especially that of the suppression chamber (SC). A comparison of both containment configurations is shown in figure 3.

In Mark-I containment, the dry well (DW) can be described as the classic *inverted bulb shape*. It is connected via a series of large ducts and spargers to the SC. The SC forms a toroidal shaped compartment made of sheet metal below the DW in which large amounts of water are present at

all times during normal operation – this is called the suppression pool. During a [loss of coolant accident \(LOCA\)](#), hot steam can flow through the ducts down in the spargers and into the pool of water, condensing below the surface, thus reducing the overall pressure in the [DW](#). The [DW](#), [SC](#), and all connecting ducts and spargers are part of the [PCV](#) [1].

In Mark-II containment, the pressure suppression system follows the same concept as in Mark-I [1]. What is different is that the Mark-II containment [DW](#) is formed in a truncated cone shape with the [SC](#) directly below it. In this design, the [DW](#) and especially the [SC](#) are completely surrounded by concrete. The [PCV](#) is much easier to distinguish from the rest of the structure due to its more compact nature in this containment.

There are also several additional safety systems in case of a discharge of radioactive material or formation of hydrogen gas in both the primary and secondary containments. During normal operation, the [PCV](#) is filled with nitrogen gas to counter the hazard of an accumulation of hydrogen in an accident. Additionally, should this not be enough to stop the accumulation of hydrogen gas, additional hydrogen recombiners can be started inside the [PCV](#). This system, however, does need AC power in order to function and there are none installed outside the [PCV](#) in the [RB](#). In case of an escape of gas contaminated with radioactive material from the [RPV](#), the suppression pool inside the [SC](#) can also be used to scrub the majority of radionuclides from the gas to reduce its radioactivity [1]. This obviously requires the availability of enough water inside the suppression pool and is only a compromise since it cannot guarantee the total absorption of all radioactive material.

Inside the [RB](#) another safety system is the [standby gas treatment system \(SGTS\)](#). It keeps the pressure inside the building below the outside atmospheric pressure. The air from the inside is filtered before being released, therefore preventing any radioactive material from being released to the outside world [1]. This system, however, does need AC power as well for operation.

In cases of severe accidents where the pressure inside the [PCV](#) exceeds a safe threshold, containment vents were installed in all of the units at [FDNPP](#) in the 1990s following a change in regulations in Japan. These so-called *hardened-vents* were made of pressure relief devices with thick-walled discharge pipes eventually leading to a stack. Their purpose was simple: prevent excessive pressure buildup inside the [PCV](#) that could compromise the containment integrity by controlled release of the built-up gas. At [FDNPP](#) there were two vent lines: one in the [DW](#), and one in the [SC](#). In any way it was preferred to vent through the [SC](#) in order to take advantage of the additional radioisotope scrubbing by the suppression pool water. However, in extremely severe cases the vent line leading from the [DW](#) was also necessary to deal with overpressurization in a timely manner. This line did not benefit from any scrubbing whatsoever and lead directly to the stack. The two vent lines eventually joined together to a single line just before the stack and a special rupture disk. The rupture disk was an additional safety mechanism in order to prevent premature venting. It was set to burst when a pre-set pressure was exceeded in the [PCV](#). According to the [IAEA](#) report, "the underlying philosophy in Japan was not to vent until it was inevitable, and as a last resort for maintaining the integrity of the primary containment in order to delay or prevent the direct release of radioactive material to the environment". Therefore, in line with this philosophy, active venting was to be procedurally delayed until the pressure in the [PCV](#) reached a value of twice its design [1].

Fukushima Daiichi was supplied with electricity via off-site and on-site power. Off-site power consisted of a total of seven power lines with at least a single transmission line per unit. There were also high-voltage power switch lines between Units 1 - 4, and Units 5 and 6 to form an interconnection between the main generators. There was no interconnection in between the two complexes, though [1].

In order to deal with a [loss of offsite power \(LOOP\)](#) and [station blackout \(SBO\)](#) emergencies, there were additional on-site backup power sources. This backup system comprised of multiple redundant [emergency diesel generators \(EDGs\)](#) for AC power (see Tab. 2) and a battery system for DC power. The [EDGs](#) were typically used for a [LOOP](#) event and the DC batteries in case

¹This [EDG](#) was out of service for maintenance at the time of the accident.

Table 2: FDNPP on-site emergency AC power sources. **Source:** [1]

Unit	Number of EDGs	Type	Location	Floor level
Unit 1	2	Water-cooled	Turbine Building	Basement
		Water-cooled	Turbine Building	Basement
Unit 2	2	Water-cooled	Turbine Building	Basement
		Air-cooled	Common SFP Building	Ground
Unit 3	2	Water-cooled	Turbine Building	Basement
		Water-cooled	Turbine Building	Basement
Unit 4	2	Water-cooled ¹	Turbine Building ¹	Basement ¹
		Air-cooled	Common SFP Building	Ground
Unit 5	2	Water-cooled	Turbine Building	Basement
		Water-cooled	Turbine Building	Basement
Unit 6	3	Water-cooled	Reactor Building	Basement
		Air-cooled	EDG Building	Ground
		Water-cooled	Reactor Building	Basement

of an SBO. During normal operation, the EDGs were idle and the batteries were kept fully charged. Each unit had at least two EDGs, most of the time in the turbine building basement, i.e., 7 - 8 m below the plant grade, with one exception being Unit 6 that had, in fact, a total of three EDGs. In an emergency these generators would provide backup AC power to all of the critical cooling systems, as well as the DC batteries that were also used to supply other DC loads at all times. At FDNPP these emergency on-site power sources were designed to be able to continuously run for eight hours during an SBO. At the time, this was typical for a nuclear power plant and they were typically equipped to handle power outages of 4 - 72 hours. The batteries were split between the basement of the control building and the mezzanine levels of the turbine buildings [1].

1.2 The 2011 FDNPP Nuclear Accident

On March 11, 2011, one of the world's most severe nuclear accidents in history would unfold. After one of the largest earthquakes ever recorded, a tsunami would overwhelm the seawalls at the Fukushima Daiichi Nuclear Power Plant (FDNPP) and flood the primary and backup power systems, leading to the total loss of power at the site. The main shock lasted for more than 2 minutes with a magnitude of M 9.0. Due to the damage sustained, an extended SBO would lead to the total loss of four of the six units, with three of those lost due to the complete loss of plant cooling, resulting in the fuel overheating and melting. This in turn would result in the release of radionuclides into the atmosphere. In this section, a chronological sequence of the events that took place on this day will be described. Again, most of the information will be summarized from the Fukushima Daiichi accident report [1]. All timestamps are cited in the respective local time, i.e., Japan Standard Time (JST) (UTC +09:00). For quick reference, an overview of the main event sequence is shown in figure 4.

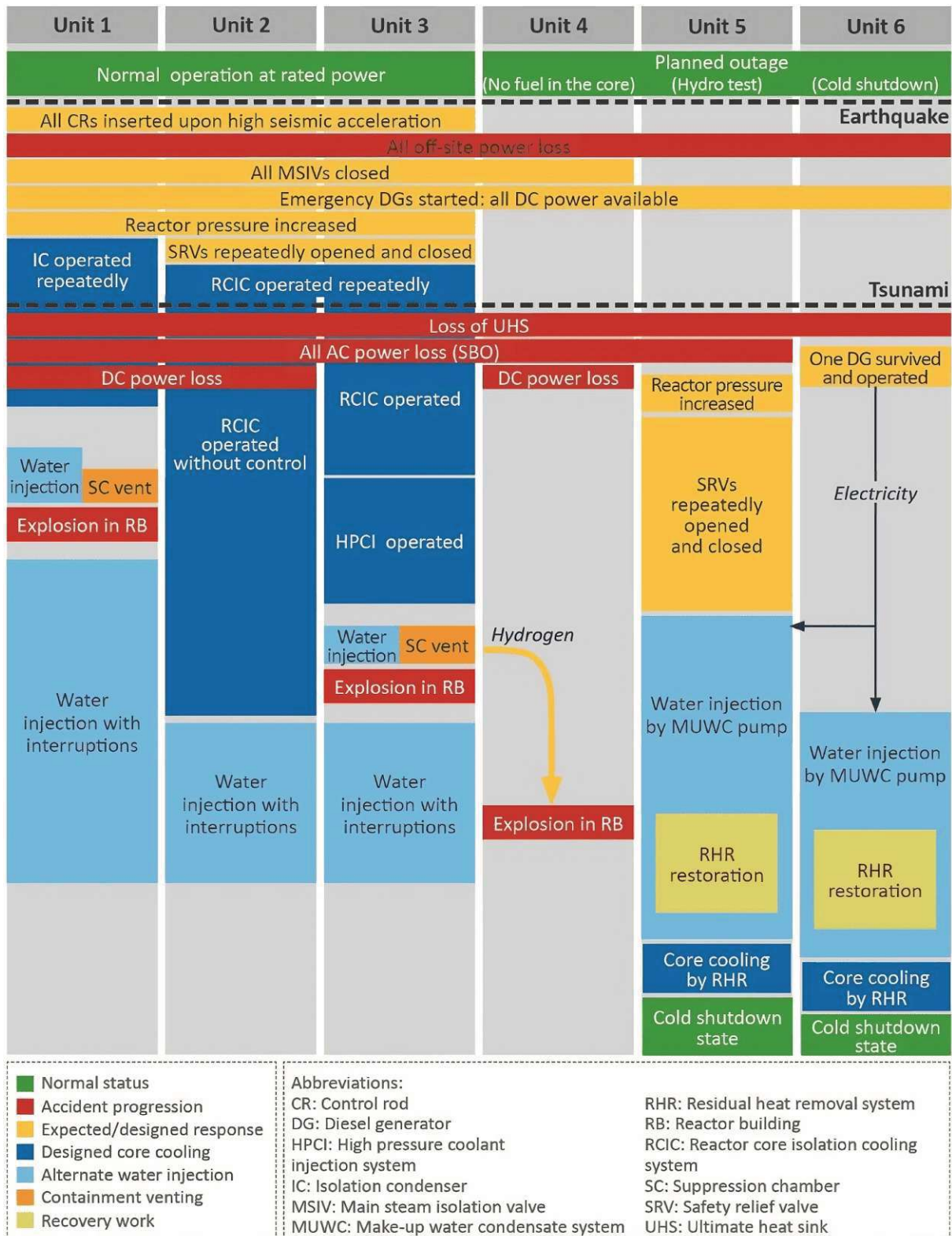


Figure 4: Overview of the main sequence of events at FDNPP shortly before and after the earthquake and tsunami hit the site. Source: [1]

1.2.1 Onset of the Accident

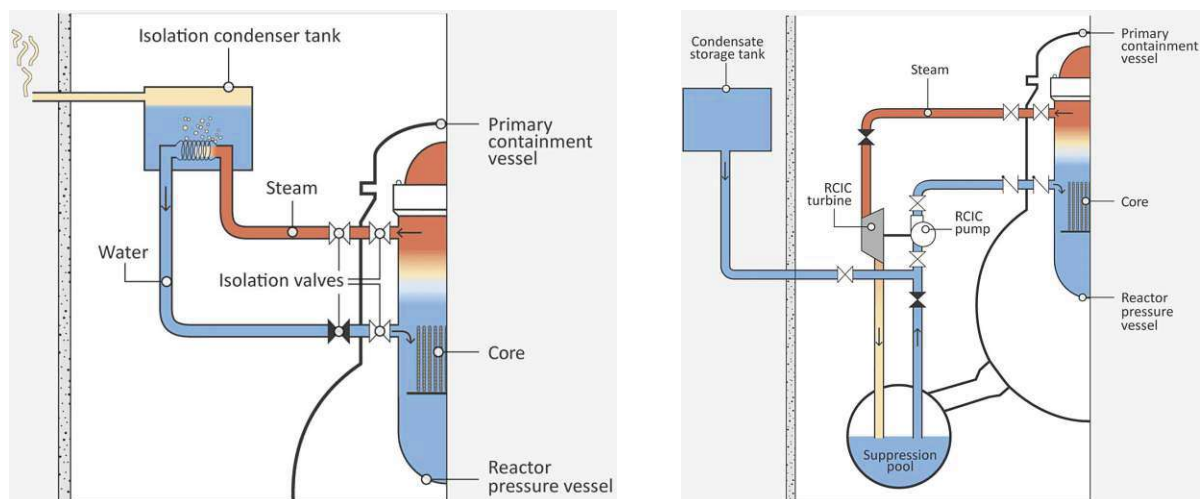
The initiating event of the entire accident cascade was the Great East Japan Earthquake, better known internationally as the 2011 Tohoku Earthquake [4]. The epicenter was about 180 km north-east of FDNPP and the neighboring Fukushima Daini Nuclear Power Plant. The closest nuclear power plant to the epicenter on this day was Onagawa nuclear power plant (NPP) to the north of FDNPP as shown in figure 1a.

The earthquake consisted of a main shock with several significant pulses and aftershocks, which caused severe damage to the infrastructure in the surrounding area, including vital power transmission lines. At 14:46, just when the seismic event started, Units 1 - 3 were at their rated power and Units 4 - 6 were in several different stages of planned maintenance or inspection. Citing from the accident report, the status of all six units of the power plant was as follows [1]:

- Unit 1 was generating 460 MW electricity.
- Unit 2 was generating 784 MW electricity.
- Unit 3 was generating 784 MW electricity.
- Unit 4 had its fuel off-loaded from the reactor core to the fuel storage pool, the **spent fuel pool (SFP)**, and no fuel assemblies were in the **RPV**, the vessel that houses the reactor. Both the **SFP** and **RPV** were filled with water.
- Unit 5 had fuel assemblies loaded in the reactor core. The fuel had relatively low decay heat due to the period elapsed since power operations. The **RPV** was filled completely with water and isolated (bottled up) and was being pressurized by a pump in preparation for the **RPV** pressure (leak) test. Its confinement structure, the **PCV**, was open, with its lid removed.
- Unit 6, which was under the cold shutdown state of the outage, also had fuel assemblies with relatively low decay heat loaded in the reactor core, and the **RPV** was filled with water to a prescribed height, sufficiently covering the reactor core. The **main steam isolation valves (MSIVs)** that, when closed, disconnect the **RPV** from rest of the power plant, were open, and the **RPV** was nearly at atmospheric pressure and ambient temperature.

When sensors on the site detected the excessive ground motion, as designed, Units 1 - 3 were automatically shut-down by insertion of the control rods, which stopped the nuclear chain reaction. Despite that, the decay heat from the reactors still, of course, had to be cooled by the mostly electrically-run cooling systems. However, the earthquake caused so much damage to on- and off-site AC power equipment and transmission lines that the off-site power was cut in its entirety to all of the units, resulting in a **LOOP** event. Because of this, the **EDGs** were automatically started as designed and restored power to all of the six units and also the DC batteries [1].

Another automatic safety measure after the initial earthquake was the isolation of the reactors from the turbine systems by closing the **MSIVs**. This naturally lead to an increase in core temperature and thus increased core pressure. In order to cool the reactors when they are isolated, there were mainly two systems in place that are shown in figure 5. The **isolation cooler (IC)** (Fig. 5a) is a trivial system that uses cold water tanks (isolation condenser pools) outside of the **PCV** to cool down and condensate the steam from the reactor. The water inside the tank would eventually boil away and be released to the atmosphere, thereby acting as the heatsink. This naturally works completely without the need for power by the use of gravity and was sufficient for 8 h of operation before needing to be replenished. The **reactor core isolation cooling (RCIC)** (Fig. 5b) works by using the **SC** together with a condensate storage tank as a heatsink. The steam from the reactor drove a small turbine that in turn ran a pump that injected water back in the reactor at a high pressure. The water lost from the reactor was restored by the storage tank. This formed a closed loop cycle that was designed to run for at least 4 h. All the



(a) Working principle of the isolation cooler (IC) in the design of Unit 1.

(b) Working principle of the reactor core isolation cooling (RCIC) in the designs of Units 2 - 6.

Figure 5: Overview of the systems for cooling the reactor cores when the system is isolated from the turbines (MSIVs closed). **Source:** [1]

units at the power plant responded to the initial events according to the appropriate operating procedures and as intended by their designs [1].

About 40 minutes after the initial earthquake, the tsunami began hitting the power plant. The seawalls were able to protect the site from the first, smaller wave – the second wave with a run-up height of 14 - 15 m, however, inundated large parts of the plant. This damaged the pumps and motors for the water-cooling of all essential plant systems, including the water-cooled EDGs, resulting in a loss of ultimate heat sink (UHS). All of the reactor and turbine buildings, the common SFP storage building, and diesel generator building were flooded with damage to the EDGs and some critical electrical systems. All emergency power, except for the Unit 6 (air-cooled) EDG was thereby lost. This resulted in an SBO for Units 1 - 5, which should have been covered by the DC power backup sources. Due to the damage of the plant flooding, Units 1, 2, and 4 gradually lost power and the operator were unable to monitor vital reactor parameters. DC power was still available for Units 3 and 5, and allowed operators to prevent reactor overpressurization. As mentioned previously, Unit 6 maintained AC power and it was decided to inject low-pressure water into the reactor using the make-up water condensate (MUWC) system [1].

1.2.2 Progression of the Accident

Due to the fact that critical reactor systems could not be verified, because of the loss of all power, it was determined that core cooling is likely compromised. Therefore, alternative ways to inject coolant water into the reactors using the station fire engines via the fire protection system were identified. Since Unit 1 lost all core cooling, its pressure did not decrease as would be needed for the alternative low-pressure water injection. Assuming the worst case scenario for Unit 2, which would be a similar loss of all core cooling including the backup systems, the public was ordered to be evacuated within a 3 km radius around FDNPP on the same day. Later that night, high radiation levels were first discovered in the Unit 1 RB and then in the turbine building, restricting access to these parts of the plant. This marked the severity of the status of Unit 1, including the still non-functioning IC system. Just before midnight, pressure readings inside the Unit 1 PCV indicated an exceedance of the maximum containment design pressure [1].

On early March 12, the RCIC of Unit 2 was confirmed to be operating, meaning priority

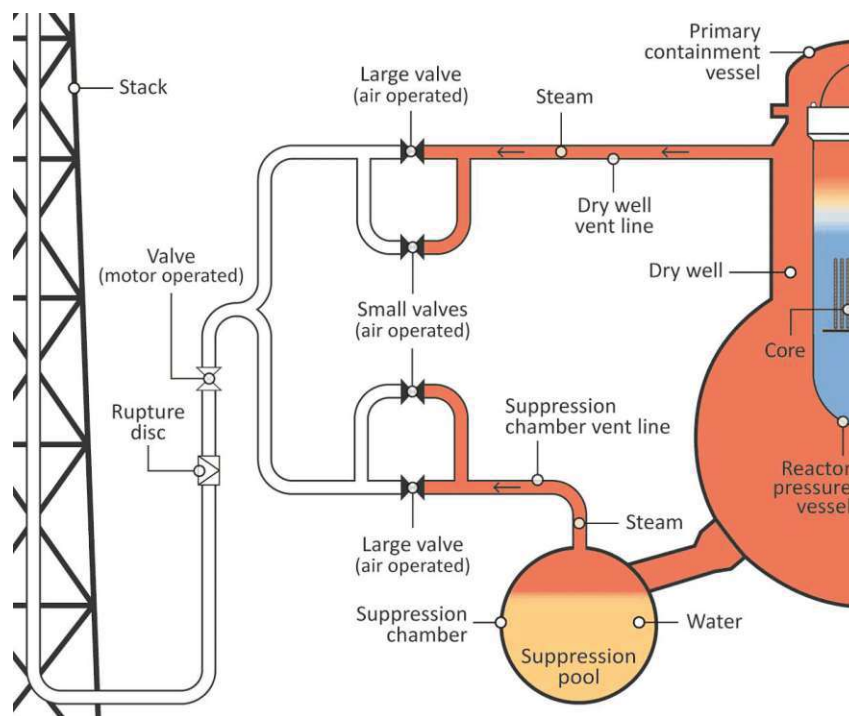


Figure 6: Schematic of the containment venting system with thick-walled discharge piping from the DW and the SC to a single stack. It was used to prevent a breach of the PCV's integrity by overpressurization. Venting through the SC was preferred due to radioisotope scrubbing. At FDNPP the vent line contained an additional rupture disk. **Source:** [1]

could be given to the Unit 1 core cooling. Almost 13 hours after the SBO, the alternative water injection by fire engines to the Unit 1 reactor commenced. In the mean time, radiological conditions around Unit 1 only worsened. A white fog-like steam was noticed in the RB and shortly after that, a sudden drop in pressure of the PCV accompanied a 10x increase in radiation levels. In order to ensure continuous water injection to Unit 1 by the fire truck, a direct injection line could be established in the morning, connecting a freshwater tank to the fire protection port [1].

In the meantime, in Unit 2, the RCIC condensate tank was running dry and the SC was quickly filling up, making it necessary for workers to switch the system to use the water inside the SC, increasing its temperature as expected. Nearly 17 hours after the SBO, AC power could be restored to Unit 5 through interconnects with the Unit 6 EDG. This ensured the continued operation of the reactor heat removal systems. Before that, safety relief valves (SRVs) were repeatedly opened and closed to relieve pressure from the RPV of Unit 5 [1].

During all of this time, the RCIC in Unit 2 ran for a good 20 hours straight – more than 5x its minimum design requirement. However, after this time, pressure and temperature inside the SC naturally increased, the system ceased to function, and another emergency core cooling system activated. Due to all of this, it was decided to also start spraying the SC with freshwater via the fire protection ports as in the case of Unit 1 [1].

At around 14:00 on March 12, venting operations were commenced at Unit 1 in order to prevent a breach of the containment's integrity. This successfully lowered the pressure inside the PCV and led to a delayed increase in radiation dose rate readings of 1 mSv/h north-west of Unit 1. An overview of the venting system used at FDNPP is shown in figure 6. Just after this, water injection to the reactor stopped because of the depletion of the freshwater tank. Therefore, the decision was made to use seawater for the continued injection instead [1].

At 15:36, an explosion occurred on the service floor of the RB of Unit 1, severely damaging the upper building structure. The explosion, fortunately, did not seem to directly affect the PCV. At the time, the cause of the explosion was unknown, but it was suspected that hydrogen

had escaped from the core into the **RB**. This explosion only worsened the already bad conditions for emergency workers and even damaged the seawater injection lines to the Unit 1 core. Because of all of this, the radiation dose rates at the site worsened as well and the evacuation zone was extended to a 20 km radius. As a precaution, venting preparations were started for Units 2 and 3, although not immediately necessary [1].

After a temporary evacuation following the explosion, the injection of seawater into Unit 1 was re-established and later boric acid was also added to address concerns of recriticality in the reactor. In the meantime, the situation for Unit 3 worsened, when an emergency core cooling system was turned off due to concerns with its continued safe operation. At 05:10 on March 13, Unit 3 therefore became the next unit to lose core cooling after Unit 1. In the end, this led to the reactor not being cooled for 7 hours, which was an adverse turning point for the fate of Unit 3. At the same time, neutrons were detected by a mobile radiation monitor as far as 1 km away from the reactor. After the accident, it was concluded that these originated likely from Unit 3 by spontaneous fission of actinides that had been released due to the sustained core damage [1].

As a consequence of the loss of core cooling, a new fire engine line to the fire protection system of Unit 3 was established to inject seawater into the reactor. However, due to contrary orders from the **TEPCO** headquarters, injection was delayed until the reactor pressure increased above the pump pressure of the fire engine and injection did not occur. To fix this, it was attempted to vent the **PCV**, however, this failed due to the pressure being too low for the rupture disk to burst (see Fig. 6). After this, it was tried to open an **SRV** electrically using batteries, some of which were collected from cars. This seemed to work, since the reactor pressure decreased following this action. The drop in pressure finally made it possible to use the fire engine to spray borated freshwater into the reactor. Along with the depressurization of the **PCV**, a pressure surge inside the **SC** occurred, following an exceedance of the maximum design pressure and a subsequent rapid drop in pressure. This indicated the successful containment venting due to the bursting of the rupture disk [1].

At approximately 10:15 and 12:05, in light of the recent events at Unit 3, venting of Unit 2 was readied and the injection of seawater into the reactor was prepared, taking advantage of the still favorable radiological conditions that could quickly worsen at any time. Once again, this was done using the available fire engines. Shortly thereafter, the freshwater pool was depleted and the workers had to switch to seawater for Unit 3. Around two hours later, the radiation dose rate increased significantly, marking a probable release of radioactive gasses from the Unit 3 reactor, which meant that hydrogen would also likely have leaked at the same time [1].

Later that evening, power from the Unit 6 **EDG** could be connected to Unit 5, making it possible to use the **MUWC** system for water injection. Before that, reactor pressure had to be decreased in order for the pumps to work – this was done via the **SRVs**. In addition to this, the now available AC power was also used to operate the **SGTS** in the Unit 5 **RB**, ensuring secondary confinement [1].

In the early morning of March 14, the water level available for the seawater injections dropped so low that the water injections to both Unit 1 and 3 had to be stopped temporarily. The hoses were lowered down and the remaining seawater was now reserved to cool Unit 3 only. Following this, the containment pressure of Unit 3 continued to increase until the core probably got uncovered at 06:20 in the morning. This, however, did not initially seem to be critical, since the pressure kept decreasing back to a more sustainable value. After a couple of hours, the seawater reservoir could be filled up and water injections to all of the units were re-established [1].

At 11:01 on March 14, an explosion occurred in the upper parts of the Unit 3 **RB**, which destroyed the structure above the service floor and injured workers. It happened at a time when the water injection to Unit 1 was getting ready to be restarted, but required workers to temporarily evacuate the premises. This delayed the injection to Unit 1 and interrupted that to Unit 3. The cause of the explosion was unknown at the time, but another hydrogen explosion was suspected. Importantly, this also affected the Unit 2 venting line, making it impossible to use the previously set-up vent lines to relieve pressure for that unit, in the case it would be

needed later on [1].

After this setback, the plant staff began re-establishing the seawater injection lines to both Unit 1 and Unit 3, but this time the water was sourced directly from the ocean instead of the reservoir. Only about 3 hours later, Unit 2 experienced a loss of core cooling now as well, being the third of the six units to do so. Suspecting a failure of the Unit 2 RCIC, workers prepared to inject seawater using the fire protection system via the fire engines once again. However, this was initially impossible since the pressure inside the RPV was too high for the fire engine pumps. For this exact case, Unit 2 was originally prepared to be vented through the usual venting lines, but the hydrogen explosion in Unit 3 permanently closed the isolation valve. Therefore, it was decided to use the SRVs to depressurize the RPV into the PCV, which would release some of the steam into the containment. At around 20:00 on March 14, the depressurization concluded successfully and the fire engines began to inject seawater into the reactor of Unit 2 [1].

Nearing midnight on March 14, a substantial rise of the dose rates in the DW and the SC were noticed. Neutrons were also detected near the main gate from 21:00 until 01:40 on March 15. At the same time, the pressure inside the RPV steadily increased, making it necessary for on-site staff to open more and more SRVs into the PCV. This in turn only kept increasing the containment pressure, and workers still were unable to open the vent valves. As a last resort, staff tried to vent through the DW venting line, hoping that this would work. However, these efforts would turn out to be fruitless as it was impossible to open the DW vents either [1].

Finally, at 06:14 in the morning on March 15, an explosion was heard, following a drop in pressure inside the SC of Unit 2. The information at hand indicated a possible PCV failure and a possibly uncontrollable release of radioactive gases from Unit 2. This resulted in the evacuation of around 650 staff members to the near Fukushima Daini NPP, and only 50 - 70 people remained at FDNPP. At about the same time, an explosion in the upper parts of the Unit 4 RB was observed by evacuating workers. At about 08:25, two hours later, white smoke or steam was observed rising from the Unit 2 RB. At this time, the highest dose rate measurement at the main gate of the site was recorded: 11.93 mSv/h. Two hours later, because of the elevated levels of radiation, the authorities ordered all residents within a radius of 20 - 30 km surrounding the plant to take shelter indoors [1].

At around 10:45, a team attempted to enter the Unit 4 RB to assess the damage caused by the explosion and investigate the integrity of the SFP. The dosimeter that they were carrying maxed out at a dose rate of 1000 mS/h. A remote visual inspection from a helicopter was conducted on the afternoon of March 16, confirming sufficient water inside the SFP of Unit 4. It was not possible to assess the water levels in the Unit 3 SFP, though, hence making it a priority. On March 17, helicopters dropped around 30t of seawater on the Unit 3 RB. Additionally, freshwater was sprayed onto the Unit 3 SFP later that same day. In the following days, seawater and freshwater were also sprayed onto the Unit 4 SFP [1].

Finally, almost exactly 9 days after the SBO, at 15:46 on March 20, off-site power was restored to Units 1 and 2. Just the day prior, the second EDG in Unit 6 was powered up and both EDGs continued to provide AC power for Units 5 and 6. The SBO in Units 3 and 4 was ended after more than 14 days, when off-site power was restored to them on March 26. During this time, water injection was also switched from seawater to borated freshwater and the fire pump were replaced by a stationary pump, eventually driven by off-site power [1].

Units 5 and 6 reached the cold shutdown mode on March 20, Units 1 - 3 reached a similar state on December 16². This marked the end of the accident phase as defined by the Japanese government. For a few months after this, some plant conditions still remained to be unstable, until stable parameters finally could be achieved in March and April 2012 [1]. At the time of writing, decommissioning efforts for Units 1 - 4 are estimated by TEPCO to take another 20 - 30 years until completion [7].

²The *cold shutdown state* for Units 1 - 3 was defined by the Japanese government based on two conditions defined in their *Roadmap towards Restoration from the Accident at Fukushima Daiichi Nuclear Power Station* [5, 6].

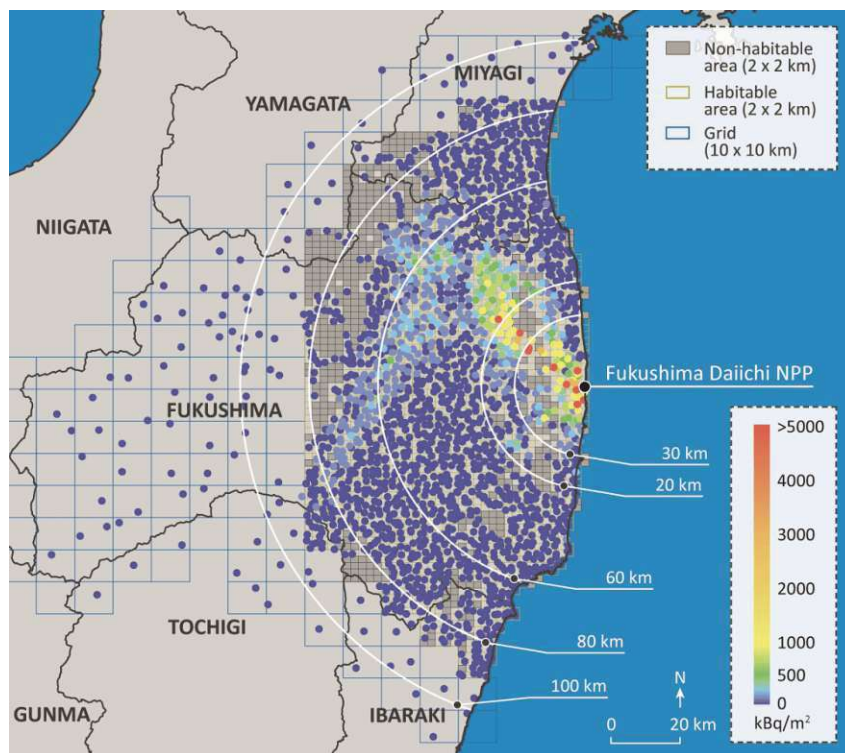


Figure 7: Deposition density in Bq/m^2 of ^{137}Cs based on soil sampling, decay corrected to 14 June 2011. **Source:** [1]

1.2.3 Releases of Radionuclides

Uncontrolled releases of radionuclides into the terrestrial and aquatic environment continued for several weeks after the accident. Besides a large amount of short-lived isotopes with half-lives of only hours to days, most of which were fission noble gases, trace amounts of strontium and plutonium were emitted as well. Several releases until the end of March 2011 distributed mainly ^{131}I , ^{134}Cs , and ^{137}Cs onto Mainland Japan surrounding FDNPP. Prevailing westerly winds deposited most of the radioactive fallout from the accident in the Pacific Ocean [9]. This can be seen when comparing the land deposition density of ^{137}Cs in figure 7 with that of the Pacific in figure 8. The dispersion into the terrestrial environment mainly took place in the north-west area, up to about 60 - 80 km from the site with values ranging up to over 5 MBq/m^2 . In contrast, aeolian input to the ocean resulted in deposition densities of up to 10 MBq/m^2 over a much larger area due to natural ocean currents. The highest value of the deposition on Mainland Japan was 15.5 MBq/m^2 , recorded just north of FDNPP [9].

Table 3 shows the estimated atmospheric releases from FDNPP and compares it with those of the Chernobyl accident. It is clearly visible that the fallout from Fukushima mainly consisted of fission noble gases, that escaped mostly during the venting operations or the hydrogen explosions. There was also a significant release of volatile fission products such as different Te, I, and Cs radioisotopes. The maximum temperature of the reactors at the time of the release can be estimated to around 2100 - 2300 $^{\circ}\text{C}$, which implies that all of the volatiles with a boiling point below this temperature were released in the form of vapors. After the releases, these vapors would quickly condense back onto particulate matter in the environment, except for the isotopes of iodine [1].

In contrast, semi- and low volatile fission products, as well as refractory elements were scarcely emitted, especially when compared to Chernobyl. The release of the less volatile fission products mainly originated due to core overheating and melting of the nuclear fuel without the presence of ambient air [1]. Ultimately, with the exception of the similar scale of the ^{85}Kr and ^{133}Xe releases, all other radionuclide emissions were orders of magnitudes lower than that of

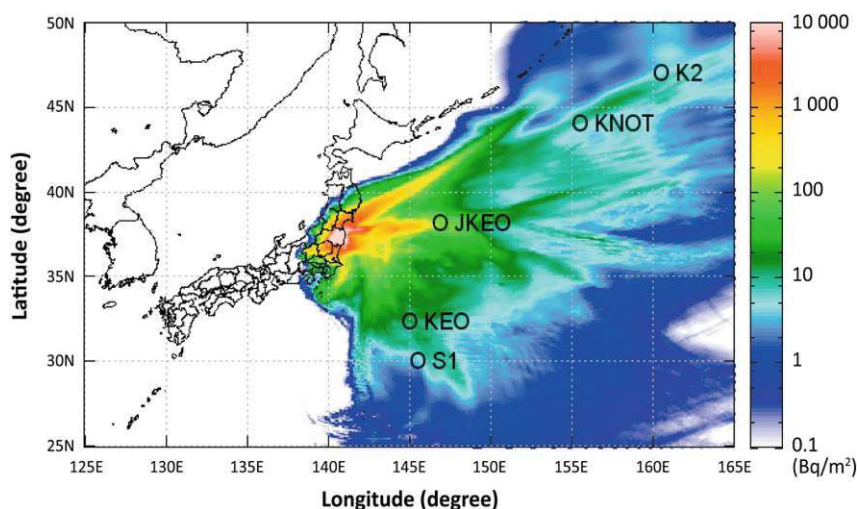


Figure 8: Modeled cumulative ^{137}Cs aeolian input through 1 April 2011. Deposition density in Bq/m^2 . **Source:** [8]

Chernobyl. This is especially true for the two ruthenium radioisotopes ^{103}Ru and ^{106}Ru , as well as ^{99}Mo .

Initially, the most important radionuclides that were especially radiologically relevant to humans were ^{134}Cs (2.1 yr half-life), ^{137}Cs (30.1 yr), ^{131}I (8.05 d), and $^{129\text{m}}\text{Te}$ (33.6 d). In the long term, only the two radiocaesium isotopes were relevant [9]. It can be argued that, at the time of writing, even the ^{134}Cs has lost most of its radiological concern since the accident.

After the accident, a comprehensive monitoring program was launched including measurements of ambient dose rates and of radionuclide activity concentrations in soil, crops, food, and feed for animals. On the basis of these measurements, restrictions on the consumption and distribution of food and water were implemented. After the Fukushima Prefecture itself, the most affected prefectures were Iwate, Miyagi, Ibaraki, Tochigi, Gunma, and Chiba. For example, high amounts of radioiodine and radiocaesium were detected on some crops in the form of direct deposition, as well as inside vegetables through normal uptake. However, due to the relatively early stage of the growing season, most of the crops and animal products were unaffected by the direct deposition, limiting its overall distribution [9].

It was estimated that around 130 cancer-related mortalities and about 180 cancer-related morbidities would result from the inhalation, external exposure, and ingestion of radionuclides worldwide, the majority of which concerning Mainland Japan itself. However, there are significant uncertainties with these estimates since it is inherently difficult to link them with the low-dose radiation. These estimates do not take into account the approximately 20,000 workers at FDNPP, though. Although no acute radiation sickness has been observed, it is estimated that a total of 146 staff members have received a radiation dose of more than 100 mSv, in highly varying degree, which is the minimum level statistically shown to increase cancer risk. However, these numbers are over-shadowed by the amount of disaster-related casualties during the initial earthquake and tsunami, as well as during the evacuation. The latter alone would result in an estimated 600 fatalities and it was projected that even the upper bound for the lives saved by the evacuation (due to cancer-related illnesses) was much lower than the number of deaths caused by it [20]. On top of this, the incident and evacuation naturally caused a number of social issues, the majority of which are psychological effects commonly observed after an NPP accident and are largely detrimental to overall mental health [21, 22].

³Range of estimates from JNES, 2012 [10], NISA, 2011 [11, 12], IRSN-2, 2012 [13, 14, 15], IBRAE, 2012 [16, 17, 18], with the exception of Xe-133, I-131 and Cs-137, where the estimated range is based on the greater number of estimates described in Technical Volume 1, Section 1.4 [1] (excluding early estimates, made in March-April 2011).

⁴From Ref. [19]

Table 3: An illustrative range of estimates of atmospheric releases of a wider range of radionuclides [PBq] from the FDNPP accident and comparison with those from the Chernobyl accident. Source: [1]

Radionuclide	Fukushima Daiichi ³	Chornobyl ⁴
Fission noble gases		
⁸⁵ Kr	6.4 - 32.6	33
¹³³ Xe	6 000 - 12 000	6 500
Volatile fission products		
^{129m} Te	3.3 - 12.2	240
¹³² Te	0.76 - 162	≈1.15×10 ³
¹³¹ I	100 - 400	≈1.76×10 ³
¹³³ I	0.68 - 300	2 500
¹³⁴ Cs	8.3 - 50	≈47
¹³⁶ Cs	-/-	36
¹³⁷ Cs	7 - 20	≈85
Semi- and low volatile fission products		
⁸⁹ Sr	4.3×10 ⁻² - 13	≈115
⁹⁰ Sr	3.3×10 ⁻³ - 0.14	≈10
¹⁰³ Ru	7.5×10 ⁻⁶ - 7.1×10 ⁻⁵	≈168
¹⁰⁶ Ru	2.1×10 ⁻⁶	>73
¹⁴⁰ Ba	1.1 - 20	240
Refractory elements		
⁹⁵ Zr	0.017	84
⁹⁹ Mo	8.80×10 ⁻⁸	>72
¹⁴¹ Ce	0.018	84
¹⁴⁴ Ce	0.011	≈50
²³⁹ Np	0.076	400
²³⁸ Pu	2.4×10 ⁻⁶ - 1.9×10 ⁻⁵	0.015
²³⁹ Pu	4.1×10 ⁻⁷ - 3.2×10 ⁻⁶	0.013
²⁴⁰ Pu	5.1×10 ⁻⁷ - 3.2×10 ⁻⁶	0.018
²⁴¹ Pu	3.3×10 ⁻⁷ - 1.2×10 ⁻³	≈2.6
²⁴² Cm	9.8×10 ⁻⁶ - 10 ⁻⁴	≈0.4

1.3 Radioactive Particles in the Environment

1.3.1 Overview

To begin with, it is important to define what *radioactive particles* – popularly called *hot particles* – are and what makes them special from other radioactive material. Quoting from the *Radioactive Particles in the Environment* publication of the IAEA [23], this is their definition:

Radioactive particles are defined as a localized aggregation of radioactive atoms that give rise to an inhomogeneous distribution of radionuclides significantly different from that of the matrix background. In water, particles are defined as entities having diameters larger than 0.45 μm , i.e., that will settle due to gravity. Radionuclide species within the molecular mass range 0.001 μm - 0.45 μm are referred to as radioactive colloids or pseudo-colloids. Using the grain size categories for sand, silt and clays, particles larger than 2 mm should be referred to as fragments. In air, radioactive particles ranging from submicron in aerosols to fragments are classified according to the aerodynamic diameters, where particles less than 10 μm are considered respiratory.

Radioactive particles have been released from multiple sources, especially since the mid-twentieth century with the dawn of the nuclear age, both for military and civilian use. These particles stem from a multitude of different sources, mainly being nuclear weapons tests, reactor accidents, refractory plants, and even **naturally occurring radioactive material (NORM)** particles at mining sites or coal-fired power plants for example [24, 25]. Even inconspicuous sources like coal-fired power plants emit significant amounts of radioactive microparticles from **NORMs** into the environment [26]. These particles are crucial for nuclear forensics due to the sheer amount of information these materials can offer when analyzed. Over the years, many investigations have shown that particle composition seems to reflect the origins, while particle size, crystalline structure, distribution, and even oxidation state depend on the release scenario itself [25, 23]. Importantly, these characteristics also affect how the particles will behave in the environment after their release. This is affected by the weathering rates and the mobilization of the associated radionuclides, therefore influencing the ecosystem transfer as well as the biological uptake and effect [23].

Using these properties, it is possible to make statements about the possible origins and the formation processes of radioactive particles, without needing much more than the particle itself. In the following sections, particle characterization and dosimetric aspects will be discussed, as well as a selection of arguably the most prevalent sources of this kind of particles.

1.3.2 Particle Characterization

A common way to characterize radioactive particles is to analyze the following properties, again quoting from the *Radioactive Particles in the Environment* publication of the IAEA [23]:

- Particle size, shape and appearance; particle size distribution for a set of particles or size (diameter) of individual particles, including aerodynamic diameter for airborne particles as well as shape and color
- Elemental composition including the 2D and 3D distribution of radionuclides and stable elements within the bulk particle and on surfaces
- Structures such as crystalline and amorphous phases
- Valence and oxidation states, surface charge properties

Additionally, in some cases it might also be necessary to know about particle densities, frequencies, as well as their spatial and depth distributions [23].

Table 4: Analytical tools available in radioactive particle research. **Source:** [25], modified from [23]

Method	Information obtained	Comments
Identification		
Size fractionation in water followed by radioanalytical techniques	Size distribution	
Cascade impactor with aerosol filters followed by radioanalytical techniques	Size distribution (AMAD)	
Portable monitors in the field	Hot spot identification	
Digital autoradiography	Distribution of radioactivity	Easy and time saving, non-destructive,
Real-time imaging techniques	Distribution of radioactivity	Easy and time saving, non-destructive
Repeated sample splitting combined with γ -spectrometry	Elevated activities in sub-samples indicate heterogeneities	Non-destructive
Repeated sample mixing combined with γ -spectrometry	Skewed frequency distribution of the counts indicate heterogeneities	Non-destructive
Isolation		
Repeated sample splitting in fractions combined w/light microscope and GM-tube, γ -spectrometry or autoradiography	Elevated activity in sub-samples indicate heterogeneities	Non-destructive
Direct identification in SEM-confirmation by XRMA	High atomic number elements identified as bright areas in BEI-mode	Non-destructive
FIB-SEM	Micro-surgery or micromanipulation of particles	
Characterization		
Scanning electron microscopy with XRMA	Size distribution, surface morphology, elemental composition and distribution	Non-destructive
Analytical TEM (transmission electron microscopy)/STEM with XRMA, electron diffraction, EELS, HAADF	Size distribution of colloids. Element composition, crystalline structure, chemical bonding and Z-contrast imaging	Often time-consuming sample preparation, thin sections prepared by ultra microtome
Nano- and micro focused XRF	Elemental composition and 2D distribution (depth information)	Non-destructive
Confocal μ -XRF	Elemental composition and 3D distribution	Non-destructive
Nano- and micro focused XANES	Oxidation state (distribution)	Non-destructive, synchrotron based
Nano- and micro focused XRD	Crystallographic structures	Non-destructive
Nano- and micro focused tomography	Spatial distribution of density, elements, ox. states	Non-destructive, laboratory based (nano-CT) or synchrotron based
EXAFS	Structure of non-crystalline materials	Synchrotron based

Table 4 shows a comprehensive list of tools available in the identification, isolation, and characterization of hot particles. Firstly, to identify the presence of such particles, it is often useful to use standardized techniques to detect elevated levels of radioactivity. Typically, this includes gas ionization, scintillation, and semiconductor detectors (usually [high-purity germanium \(HPGe\)](#)) [23]. Gas ionization detectors are cheap and readily available, however, they are only really useful for detecting α - and β -radiation, due to their low absorption efficiency of γ rays. The efficiency of scintillation detectors (usually NaI(Tl) or CsI(Tl)) is orders of magnitudes better, however, they suffer from low energy resolution and are thus less useful for isotope

identification than their semiconductor counterparts like the HPGe detectors. Checking for the presence of elevated levels of radiation, together with some rudimentary information about the activity's distribution, is the starting point for further research. It is also possible to use (digital) autoradiography for this part, since it can much more accurately give information about a particles location combined with a high efficiency for α - and β -particles.

Autoradiography is the oldest technique to detect and analyze the activity and distribution of radioactive material in environmental samples in general. For example, it has been used to look for radiation after nuclear weapons tests, but also extensively after the Chornobyl nuclear accident and its associated fallout. It works by placing a sample very close to a photographic film sensitive to alpha and beta radiation. The film then gets exposed by the radiation emitted from any hot particles inside the sample. After the exposure, the film is developed or digitally scanned and the exposed spots can be viewed. Due to its simplicity and spatial resolution, it is still extensively used today. A further development of this technique is electronic autoradiography using phosphorous image system, which enables viewing the radiation in real time. This makes the whole process a lot faster and it is easier to determine points of interests [23].

Gamma spectrometry is a simple way to identify all gamma-emitting radionuclides in a bulk sample. Conventionally, it does not provide any spatial resolution, but due to the very high energy resolution of these devices (e.g., HPGe detectors) it can reliably provide the user with a list of contained isotopes and an accurate figure of each isotope's activity. It takes advantage of the discrete energy levels of photons often emitted by an atomic nucleus after a radioactive decay like alpha or beta decay. These photons are then partially captured in the detector volume⁵ and converted into a current pulse proportional to the incident photon's energy. After an energy calibration, the detector will be able to generate a pulse height histogram of energy over incoming photons, i.e., counts (per second). This is then used to identify the contained radioisotopes with their respective activity.

For aerosols, the standard practice for sampling is using aerosol filters with different types of filter material. There are even systems that are able to separate the aerosols into different size fractions altogether. These work by drawing in air through several inlets in a so-called *cascade impactor* arrangement (see table 4) to obtain detailed size distributions of the particles. Of course there are also lots of different sampling techniques to probe soil, sediment, and aqueous samples, some of which can also be seen in table 4. These range from using centrifuges to obtain different size fractions for soil samples, to using ultrafiltration and filter membranes for aqueous systems [23].

As for sample splitting, a simple way is to use fractionation for binary separations. In this process, the sample is split into two or more equal parts, which are then analyzed for their radioactivity. The most promising fractions are then split again and again, until a desired small fraction size has been achieved. In between these steps, the fractionated samples are analyzed using similar monitoring techniques as above, like autoradiography, gamma-ray spectrometry, or even by means of GM tubes and light microscopes [23]. This process has been shown to be fairly reliable in detecting hot particles in any given environmental sample as shown in a previous study [27]. Most importantly, the conclusion of the analysis in the study was two-fold:

1. The wider the frequency distribution of the activities of the hot particles (large relative standard deviation), the smaller the number of sub-samples necessary to detect the presence of hot particles with a given probability will be.
2. Unless there is a strong indication of the presence of a large number of hot particles in the original sample (i.e., $n < 5$), these will usually be detected with a probability $> 95\%$ by assessing 3 - 4 sub-samples.

On top of this, it was noted that it will not be effective to increase the precision of the activity measurements of the sub-samples at the expense of the number of sub-samples investigated [27].

⁵This, of course, depends highly on the geometry, self-absorption in the sample, and the efficiency of the detector material. It typically represents a Landau distribution.

After all that is done, particle isolation and manipulation can present a challenge in itself. Sufficiently large particles, that can be seen under the (light) microscope, are straightforward in that regard and can even often be extracted by hand using fine needles. However, it is much harder the smaller the particles are. In these cases, there are methods to analyze particles without the need for extraction like [scanning electron microscopes \(SEMs\)](#) and [transmission electron microscopes \(TEMs\)](#) together with various types of [X-ray fluorescence \(XRF\)](#), [X-ray diffraction \(XRD\)](#), and [X-ray absorption spectroscopy \(XAS\)](#) (see table 4) [23].

[SEM](#) and [TEM](#) both belong to the category of electron beam techniques. They work by directing a nanometer-sized electron probe at a sample and then analyzing either backscattered, secondary, or transmitted electrons. All of this information can then be used to produce a morphological image of the sample. Additionally, all kinds of emitted X-ray radiation from these processes can be detected as well, in order to obtain compositional information by using [wavelength-dispersive X-ray spectroscopy \(WDX\)](#) or [energy-dispersive X-ray spectroscopy \(EDX\)](#) directly built into the [SEM](#) assembly. In short, with [SEM](#) the electron beam can be focused down to a few nanometers and the elemental detection limits lie in the range of 0.1% ([EDX](#)) to 0.01% ([WDX](#)). The images produced by [SEM](#) have the best resolution in the micron and sub-micron range. [TEM](#) works by detecting the electrons transmitted through the sample and therefore only thin layers can be analyzed, making sample preparation a lot more of a challenge [23].

In order to extract very small hot particles, micromanipulation is a viable option. Simple manipulation can be done using a light microscope, a precision x-y-z specimen stage, and an x-y-z needle micromanipulator. These setups often contain traditional binoculars, stereo microscopes, or CCD cameras. Anyways, for this technique it is crucial to have precision-driven stages controllable by the micrometer. For these systems, there are two kinds of needles that can be used: metallic (e.g., steel, tungsten), and non-metallic (e.g., graphite, glass, plastic). The needle material must be chosen by the specific requirements of the sample, however, with non-metallic needles it is important to keep the effects of static electricity in mind during manipulation. To eliminate this potential issue, it is possible to coat the needle with a conductive layer like gold or platinum [23].

Even smaller hot particles can be manipulated in-situ using a [SEM](#). First and foremost, these devices function as a source to search for and identify potential candidates for said particles based on their size, shape, and elemental composition. These candidates can then be moved around and separated to be further studied on their own. With this, it is possible to transfer and extract adjacent microparticles or even airborne sub-micron particles from samples [23].

Lastly, it is also possible to use so-called *micro-surgery* on hot particles. This technique uses an energetic [focused ion beam \(FIB\)](#) to perform slicing and removing material from certain parts of the particles. The particle is shot with a precisely focused ion beam to make thin slices of the material, which can be examined layer after layer. It is a fast, but destructive way to examine the inner structure of particles similar to non-destructive μ -tomography, that uses X-rays to perform virtual slicing of the target [23]. Using a [FIB](#), it is also possible to slice away material in between adjacent particles that are attached to each other, or to cut free a single particle that has been somehow bonded to much larger, non-radioactive material.

1.3.3 Dosimetric Aspects

Particle bound radionuclides are often overlooked in radiation protection and dosimetry, because of their inherently different mobilization, weathering effects, and ecosystem transfer mechanisms. These all influence the biological uptake and effect, and as a consequence also the impact on human health. However, all of these properties make it very difficult to assess any dosimetric effects on the human body and has proven to be a complex issue. For this reason it is also a relatively new topic in the field of radiation protection and a lot of research still has to be done in order to fully understand the effects of all of these processes on human health and long-term ecological consequences [28, 23, 25]. In 2001, for example, there were no standard techniques

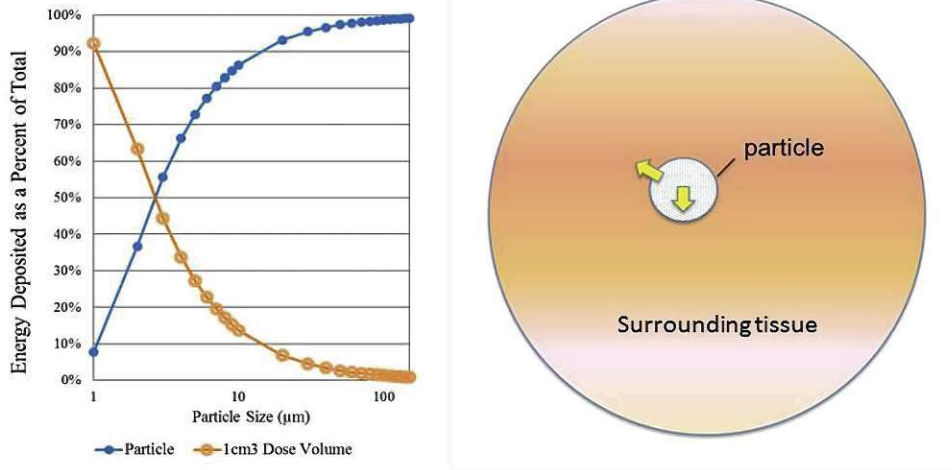


Figure 9: Model data indicating, for a range of particle sizes, the relative fraction (%) of alpha emission energy that is deposited within a Pu-containing particle (blue symbols) versus that deposited in surrounding tissue (orange symbols). The Pu was assumed to be homogeneously distributed within a spherical particle. **Source:** [25], adapted from [29]

available to collect, isolate, and measure radioactive particles found in the environment. On top of this, little to no information about the distribution, transport, and bio-availability were available at this time [23].

Arguably the greatest health risk comes from incorporation of radioactive particles, primarily through inhalation, but also dermal absorption, wound exposure, and ingestion of the particles [25]. Due to their small size, often in the micron ($< 10 \mu\text{m}$) or even submicron range, they are respirable and can potentially penetrate deep into the lungs similar to fine atmospheric particulate matter. This significantly decreases their chances of being expelled again using coughing or through similar processes, resulting in possible long-term effects on the lung and surrounding tissue. Another issue with micron-sized particulate is the fact that if they contain alpha emitters, no significant self-absorption will be able to reduce the impact of the radiation. Additionally, due to the inherently discrete nature of the emitters, radiation effects from hot particles are distinct from commonly known homogeneous contamination, so dose calculations have to take into account the point source radiation [28]. A model calculation of the relative change in self-absorption for a single Pu-containing particle (homogeneous distribution) inside the surrounding tissue is shown in figure 9. It is clearly visible that the energy deposited in the particle itself increases nearly exponentially with an increase in particle size. Most importantly, for particle sizes less than $10 \mu\text{m}$, i.e., particles that are considered respiratory, self-absorption significantly decreases with every further reduction in particle diameter.

In the following section 1.3.4 and onward, a selection of the most prevalent sources of radioactive particles will be presented, starting with one of the most well-known and earliest origins: nuclear weapons tests.

1.3.4 Nuclear Weapons Tests

Atmospheric, ground surface underground, and underwater nuclear tests represent the largest source of global radiological contamination and are the major contributors to radioactive particles in the environment [23, 25]. Most tests were conducted by only a handful of nations during the height of the cold war up until the turn of the millennium. Key areas where these weapons tests were conducted, grouped by nation, are as follows [23]:

- **USA:** Nevada test site (US), Marshall Islands (current Republic of the Marshall Islands)

- **USSR:** Semipalatinsk (Kazakhstan), Novaya Zemlya (current Russian Federation)
- **France:** Mururoa and Fangataufa atolls (France)
- **UK:** Maralinga and Emu sites (Australia)
- **China:** Lop Nor (China)

Table 5: Radionuclides produced and globally dispersed in atmospheric nuclear weapons testing. **Source:** [23]

Radionuclide	Half-life	Global release [10^{18} Bq]
^3H	12.33 a	186
^{14}C	5730 a	0.213
^{54}Mn	312.2 d	3.98
^{55}Fe	2.73 a	1.53
^{89}Sr	50.6 d	117
^{90}Sr	28.5 a	0.622
^{91}Y	58.5 d	120
^{95}Zr	64.0 d	148
^{103}Ru	39.25 d	247
^{106}Ru	365 d	1.22
^{125}Sb	2.73 a	0.741
^{131}I	8.04 d	675
^{137}Cs	30.0 a	0.948
^{140}Ba	12.75 d	759
^{141}Ce	32.5 d	263
^{144}Ce	285 d	30.5
^{239}Pu	24110 a	0.0065
^{240}Pu	6560 a	0.19
^{241}Pu	14.4 a	0.142

At most of these locations, atmospheric and underground nuclear tests were performed, as well as so-called *safety tests* that produced little to no nuclear yield and only dispersed the radioactive material contained in the warheads (i.e. ^{239}Pu and ^{235}U) with conventional explosives. The total amount of radionuclides produced and globally dispersed can be seen in table 5 [23]. Most of it is in the form of quite short-lived radionuclides.

In the former USSR, 456 nuclear weapons tests for military purposes were conducted between 1949 and 1989 at the Semipalatinsk site alone. These produced spherical, reddish brown or black radioactive particles with diameters of up to $15\ \mu\text{m}$ that could be detected as far away as in Japan. Similar particles from nuclear test fallout originating at the same site and containing plutonium could be found in Norway [25].

A more recent study conducted at the site investigated two radioactive fallout plumes generated by a low-yield surface nuclear test and a surface non-nuclear experiment with little to no nuclear energy release. Typically, in areas affected by global fallout, the adsorbing radionuclides like Pu are mainly associated with the finest soil fractions. In contrast to this, the study found that the highest activity concentrations can be found, in fact, in the coarse soil fractions along

both analyzed plumes. At the plume of the nuclear surface test, the radionuclides were concentrated mainly in the 500 - 1000 μm soil fraction, while at the plume of the non-nuclear test, they were concentrated in the 250 - 500 μm soil fraction. The enrichment in the coarse fractions can therefore be understood as a result of the presence of radioactive particles from the nuclear tests [30]. In soil samples at ground zero, the Balapan, and Degelen glass-like particles have been found. Small grains ($O(10\mu\text{m})$) with highly concentrated U and Pu were found in soil particles at the Tel'kem craters [25].

The United States performed 23 atmospheric and ground-level nuclear weapons tests between 1946 and 1958 at the Marshall Islands. Particle characteristics such as size distribution, shape, and color depended on the device and shot conditions according to one study [31]. Autoradiographic analysis revealed large spherical particles (0.5 - 1 mm) and Si-O-rich particles containing plutonium. Additionally, between 1951 and 1992, 86 atmospheric and 828 underground nuclear weapons tests were performed at the Nevada Test Site in the US. Most of the radionuclides produced in the underground tests were incorporated into melted glass according to another study [32]. The resulting particle's properties were found to vary largely in size, shape, color, specific activity, density, and magnetic properties. They have been found in fused or partially fused states and even as larger agglomerates with the mentioned differing characteristics [25].

The French nuclear tests in French Polynesia resulted in relatively large Pu-containing particles as well, roughly ranging from 100 - 1000 μm . From the French tests in Algeria, no information about particle characteristics is available [25]. In general, it is safe to say that a lot more research needs to be done in order to investigate the particulate produced by all kinds of nuclear weapons tests [25, 24].

1.3.5 Nuclear Weapons Accidents

Today we know about quite a large number of accidents that involved nuclear weapons and resulted in them being conventionally destructed, damaged, or entirely lost. Arguably most of those involved US military aircraft, especially during the height of the cold war. The two most well-known incidents are probably the Palomares and the Thule accidents. Both were very similar in nature and incidentally involved armed B-52 Stratofortress bomber aircraft on missions for the US' Operation Chrome Dome over non-US territory in Europe and the Arctic.

The Palomares accident occurred on January 17, 1966. A B-52 bomber aircraft armed with four thermonuclear warheads was on an air-to-air refueling rendezvous with a KC-135 Stratotanker when the two planes collided, snapping off the left wing of the bomber. The subsequent explosion resulted in seven fatalities out of the eleven crewmen, a total loss of both aircraft, and all four thermonuclear weapons falling to the ground. Two of the warheads were eventually recovered intact⁶, however, the conventional explosives inside the other two bombs detonated, which distributed large amounts of Pu-U particles over an area of 2.3 km² on the southeastern coast of Spain near the town Palomares. 1400 tons of contaminated soil and vegetation were excavated and transported to the US by sea [25].

The Thule accident occurred on January 21, 1968, almost exactly two years after the prior accident. A bomber, again, carried four thermonuclear warheads with seven crew members on board. After a heater malfunction, the plane caught fire and six of the seven men bailed out of the aircraft over Thule airbase, Greenland. The pilotless aircraft continue to fly until it crashed into the ice about 12 km west of the airbase. The conventional explosives and the fire resulted in the dispersion of Pu-U particles. The geometrical mean diameter of the particles' size distribution at Thule was 2 μm , but the majority of all activity was held in only a few larger particles of 10 - 1000 μm size. They were found to contain largely of uraninite (UO_2) with no traces of metallic Pu and Pu(VI) [25].

⁶One of the two warheads that was recovered intact was only found almost two months after the incident on the seabed of the Mediterranean.

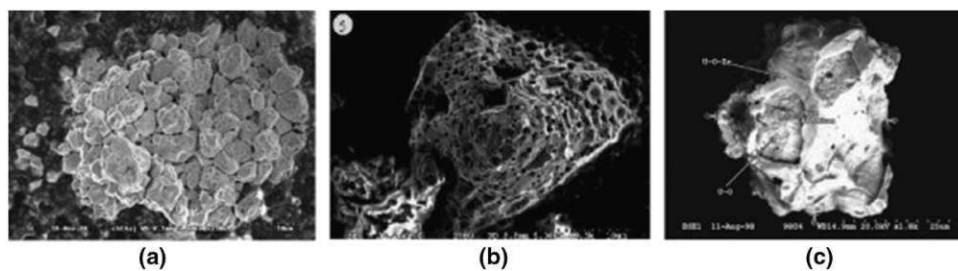


Figure 10: SEM images of fuel particles found in Chernobyl's Red Forest: **a)** UO_2 fuel particle; **b)** oxidized UO_{2+x} fuel particles; **c)** ZrU_yO_x fuel particles. **Source:** [24], originally taken from [35]

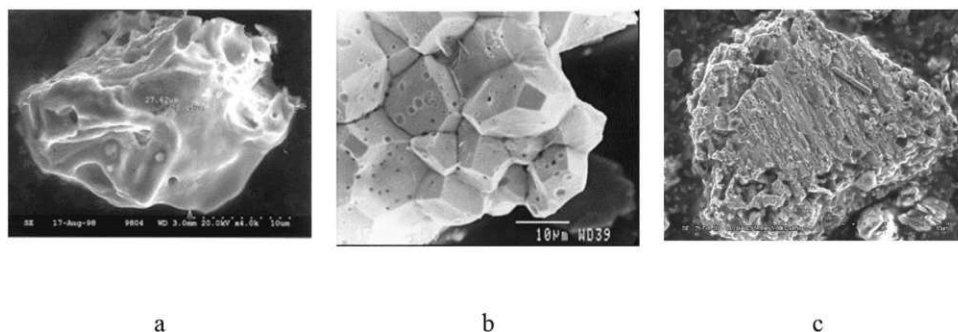


Figure 11: SEM images of fuel particles: **a)** ZrU_yO_x fuel particles; **b)** UO_2 fuel particles; **c)** UO_{2+x} fuel particles. **Source:** [36]

1.3.6 Chernobyl Nuclear Accident

The Chernobyl nuclear accident occurred on April 26, 1986, northwest of the city of Chernobyl, formerly part of the USSR, now part of Ukraine. It is only one of two nuclear accidents rated at the maximum severity on the [International Nuclear Event Scale \(INES\)](#) and remains by far the most catastrophic civilian nuclear disaster to date. Following a series of unfortunate decisions made by the plant staff, a massive explosion occurred in reactor Unit 4 and together with the resulting graphite core fire released massive amounts of nuclear fuel in the form of small particles ranging from 1 - 100 μm in size. In total, a staggering amount of 5300 PBq (excluding noble gasses) were released at Chernobyl [24, 33]. About 3 - 4 tons of uranium fuel from the reactors were released into the atmosphere, either as fuel particles, particles containing construction material, or condensation particles [25].

Particles of 5 - 35 μm in size can still be frequently encountered in the surrounding area of the [Chernobyl exclusion zone \(CEZ\)](#), especially in the so-called *Red Forest*. Fallout from the accident could be registered in large parts of Europe and to this day there are still regionally measurable levels of ^{137}Cs in the soil from the Chernobyl fallout, especially enriched in mushrooms and wild boar populations. In fact, radiocaesium contamination in wild boars can sometimes still exceed the regulatory limits. A recent study concluded that ^{137}Cs from the Chernobyl disaster (as well as from nuclear weapons tests) still disproportionately affects wild boar populations at persistently elevated levels [34]. The accident also released large amounts of sub-micron ($<1 \mu\text{m}$) particles, so-called *condensation aerosols* that exhibit enriched radiocaesium activities.

The particulate matter from the original fallout can be categorized into three main groups according to their composition [25, 24], taken directly from [24]:

- Fuel particles (UO_2) that originated from the mechanical fragmentation through the explosions and emitted on 1986/04/26. These particles, together with volatile fission products, formed the 'western trace' and were blown into the area of the 'Red Forest'. These particles are chemically relatively stable.

- Oxidized fuel particles (UO_{2+x}) that formed during the graphite fires of the burning moderators between 1986/04/26 and 1986/05/05. They have a UO_2 core surrounded by a layer of $\text{U}_2\text{O}_5/\text{U}_3\text{O}_8$ and exhibit high dissolution rates. They were distributed along the northern and southern traces of the Chernobyl fallout.
- Fuel particles embedded into a zirconium matrix (ZrU_xO_y) that originated through annealing of UO_2 fuel with zirconium materials inside the molten reactor core. They are chemically rather inert and exhibit low dissolution rates. These particles are relatively rare. They are believed to have formed in the initial phase of the accident and have spread along the western trace.

In the SEM images of figures 10 and 11, the three categories of particles are shown. They are clearly of different morphological nature hinting to their distinctive production processes.

Fuel particles pose an inherent environmental and health hazard, however, they can also mobilize radionuclides by processes of weathering and dissolving. These processes depend largely on each individual particle's chemical nature and chemical features of its environment. This changes the likelihood for weathering and corrosion. For example, a higher soil acidity increases the dissolution rate of the particles [24].

Since the accident, most of the hot particles and radioactive material have been disintegrated by weathering over the years. In fact, the radiological situation in the so-called *fuel paths* of the fallout had already reached a stable state by 2004. One novel source of hot particles is the cooling pond of the nuclear power plant that forms a large reservoir, especially in the sediments. The total water volume of the pond, at the time of the accident, was $150 \times 10^6 \text{ m}^3$ and it is located about 7 m above the water level of the nearby Pripjat river. At the time of operation, the pond had to be constantly filled with water from the river by electric pumps. Since the shutdown of the last operating reactor in the year 2000, the cooling pond lost its purpose and was consequently shut down fifteen years later in 2015. In the time since, the pond has already dried up significantly and a large amount of hot particles originating from the initial fallout after the explosion are at risk of being removed from their anoxic environments. They are going to become exposed to atmospheric oxygen and undergo chemical alterations and weathering [24].

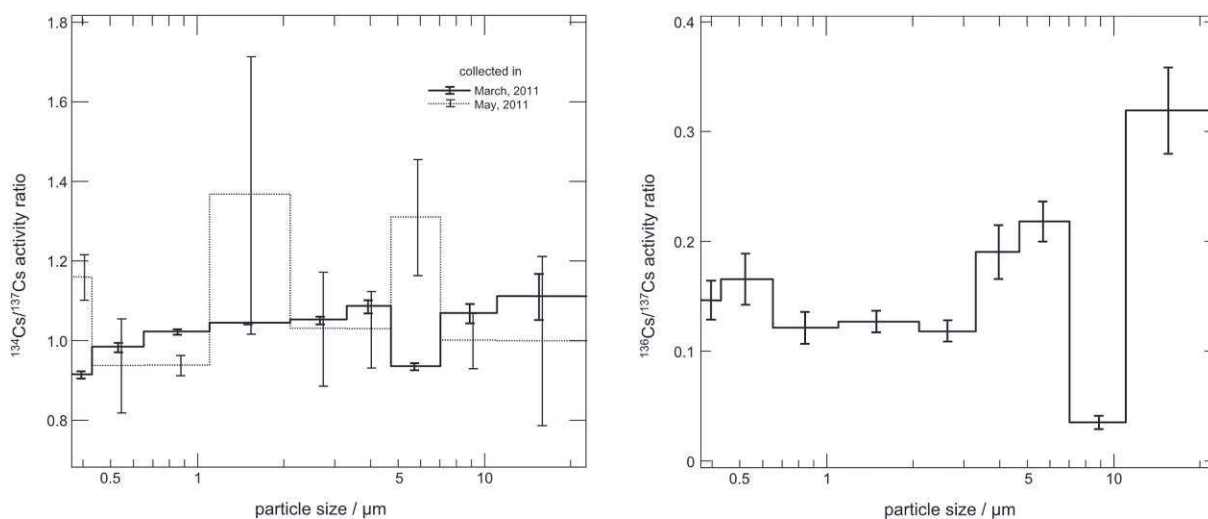
The yearly corrosion rate of the environment is expected to more than double and the acidification of the former sediments will contribute to an increased dissolution rate. The newly exposed particles are expected to disintegrate within 15 - 25 years, while those in the flooded parts of the cooling pond will probably remain stable for another 100 years. In short, this is expected to lead to a significant secondary contamination of the immediate area [24].

1.3.7 Fukushima Nuclear Accident

The Fukushima Daiichi nuclear accident in 2011 barely compares to that of Chernobyl, even if both are rated at the maximum level of the INES scale. In both accidents, most of the radioactive release was due to volatile radionuclides (noble gases, iodine, caesium, tellurium), however the amount of refractory elements (including actinides) emitted at Chernobyl was roughly four orders of magnitude higher than at Fukushima. The total release at Fukushima was estimated to be around 250 PBq, while for the Chernobyl accident it was 5300 PBq (excluding noble gases) as mentioned in the previous section 1.3.6. The majority of all radionuclides (>80%) were deposited in the Pacific Ocean [33]. In contrast to Chernobyl, where 0.4% of the total nuclear fuel inventory of the single affected reactor was emitted, only about 150 g were released at Fukushima [24]. In fact, in a study, the quantities of U and $^{239+240}\text{Pu}$ emitted to the atmosphere were estimated as $3.9 \times 10^6 \text{ Bq}$ (150 g) and $2.3 \times 10^9 \text{ Bq}$ (580 mg) respectively [37].

The lasting environmental impact at Fukushima after the accident was observed to be much less severe than that of Chernobyl. Both the highly contaminated areas and the evacuated areas (difficult-to-return zones) are much smaller around FDNPP than around the Chernobyl nuclear power plant (e.g., CEZ). On top of this, the projected health effects in Japan after the accident are significantly lower too. The evacuations and food safety programs in Japan almost do not

compare to those at the time in Chernobyl in the USSR – they worked a lot quicker and more efficient after the FDNPP accident [33].



(a) Variation of $^{134}\text{Cs} / ^{137}\text{Cs}$ activity ratio with particle size. The solid lines show the variation for the samples collected in the period of March 17 - April 1, 2011, and the dotted lines show those collected in the period of May 9 - 13, 2011.

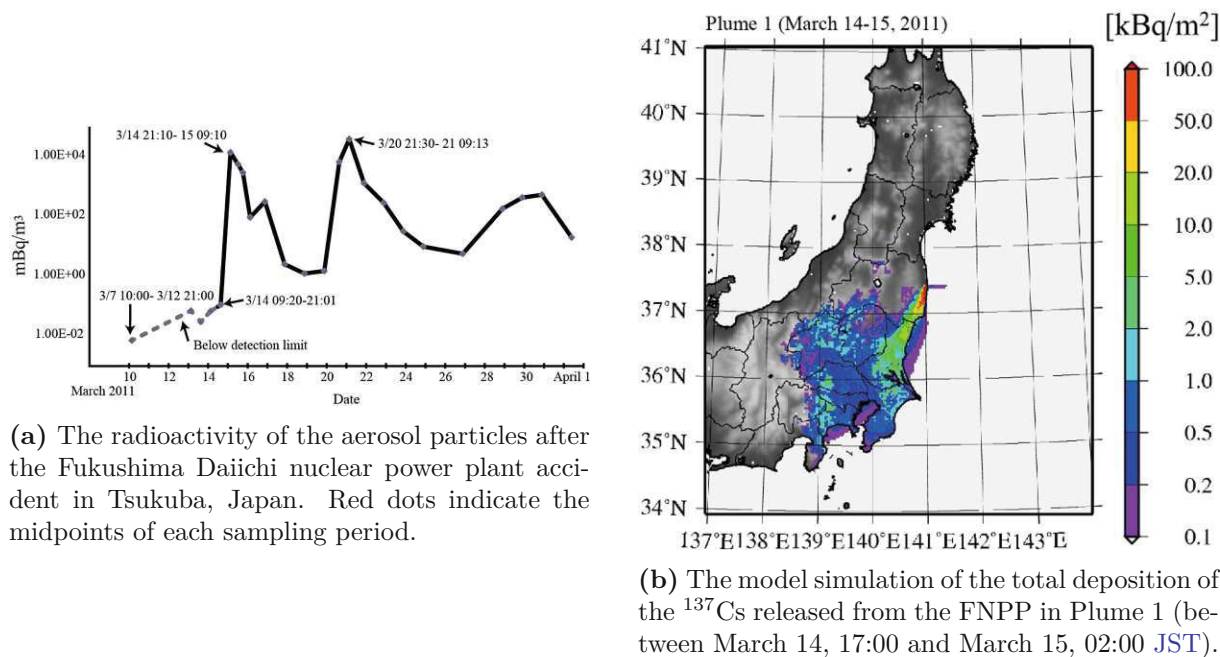
(b) Variation of $^{136}\text{Cs} / ^{137}\text{Cs}$ activity ratio with the particle size.

Figure 12: Overview of the located particle sizes compared to the activity ratios of different Cs isotopes. The activity ratios are calculated as of March 11, 14:46 (JST), 2011, just when the earthquake occurred. **Source:** [38]

Shortly after the nuclear accident, airborne radioactive particles were collected at a short distance from FDNPP. They were found to contain ^{134}Cs , ^{136}Cs , ^{137}Cs , $^{129\text{m}}\text{Te}$, and ^{140}Ba with an activity median aerodynamic diameters (AMADs) of 1.5 to 1.6 μm and ^{131}I with an AMAD of 0.45 μm . The size AMAD distributions depending on the Cs isotope ratios are shown in figure 12. One thing of notice is the fact that, after two months, the AMAD of ^{134}Cs and ^{137}Cs significantly changed to three distinct peaks suggesting a change in the specific carriers of the activity. Also, the $^{134}\text{Cs} / ^{137}\text{Cs}$ ratio of dust collected in March 2011 decreased with particle size [38].

A novel type of radioactive particle observed after the FDNPP accident was glassy spherical caesium-bearing microparticles (i.e., CsMPs). The presence of these particles during the early stage of the accident was first observed in a study that remarked two very distinct radioactive plumes [39]. This is shown in figure 13a for the time between the accident date and April 1st. They were approximately 2 μm in diameter and contained large amounts of Si, Fe, Zn, and some other elements. The distribution of these elements inside the particles was found to be entirely evenly, which means that they must have been internally mixed, forming some sort of alloy. Furthermore, the particles are solid and largely water-insoluble, resulting in more dry deposition and less contamination of the region north-west to FDNPP. This can be seen in figure 13b, where the first major plume deposition of radioactive material has been simulated. At the time of the study, it also seemed probable that the emission processes between plume 1 and plume 2 had changed, due to the way the accident proceeded.

The most dominant atmospheric releases could be determined in another study on a per-unit base [40]. In the afternoon of March 12, 2011, the first major source was Unit 1. After that came Unit 2 during the late night of March 14, to the morning of March 15, 2011. From the evening of March 15, 2011, the major source reactors were Unit 2 and 3. These all correspond to the first plume, i.e., a peak in activity as can be seen in figure 13a. The major source of the second plume was Unit 3 on March 20, 2011, with a temporary change to Unit 2 [40].



(a) The radioactivity of the aerosol particles after the Fukushima Daiichi nuclear power plant accident in Tsukuba, Japan. Red dots indicate the midpoints of each sampling period.

(b) The model simulation of the total deposition of the ^{137}Cs released from the FNPP in Plume 1 (between March 14, 17:00 and March 15, 02:00 JST).

Figure 13: Emission of radioactivity in the form of aerosol particles shortly after the nuclear accident in distinct two plumes with the respective planar distribution. **Source:** [39]

Another type of hot particle observed after the accident are caesium-rich sulfate aerosols in the sub-micron range. They are significantly smaller ($<1\ \mu\text{m}$), hydrophilic, and also water-soluble. They are thought to have formed outside of the reactor buildings from March 20 - 21 with the first plume [39]. These sulfate aerosols share some similarities with the condensation aerosols from Chernobyl that were quickly mentioned in the previous section 1.3.6, hence it is possible that the formation processes in the atmosphere are similar as well [24].

Three key topics of research were defined that are closely coupled to the emitted particles [39]:

1. The composition and the spherical shape of the Cs-bearing particles emitted by the FDNPP accident will be a key to understand what happened in the nuclear reactors during the accident.
2. The spherical Cs-bearing particles likely have longer retention times on the land surface than those of the water-soluble Cs particles. The retention time of the particles in the soil or other environments needs to be reconsidered.
3. The health effects of the particles should be evaluated based on the particle sizes and insolubility in water.

These glassy, water-insoluble, and relatively stable CsMPs are the topic of research in this thesis and will be discussed more in-depth in section 1.4.

1.3.8 Other NPP Accidents

There are, of course, other accidents revolving around nuclear power plants that were less severe than Chernobyl and Fukushima. For example the Windscale fire in the United Kingdom and the core melt down at the Three Mile Island nuclear power plant in the US.

The Windscale Piles were two nuclear reactors at the Windscale nuclear site, now Sellafield, UK. They were part of the British early cold-war effort to produce weapons-grade plutonium for their nuclear arsenal and were operational between 1950 and 1957. To produce the material as quickly and efficiently as possible, the reactors were air-cooled, graphite-moderated, and the

exhaust air was simply filtered and expelled through a stack. The nuclear fuel used at the time was natural uranium oxide. During operation, the graphite moderator combusted and a fire broke out that led to the dispersion of large amounts of radioactivity in the surrounding area, the UK, and Continental Europe. It is estimated that around 12 kg of uranium, 740 GBq ^{137}Cs , 666 GBq ^{90}Sr , and 11.1 GBq $^{239+240}\text{Pu}$ were emitted. The particles from the accident were quite large with 85% of the particles by weight being between 10 and 100 μm in diameter. They mostly fell within a few km of the site and led to a severe increase in ^{137}Cs and ^{90}Sr levels in milk [41]. To this day, there is still a large ongoing effort to decontaminate the beaches in the surrounding area. In the past, proposed methods to detect this particulate matter included low flying helicopters equipped with large-volume NaI(Tl) detectors in order to conduct rapid air surveys [42].

The core melt down accident at the Three Mile Island nuclear power plant in the United States happened on March 28, 1979. At the site, two PWR reactors were utilized, one of which was involved in the accident. During maintenance work issues with some of the valves eventually resulted in a LOCA that led to the partial melt down of the reactor core. Due to proper containment, no particulate material was released, but volatiles such as noble gases were, in fact, emitted to the environment. The estimated total atmospheric release for the accident was 10^{12} Bq, which is around six orders of magnitude lower than the emissions at Chernobyl [23].

1.3.9 Releases from Reprocessing Plants

In the past, reprocessing plants were a major source of environmental (radioactive) pollution. Up until the 1990s, the liquid effluents from reprocessing were responsible for the majority of the global collective dose commitment of nuclear power generation. At times, radioactive waste solutions were simply discarded and dumped into nearby rivers or into the sea [23].

The Mayak Production Association was the first and still is one of the largest nuclear facilities in the Russian Federation. In the past, it was used to produce weapons-grade plutonium for the Soviet nuclear program, and now it allegedly specializes in the reprocessing of spent nuclear fuel. Between 1949 and 1951, 10^{17} Bq of liquid radioactive waste were released into the nearby Techa river. In addition to this, around 4.4×10^{17} Bq of other waste were also released into a lake near the site. Later, due to a severe drought at the lake, a tornado was able to disperse large amounts of this radioactive material that was originally suspended in sediments. Lastly, the Mayak Production Association was responsible for the third largest nuclear accident ever according to the INES scale, when a tank exploded and dumped approximately 74 - 740×10^{15} Bq of radioactive liquid sludge into the environment, contaminating roughly 15,000 to 23,000 km^2 of land [23]. This is now more widely known as the *Kyshtym disaster*.

Similar accidents also happened in other reprocessing plants in the Russian Federation. At Seversk (Tomsk-7), the Siberian Chemical Combine contaminated the river Tom. The reprocessing plant in the Tomsk-7 military complex ejected radioactive solution into the environment when a tank containing a U-Pu solution exploded in 1993. Severe contamination and a diversity of hot particles were also observed in the river Yenisey, following the release of effluents from the Mining and Chemical Combine in the closed city of Zheleznogorsk, Krasnoyarsk-26 [23]. This was Russia's largest producer of weapons-grade plutonium and the site operated three reactors. Most of the radioactive particles found in the river were fuel particles and could be traced back to three formation time intervals. Some particles were found to contain differing plutonium isotope ratios, while others only contained several activation products. Possible sources include cobalt particles from the corrosion of a reactor coolant system and europium particles from damaged compensating rods. SEM images of typical fuel particles from this region that were investigated in a study are shown in figure 14 [43]. The contaminated region exhibits a unique diversity of hot particles that makes it special for studying their environmental effects.

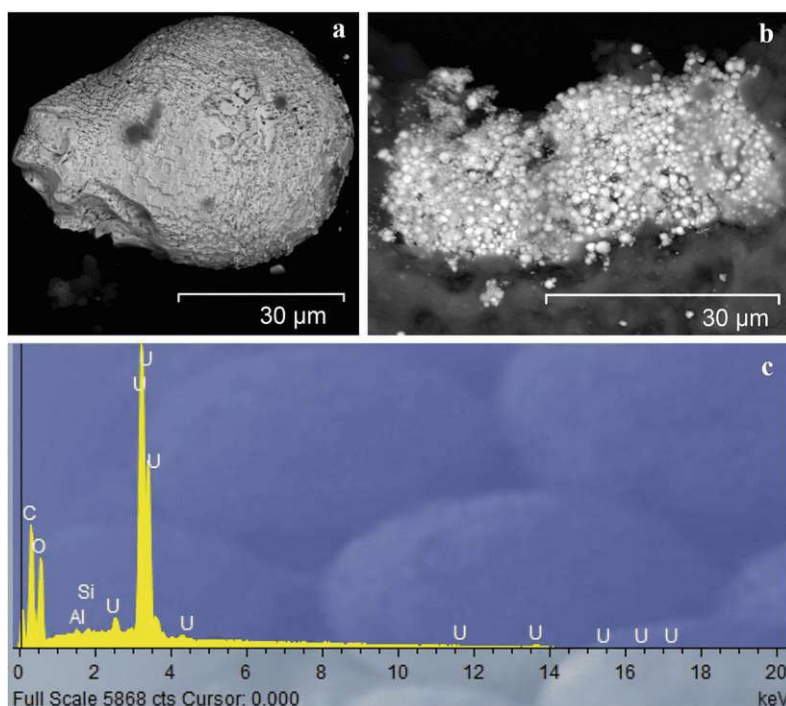


Figure 14: SEM images of some of the typical Yenisei fuel particles that were investigated: (a) an individual particle; (b) a conglomerate of particles; (c) a typical X-ray spectrum of fuel particles. **Source:** [43]

1.3.10 NORM Sources

Naturally occurring radioactive materials (NORMs) can also be a source of radioactive particles, even if largely ignored in literature due to their natural occurrence. Mostly, these particles are distributed in minerals and contain, of course, the naturally occurring radionuclides ^{232}Th , ^{235}U , ^{238}U , and all of their respective decay products. These can be released in the form of particulate matter at mining sites or from tailing areas [25]. Health risks mostly only originate from the immediate locations with an accumulation of these natural minerals like the ones just mentioned. Special care must be taken when handling these particles, because they possibly contain a large concentration of alpha emitters.

Another source of radioactive particles that is often overlooked are coal-firing thermal power plants. While not particularly concerning in terms of a health hazard by the radiation, these power plants release very fine particles that contain NORMs as well and are less efficiently removed by the electrostatic precipitators and other filters [44]. In fact, it is thought that the majority of the 1.48 TBq globally released per year is in the form of fine particles or aerosols [26]. The estimated additional effective dose due to incorporation of these particles, however, is predicted to be only 220 μSv after 30 years in a worst case scenario [44].

1.4 CsMPs from the FDNPP Nuclear Accident

1.4.1 Overview and Types

Caesium microparticles (CsMPs) are unique microparticles with distinct morphology, elemental composition, and a high specific radioactivity. Like briefly explained in the earlier section 1.3.7, they are distinctly different from any other type of hot particles, especially those of Chernobyl. In short, they are glassy, rounded or spherical particles that were once molten and primarily contain elements such as Si, O, Fe, and Zn upon others. Most importantly, though, they contain highly concentrated radiocaesium (^{134}Cs and ^{137}Cs). Currently, they are believed to have formed in the **high-efficiency particulate air (HEPA)** and **pre-HEPA** filters of the **SGTS** inside the different reactor units. In past publications, an effort was made to classify these particles and provide a system for categorization, which resulted in five different **CsMP** types at the time of writing [45, 46]. Understanding these hot particles can provide valuable information about what went down in the nuclear reactors and **RBs** at the time of the accident, especially related to their origins. They also play a key role in understanding the long-term consequences of the contamination of the countryside surrounding the **FDNPP** site, as well as their effects on human health. This section will give an overview of all of the different particle types that were identified, as well as their likely origins and formation processes. Lastly, I want to provide a brief view into the latest research that has been done.

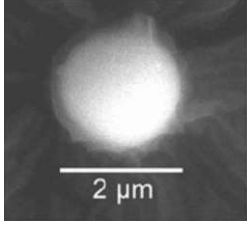
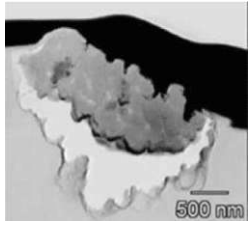
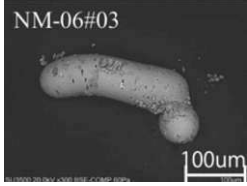
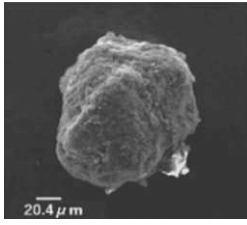
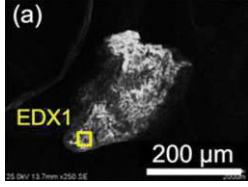
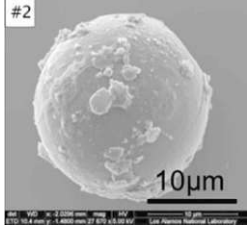
Table 6 summarizes all the five different types of **CsMP** known to this date. In general, they are less than half a millimeter in diameter. Other than this, there practically exists a type of **CsMP** for every order of magnitude in size, which makes the process of categorization much more complex. In terms of morphology, the particles can be perfectly round, but also non-spherical with even more intricate shapes. One study has specifically researched the structures of non-spherical **CsMPs**, and they concluded that the **FDNPP CsMPs** are of considerable variety and the structures likely change with time in the field [48]. It is therefore not easy to identify these particles on morphology alone. As shown in table 6, the least radioactive particles are the Type E particles with only $O(10\text{ mBq})$ per particle. In contrast, Type A has a smaller average diameter, while having at least 10x the radioactivity per particle. The typical places of discovery for all of these particles are in the main plumes, especially to the west and north of **FDNPP**. In terms of expected origins, they are mostly suspected to have formed in the **HEPA** and **pre-HEPA** filters of the power plant buildings' **SGTS** either due to condensation or – more likely – due to atomization of the filter material, more on the formation processes will be discussed later.

An important thing to note here is that the origins of Type C to Type E particles were predicted based on the origins of Type A and B, and this has yet to be supported by a number of additional studies [45]. Type A and Type B particles are by far the most researched types of the **FDNPP CsMPs**. Due to all of the complex properties, it can be much harder to categorize particles which diverge from this prospect.

Because knowing the morphology and elemental composition of **CsMPs** is of vital importance in identifying them in a sample of possible dozens of other unrelated particles, a selection of **SEM** images from a number of studies together with their respective **EDX** spectra or maps are shown in the following figures 15, 16, 17, 18, and 19. This list is, of course, not at all comprehensive, but it serves to give an overview over all the different publications of the past years. In these figures, a multitude of different shapes and sizes of **CsMPs** are presented, which shows their complexity in practice. Most of these contain significant amounts of Si, Fe, and Zn – some contain Ti and Ca, and in some cases the Cs itself could be observed. Figures 15, 16, and 17 specifically represent Type A and B **CsMPs**.

Figure 19 is from a more recent study that analyzed **CsMPs** from the insides of a school building located 2.8 km south-west of **FDNPP**. Hot particles accumulated at the entrances of the deserted building with a radioactive fraction of **CsMPs** to bulk indoor dust (RF) as high as 38.9% [54].

Table 6: Types A - E caesium microparticles (CsMPs) observed after the FDNPP accident. Source: [45], adapted to fit the notation of this thesis.

	Type A		Type B
Reference picture			
Diameter [μm]	2 - 2.6	1 - 5	70 - 400
Radioactivity [Bq/particle]	0.66 - 3.27	0.56 - 1.94	10 ¹ - 10 ⁴
Shape	Spherical	Non-spherical	Non-spherical
Observed location	Tsukuba, Tokyo, NW of FDNPP	W, NW of FDNPP	N of Unit 1, FDNPP
¹³⁴ Cs/ ¹³⁷ Cs	≈1.04		≈0.93
Expected origin	Main HEPA filter in Unit 3		Insulator in Unit 1 RB
References	[46, 47]	[48]	[46, 49]
	Type C	Type D	Type E
Reference picture			
Diameter [μm]	120	≈400	12 - 23
Radioactivity [Bq/particle]	224 ± 3	0.52 - 1.94	0.011 ± 0.008
Shape	Non-spherical	Non-spherical	Spherical
Observed location	3 km SW of FDNPP	4 km NNW of FDNPP	W, SW of FDNPP
¹³⁴ Cs/ ¹³⁷ Cs	1.02 ± 0.04	0.954 - 0.971	N/A
Expected origin	Pre-HEPA filter in Unit 3	(Pre-)HEPA filter in Unit 1	HEPA filter in Unit 4
References	[50]	[51]	[52]

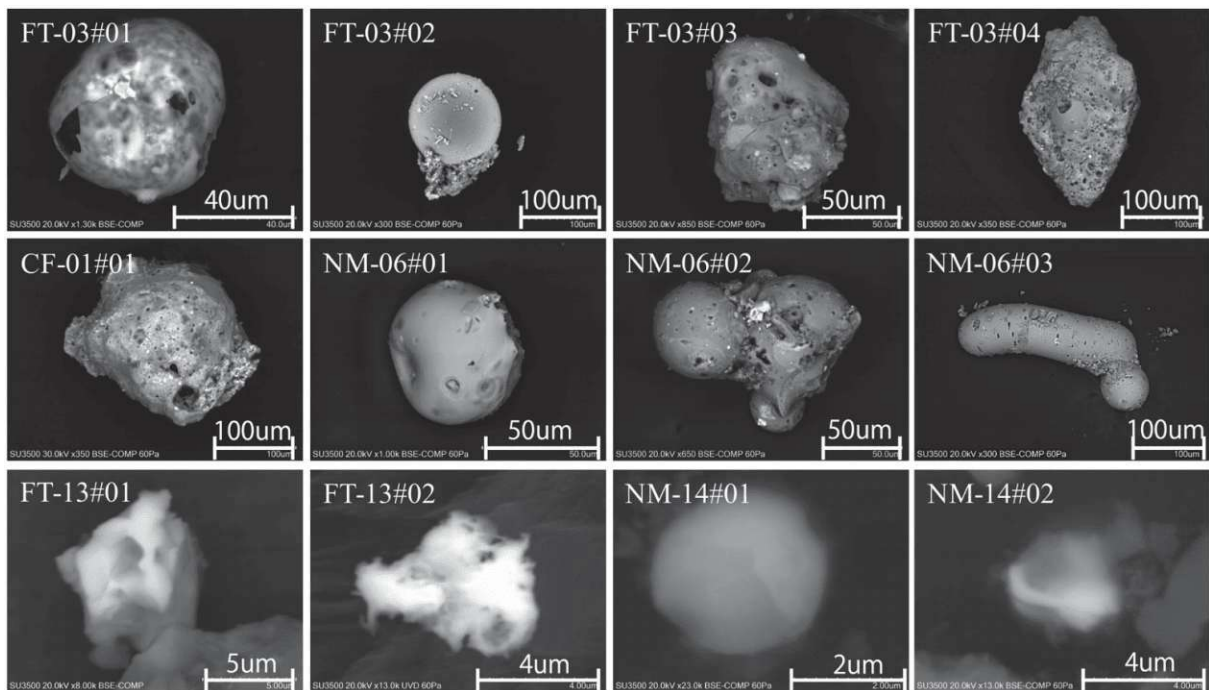


Figure 15: Backscatter electron images of representative radioactive CsMPs from environmental samples collected around FDNPP. **Source:** [49]

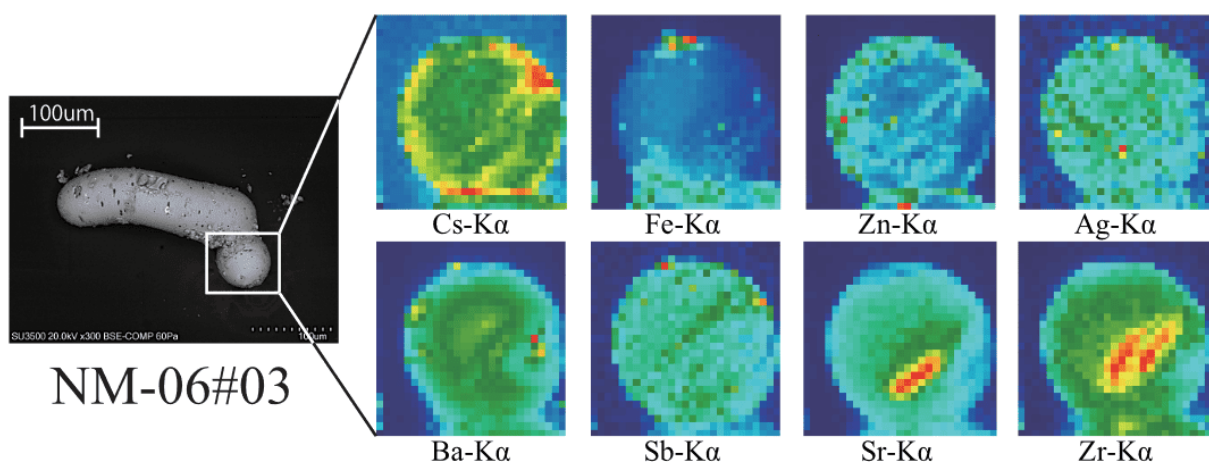


Figure 16: Micro-beam maps of elemental distributions on a CsMP, showing uneven patterns across its surface. **Source:** [49], with data reconstructed from [47]

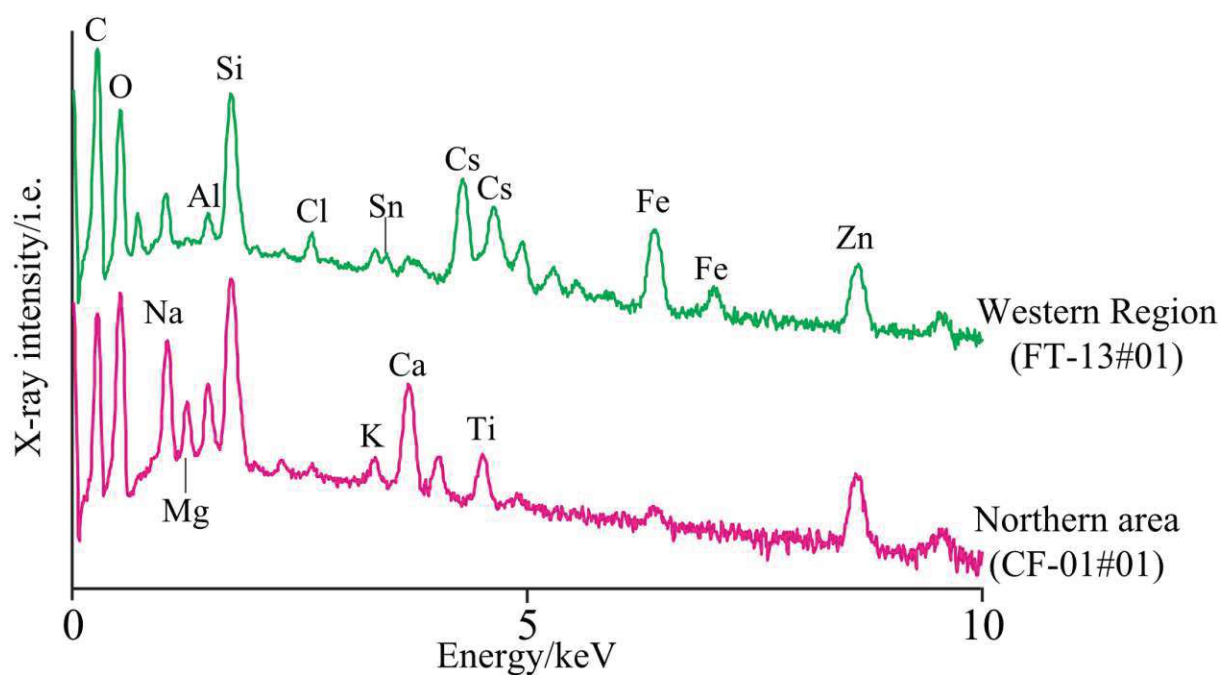


Figure 17: Elemental dispersive X-ray spectra (EDX) of two representative particles in figure 15. Note the absence of Cs peaks in the Type B particles. **Source:** [49]

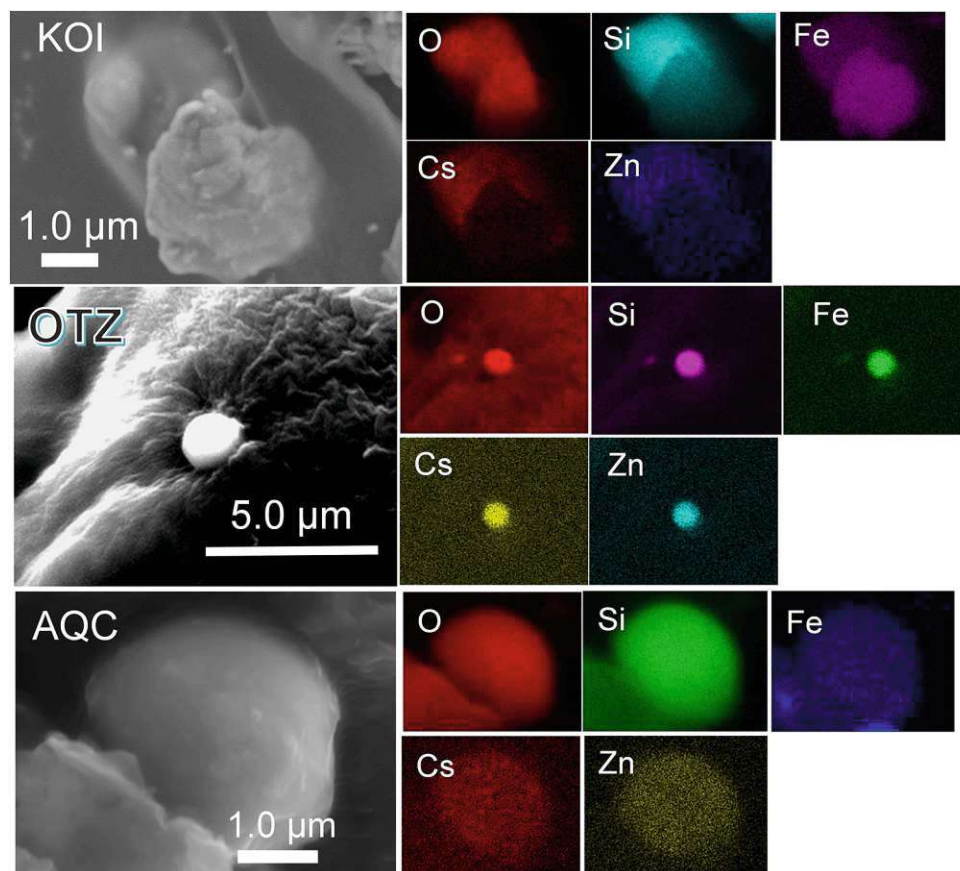


Figure 18: Secondary electron images of three CsMPs: *KOI*, *OTZ*, and *AQC*, associated with the energy dispersive X-ray spectrum (EDX) maps of the major constituents. **Source:** [53]

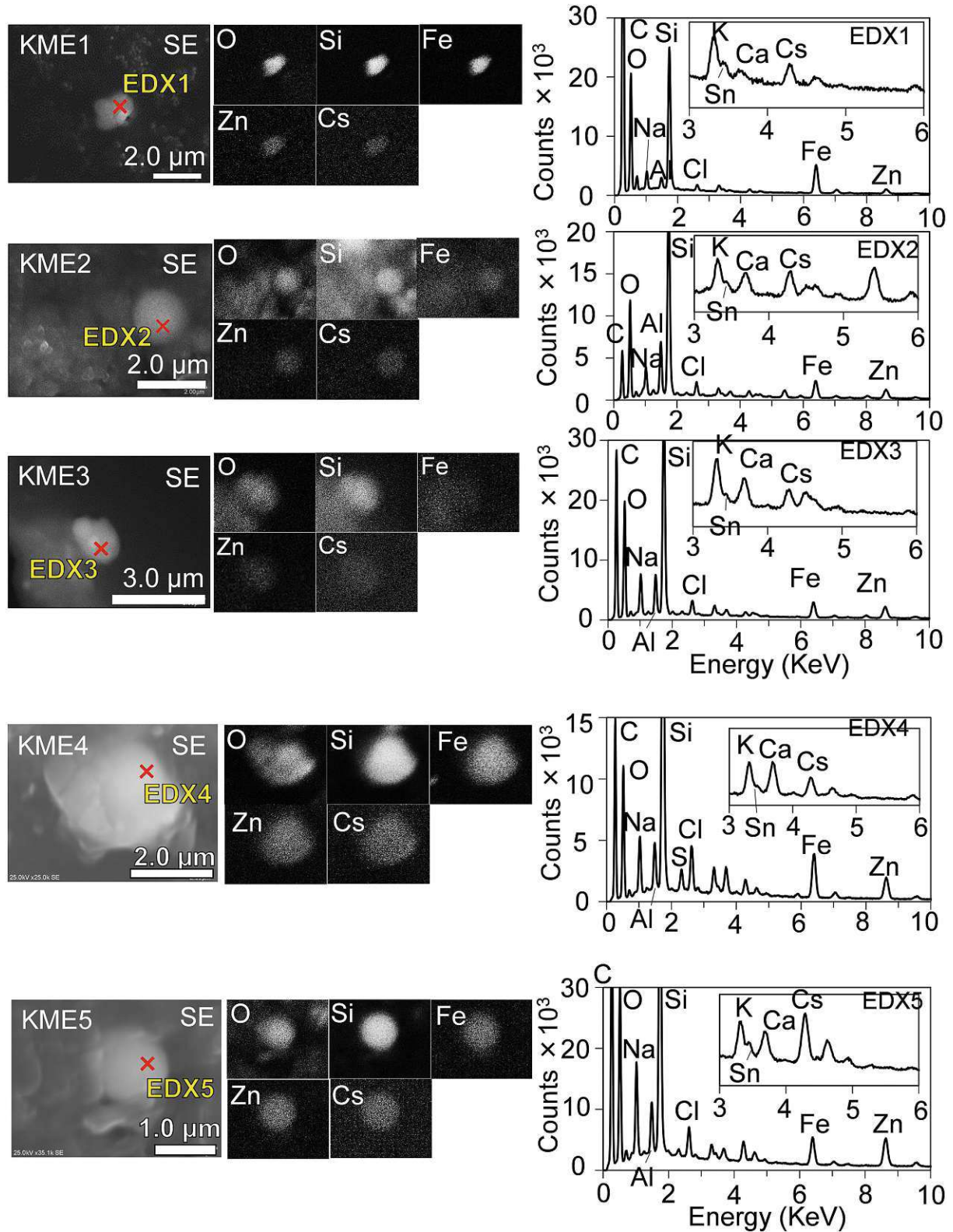


Figure 19: Secondary electron (SE) images of isolated CsMPs labeled *KME1 - 5* with the EDX elemental maps of their major constituents. The EDX spectrum obtained from point analysis is associated for each SE image, of which the position of analysis is indicated by the red cross labeled as *EDX1 - 5* (color references interpretation online). **Source:** [54]

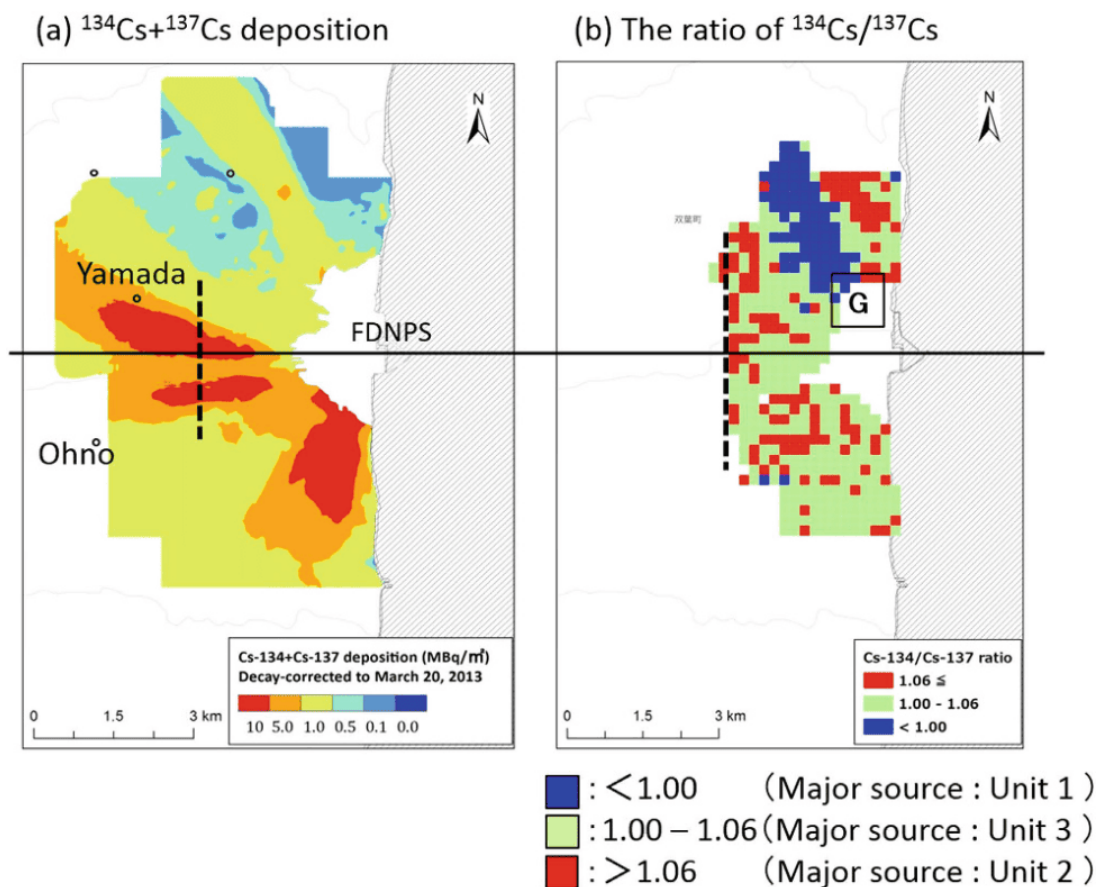


Figure 20: Autonomous unmanned helicopter (AUH) survey; spatial maps of (a) $^{134}\text{Cs}+^{137}\text{Cs}$ deposition over the 5-km area of FDNPP [55], and (b) the $^{134}\text{Cs}/^{137}\text{Cs}$ ratio over the 3-km area. Source: [40]

1.4.2 Cs-134/Cs-137 Ratio

One metric of special importance regarding these particles for the further research of their origins and formation processes are their respective $^{134}\text{Cs}/^{137}\text{Cs}$ ratios. Because the values of $^{134}\text{Cs}/^{137}\text{Cs}$ are different for each reactor due to different fuel burn-up, one can trace back a particle's path to the unit of origin at FDNPP. This is critically important information in the research of the hot particles. Figure 20 shows the deposition of ^{134}Cs and ^{137}Cs on the landscape over a 5-km area surrounding FDNPP. This deposition took place at the time of the two major plumes that are depicted in figure 13a, as well as on March 12, 2011, when the first significant releases of radioactivity were measured. There are a number of very clear plumes on the map, which correspond to the wind directions at the time of the respective releases at the accident site [40]. In table 6, these radiocaesium ratios are stated for the different types of CsMPs, if available.

More interestingly, figure 20 (b) presents the spatial $^{134}\text{Cs}/^{137}\text{Cs}$ ratio over a 3-km area around FDNPP, decay-corrected back to March 15, 2011. The average ratios of the four high-deposition areas in figure 20 (a), i.e., north-northwest, upper-west, lower-west, and south, are 0.95, 1.06, 1.05, and 1.05, respectively. Also denoted in the figure are the typical caesium ratio values for the three different units at FDNPP that can be used to identify the specific reactor of origin. Therefore, the $^{134}\text{Cs}/^{137}\text{Cs}$ ratio for the north-northwestern region is almost identical with that of Unit 1 (0.94 ± 0.01) at the time. However, the other major plumes cannot be easily traced back to one individual unit, because of issues with the accuracy of the survey. It is therefore simply assumed that the areas of the upper-west, lower-west, and south were specifically affected by Units 2 and 3 [40].

Table 7: Cesium concentrations and ratios as measured for the three reactor units at [FDNPP](#). **Source:** The University of Tokyo using undisclosed data

	Ex.	^{134}Cs [Bq/cm ³]	^{137}Cs [Bq/cm ³]	Ratio as of accident
Reactor 1	Hole B	0.695 ± 0.017	0.785 ± 0.019	0.898 ± 0.031
	Sub-drain	5.17 ± 0.080	5.90 ± 0.089	0.890 ± 0.019
Reactor 2	Hole	$(1.99 \times 10^6) \pm (4.6 \times 10^3)$	$(2.00 \times 10^6) \pm (4.9 \times 10^3)$	1.010 ± 0.003
Reactor 3	T/B water	$(1.79 \times 10^5) \pm (6.2 \times 10^2)$	$(1.80 \times 10^5) \pm (6.6 \times 10^2)$	1.005 ± 0.005

The values of the ^{134}Cs and ^{137}Cs concentrations, as well as their respective ratios for all three reactors are shown in table 7 too. These have been measured at different points near the reactors that were accessible at the time.

1.4.3 Assumed Origins

Due to the average $^{134}\text{Cs}/^{137}\text{Cs}$ ratio of 1.04, Type A is considered to originate from Unit 2 or 3. The particles are spherical or non-spherical with a diameter of 0.1 to 50 μm , more than 40% SiO_2 in weight composition, and on top of this contain major amounts of Fe, Zn, and Cs. Because there was no insulation in the Unit 3 RB, this type is considered to have been produced by atomization of the HEPA filters during the Unit 3 hydrogen explosion. Trace amounts of U and ^{90}Sr were also found in Type A particles. The specific activity of this type is 1.09 - 1.08 Bq/mm³ [45].

Type B particles are larger than Type A with an average diameter between 70 and 400 μm . Both the $^{134}\text{Cs}/^{137}\text{Cs}$ ratio (0.94) and specific activity (5.0×10^3 - 5.0×10^5 Bq/mm³) are significantly lower when compared to Type A, especially the latter (around 4 orders of magnitude less). The dispersion area of this type is limited to the north-northwest side of Unit 1 as shown in figure 20. Due to the fact that fiber-like structures have been observed in some of the particle (see figure 21), Type B is thought to have been formed by the atomization of the insulation materials (e.g., rock wool) covering the isolation condenser in the RB of Unit 1 [45].

With a particle diameter of 120 μm , Type C is larger than Type A. Together with the respective $^{134}\text{Cs}/^{137}\text{Cs}$ ratio, Unit 3 is considered to be the place of origin for this type. The particles are believed to have formed due to atomization of the Unit 3 pre-HEPA filter that possessed considerably larger glass fibers (50 μm) than the main HEPA filters (2 μm), where Type A might have formed [45].

The origins of Type D are harder to trace back than for the previous types. Because of the $^{134}\text{Cs}/^{137}\text{Cs}$ ratio, Unit 1 is considered to be the place of formation. However, at this unit, the hydrogen explosion was milder when compared to Unit 3, leaving the HEPA filters largely intact, hindering any atomization or melting. This is also the reason why – as of 2022 – they could not be dismantled yet (high dose rates). The filters fulfilled their function by catching large amounts of radioactive material before the explosion, which largely remained unaffected after the event. One interesting finding was the fact that similar particles to Type D were, in fact, found in the SGTS piping of Unit 1, indicating at least a partial atomization of the filters and reinforcing Unit 1 as the place of origin [45].

The last type, Type E, stands out especially with its low specific activity. Together with its spherical shape and relatively large size in comparison to Type A, the formation process of this type can be explained using the atomization of the Unit 4 HEPA filters. The low specific activity can be explained by Unit 4 not being in operation at the time of the accident as mentioned in

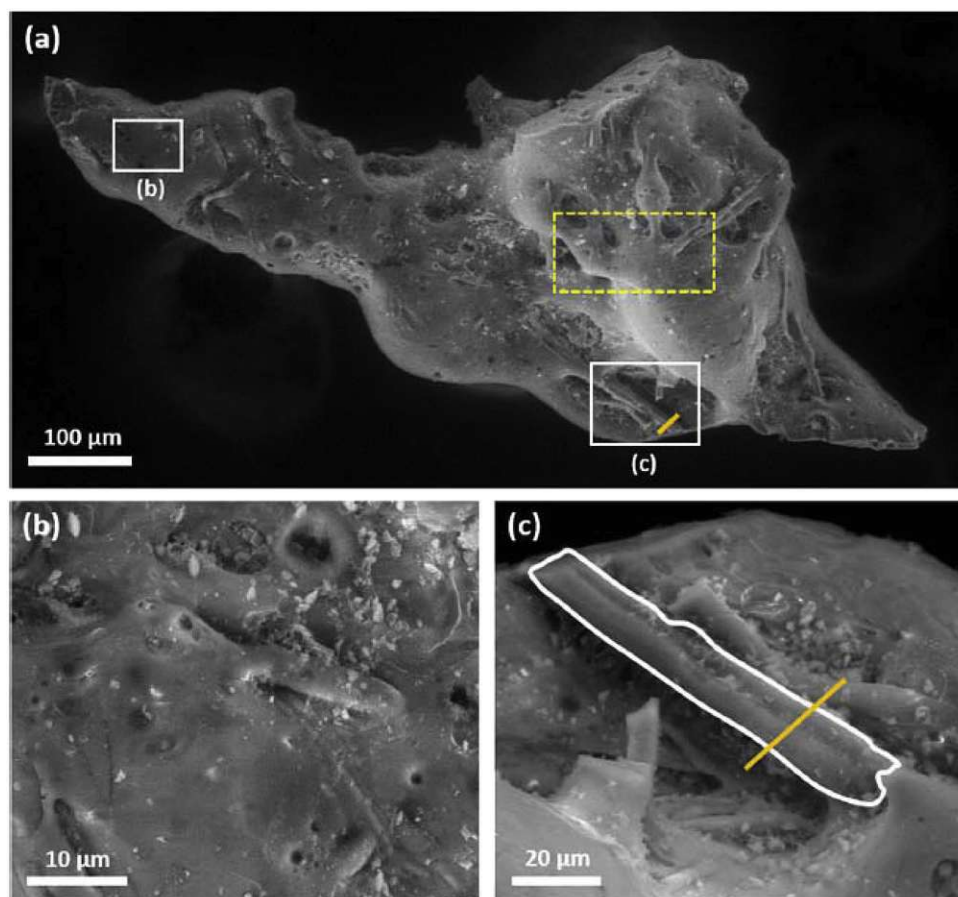


Figure 21: (a) SEM image of a Type-B CsMP; (c) shows a fibrous surface feature. Source: [46], originally reported in [49]

section 1.1, and a slow high-temperature blast would form relatively large and spherical particles [45]. This type is the most recently identified and proposed new type of CsMPs from FDNPP, with the study being published in late 2022 [52].

1.4.4 Formation Mechanism

To understand the formation mechanisms of the CsMPs, it is important to understand what the process of atomization involves, which has been mentioned a number of times so far. In atomization, particles are produced by literally atomizing a liquid in a coherent state by means of a high-speed flow. This is in full contrast to the more standard evaporation/condensation mechanisms in which particles are formed by condensation nuclei, when a material is being heated, vaporizes, and is then cooled back to a liquid. The majority of particles from severe accidents are produced this way [45], just like those at the Chernobyl accident like mentioned in section 1.3.6. The problem with the condensation approach at the FDNPP accident is that during the condensation process, typically many different elements can be found, so a pure Si matrix like the ones found in the present CsMPs would be unlikely to have formed. To further support the atomization hypothesis, the energy source given by the hydrogen explosions would be the only sources capable of melting the glass fibers⁷ and then atomizing the liquid SiO₂ melts [45]. One study was able to reproduce the formation of spherical particles similar to the found CsMPs by heating glass fibers to a temperature of 450 - 800 °C [57].

In a first study, the generation scenario for Type A particles was looked at [59]. It was proposed that some of the glass fibers of the pre-HEPA and HEPA filters of the SGTS were

⁷The melting point of SiO₂ is around 1700 °C or close to 2000 K [56].

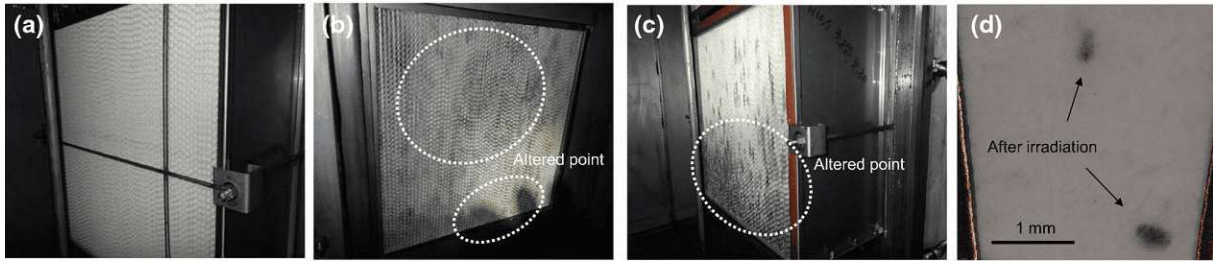


Figure 22: Images of HEPA filters and prefilters. (a) HEPA filter (No.1 in the B system) at the Unit 3 outlet after the accident; (b) Prefilter (in the B system) at the Unit 3 inlet after the accident; (c) HEPA filter (No.3 in the B system) at the Unit 3 inlet after the accident; (d) Magnified HEPA filter after irradiation in a laboratory experiment. **Source:** [57], modified from [58]

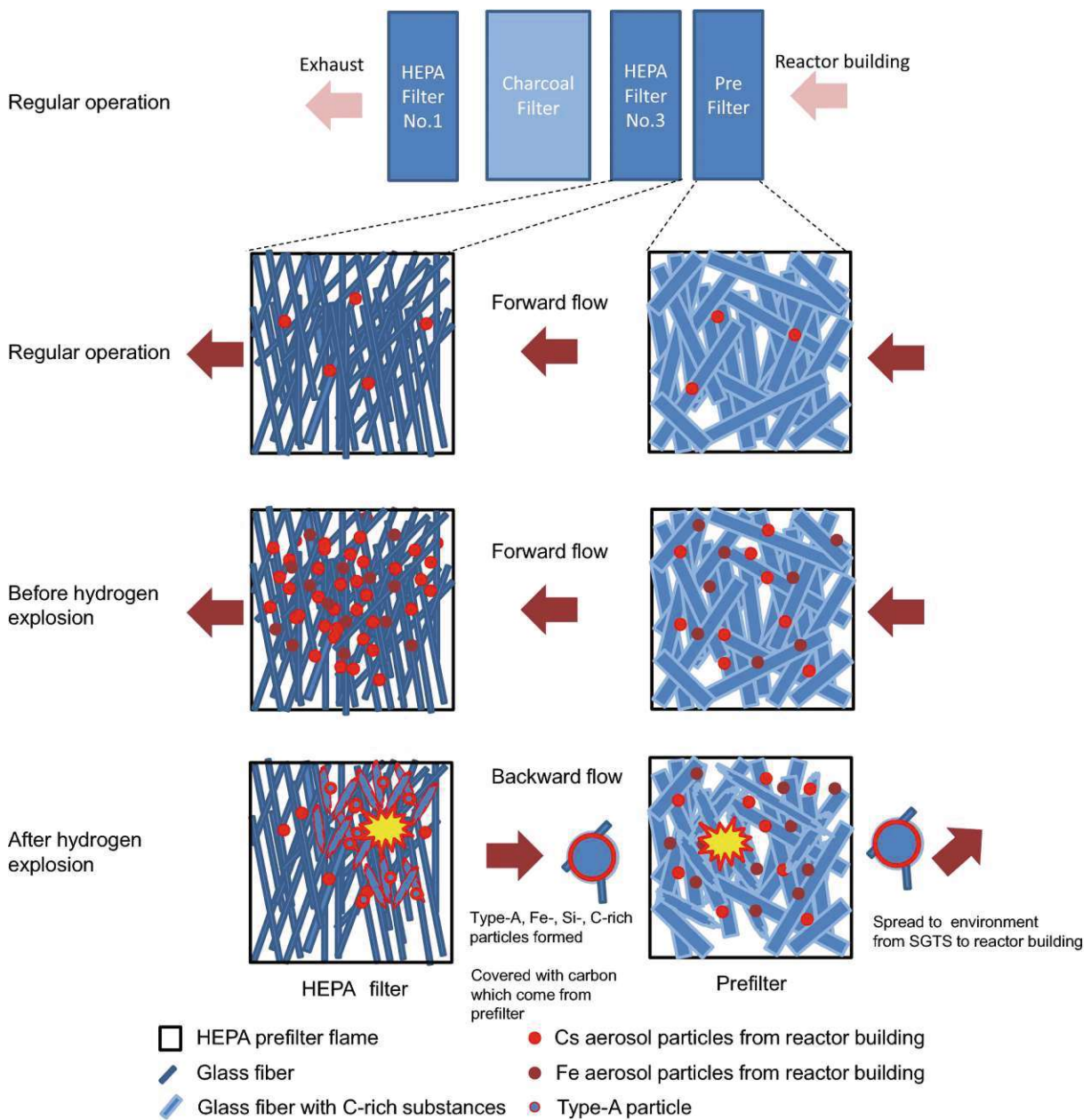


Figure 23: Schematic of the likely Type A particle formation mechanism from the SGTS at FDNPP. **Source:** [57]

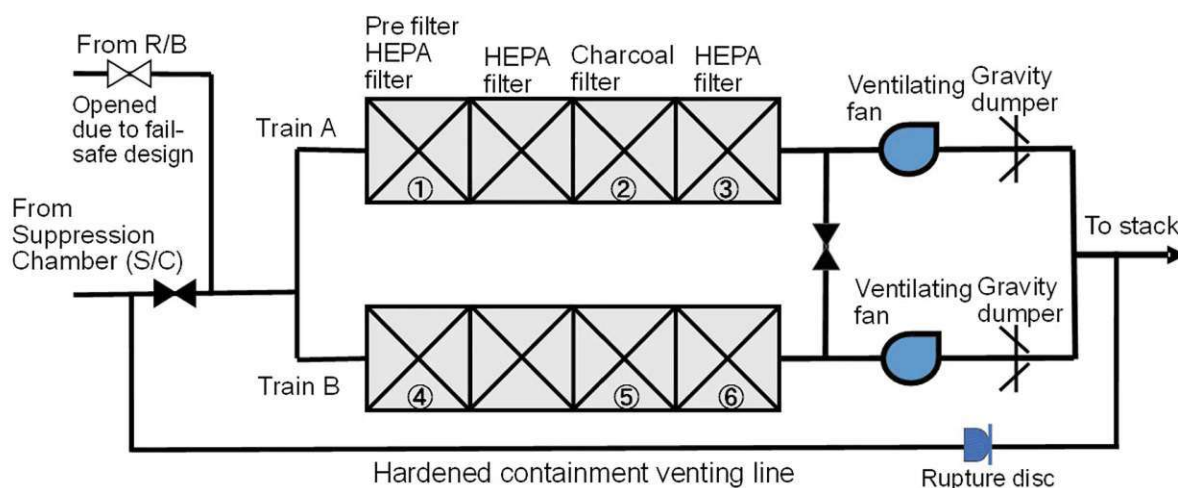


Figure 24: Setup of the HEPA filters in both lines of the SGTS at FDNPP. Source: [45], removed dose rate measurements from figure

melted under the extreme heat of the hydrogen explosion and blown away due to the subsequent high vacuum in Unit 3 of the plant. The melts of the fibers would then form spherical particles due to the surface tension of the liquid. Some of the HEPA filters of Unit 3 were shown to exhibit burn marks due to a high heat flux in a relatively recent report of Japan's NRA (Nuclear Regulation Authority) [58]. This can be seen in figure 22 (b) and (c). Interestingly, most of the HEPA filters of Unit 3 were shown to be largely intact even after the accident, one example of which can be seen in figure 22 (a). Similar burn marks could be produced by irradiating an area of a comparable HEPA filter (glass fibers) using electron beam heating in a study, which can be seen in figure 22 (d) [57]. It was reported that during the electron beam heating, uniform-sized particles were formed in the irradiated area, depending on glass fiber (μm order) thickness. This further indicates and strengthens the assumption that Unit 3 was the place of origin for Type A particles. This is also supported by fibrous structures found in some CsMPs like the one shown in section 1.4.3, figure 21.

In summary, a schematic of the formation mechanism can be seen in figure 23. This entire process essentially comprises of three sub-processes that took place first during normal operation and then in rapid succession during the hydrogen explosion. The sequence is being explained in more detail in the corresponding study [57]:

1. The HEPA filter captured aerosol particles containing radiocaesium and other particles containing Fe derived from RPV during regular operation.
2. After the loss of coolant accident (LOCA) and before the hydrogen explosion, the HEPA filter absorbed more aerosol particles containing radiocaesium and Fe.
3. After the hydrogen explosion, part of the prefilter and HEPA filter was burned, melted, and atomized by heating, and some carbon substances on the prefilter's surface were attached to the HEPA filter. Simultaneously, Type A, Fe-, Si-, and C-rich particles were formed. Finally, these particles spread into the environment from the SGTS to the reactor building due to backward flow blast.

A more recent study suggests a slightly updated version of this formation sequence [45]. For almost an entire day before the hydrogen explosion occurred, the core cooling water in Unit 3 was empty, indicating that the nuclear fuel was molten for around 24 hours, and therefore possibly leaking Cs to the outside of the fuel. Since the RB was intact before the explosion, the SGTS piping and HEPA filters would have trapped a significant amount of this escaping radiocaesium from the fuel as per specification due to their high efficiency of trapping aerosols.

The **SGTS** setup with both **HEPA** filter trains at **FDNPP** is shown in figure 24. This trapped Cs could have been formed by nucleation and might have been in the form of water-soluble aerosols.

It is likely that the hydrogen explosion entered the **SGTS** and at first came into contact with the pre-**HEPA** filter, which was made up of pretty large 50 μm fibers. The fibers near the surface melted and were subsequently atomized during the explosion, forming large-size Type A, i.e., Type C particles, containing some of the deposited water-soluble Cs from the fuel inventory [45].

The explosion then reached the main **HEPA** filter with much finer fibers (1 - 2 μm diameter) that was installed behind the pre-**HEPA** filter. It also melted and atomized the surface layer of these fibers, producing spherical, uniform-sized particles of Type A that were much smaller than those produced by the pre-**HEPA** filter [45].

The flames could then have reached the activated carbon (charcoal) filter installed behind the main **HEPA** filter. This would have burned the activated carbon filter, and the burn-activated carbon adhered to the surface of some Type A particles that were separated from the main **HEPA** filter. This would explain the carbon film adhering to the surface of some Type A particles that were inconsistently observed [45]. The origins of this surface-bound carbon are another interesting research topic, that was look into in another study. It identified possible sources of the carbon in the activated carbon filters, but also in the acrylic resin binder applied to the surface of the glass fibers of the **HEPA** filter [60].

After the melting and atomization of several surface layers of the different filters during the explosion, the resulting blast would have left almost a vacuum at its origin in the **RB**. This meant that a backflow of air would rush into the building from the **SGTS** piping. To restrict this kind of backflow, so-called gravity dampers were installed that would close if the pressure inside the **RB** was lower than outside, therefore preventing air from entering the building. In the time it took the gravity dampers to close, part of the now-produced **CsMPs** could have escaped just in time. These particles would have rapidly cooled because of the absence of any heating source, and with this formed non-spherical particles. On the other hand, the **CsMPs** that were left in the **SGTS** piping after the gravity dampers closed, would have been exposed longer to the heat of the blast due to hot air remaining in the enclosed space and the additional combustion of the charcoal filters. Considering this, the particles had enough time to become spherical in shape due to the surface tension of the molten SiO_2 [45].

After the accident, the **SGTS** filter room was found to contain about 50 L of condensed water, likely formed during the oxyhydrogen reaction which converts oxygen and hydrogen to water vapor. This might also have been the case in other units at **FDNPP**. Due to this water in the **SGTS** pipings and **RBs**, the produced Type A particles could have been quenched and temporarily trapped inside these respective spaces. After the accident, remaining decay heat would have evaporated some of the water, exposing more **CsMPs** that could have easily been resuspended by subsequent ventilation or steam generation. This process would explain why multiple releases of Type A took place over the course of the following days [45]. In figure 25, the entire process of Type A formation and distribution into the environment according to this hypothesis is shown.

There have not been a lot of significant studies discussing the formation mechanisms of most of the other types of **CsMPs** found at **FDNPP**, possibly due to the sheer complexity making it difficult to repeat findings. Most of the recent papers investigated the formation of Type A and very similarly sized, as well as spherical particles, so more research is needed in that regard. However, it can be assumed that similar processes took place, especially for other spherical particle types.

1.4.5 Current State of Research

Lately, literature in the last few years has been more focused on the replication of the formation of some synthetic **CsMPs** to research the formation mechanisms of Type A. This includes the testing of different candidate materials in high temperature steam atmospheres [61] and conducting experimental **molten core concrete interactions (MCCI)** as a potential generation mechanism

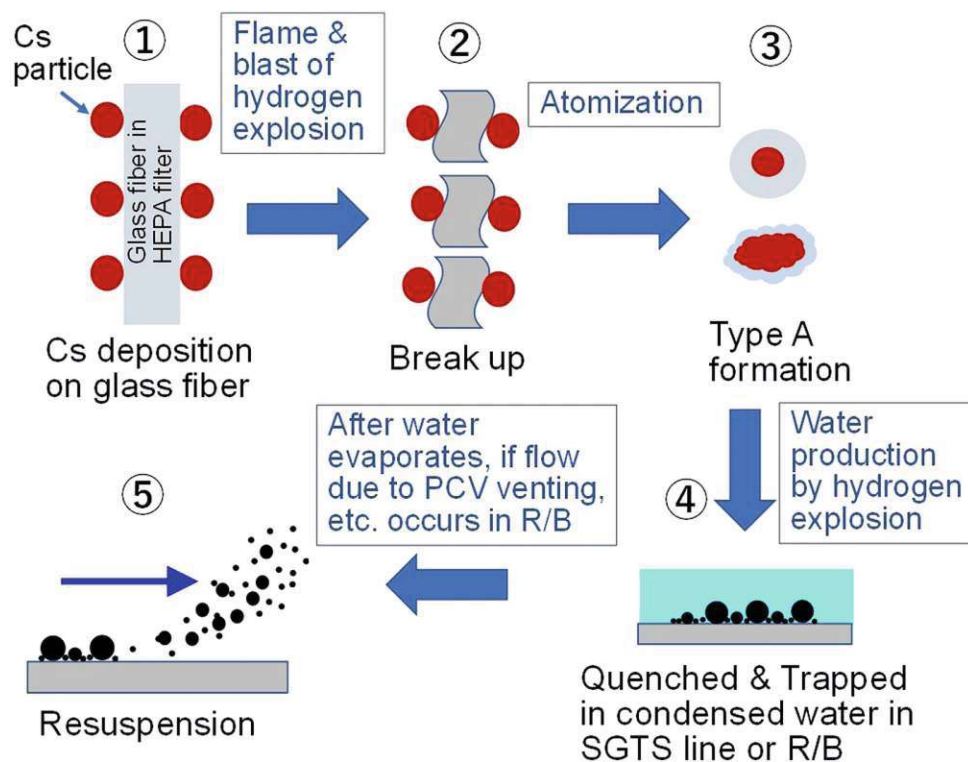


Figure 25: Summary of the process from Type A formation to the environmental release derived from a recently proposed hypothesis. **Source:** [45]

[62]. The findings of the latter study demonstrate that MCCI is in capacity to produce spherical sub-micronic and micronic particles, primarily composed of amorphous silica and incorporating elements akin to CsMPs. Additionally, a humid atmosphere was found to be beneficial to this process, which could have been the case in the RB and SGTS after the hydrogen explosion.

One study looked at radiocaesium-bearing microparticles with different morphologies in soil samples in areas surrounding FDNPP [63]. It concluded that Type A particles could have had similar formation mechanisms at multiple different locations, despite the varying plume directions. Compared to spherical particles, non-spherical particles also exhibited higher elemental distributions of C, Zn, and Cs.

Another study looked at the availability and distribution of CsMPs in a locked-down school building only about 3 km southwest of FDNPP. They specifically looked into the distribution of particles depending on the floor of the building and the position in regards to staircases and exits. On top of this, the fraction of radiocaesium particles per gram in dust was determined as well as the radioactive fraction of these microparticles [54].

2 Materials and Methods

This section will introduce the two different types of samples that were investigated in this work, as well as all the used experimental setups, equipment, and the analysis processes used to examine them. In the end, the goal was to find, extract, and examine one or even multiple CsMPs from the provided samples, which required a number of different analytical methods at the facility of the ATI and help from the University Service Facility for Transmission Electron Microscopy (USTEM) at TU Wien.

2.1 Samples

For this thesis, two different types of samples were provided for further analysis: one is a passive air sampler deliberately designed to capture aerosols like radioactive contamination, e.g., CsMPs, the other was a large piece of a standard fleece coat from inside an abandoned building in the difficult-to-return zone. Both types were located in areas surrounding the Fukushima Daiichi Nuclear Power Plant (FDNPP) for different amounts of time. Both sample types were subsequently contaminated with dust and other radioactive aerosols from the accident's fallout and resuspension of material during the exposure and therefore contained a measurable quantity of ^{137}Cs and in some cases ^{134}Cs as well.

2.1.1 Namie Fleece Coat



(a) Symbolic illustration of the sample extraction on a similar-looking fleece jacket.

(b) Location of the residential building inside Omaru district, Namie-town, Fukushima Prefecture.

Figure 26: Symbolic image of the extracted sample from the fleece jacket with the position of the extraction point relative to FDNPP.

The so-called *Namie fleece coat* is the primary sample researched in this thesis. It is a piece of the right sleeve of a larger fleece coat hung inside a residential building in Omaru, Namie-town, Fukushima Prefecture, i.e., inside the evacuation/difficult-to-return zone. A symbolic image of a similar looking fleece jacket with the sample location is shown in figure 26a. The location in relation to FDNPP can be seen in figure 26b. The latitude and longitude of the sampling point was N37.460428, E140.899531. The distance to the power plant from that location is about 12.5 km. The fleece coat was hung on a hanger in a room inside the house that was locked down from the day of the accident (March 11, 2011) with all the doors and windows remaining shut. It was collected by residents on April 17, 2015, almost exactly four years after the accident. In the meantime, no one had entered the locked house, so the sample hung there completely untouched.

The weight of the entire fleece coat was 668 g upon collection in 2015. As of June 19 of the same year, the specific activity of the fleece was as follows:

- $1230 \pm 15.1 \text{ Bq/kg } ^{134}\text{Cs}$
- $4964 \pm 43.2 \text{ Bq/kg } ^{137}\text{Cs}$

The $^{134}\text{Cs}/^{137}\text{Cs}$ ratio can be calculated from these values by converting the activity back to the activity on March 11, 2011. This results in a $^{134}\text{Cs}/^{137}\text{Cs}$ ratio of 0.94 ± 0.01 , which clearly corresponds to the ratio of Unit 1 at the time of the accident. Due to this, it is very likely that the source of contamination at the collection point was, in fact, Unit 1.



(a) *Top* side of the fleece coat sample.

(b) *Bottom* side of the fleece coat sample.

Figure 27: Photos of the *top* and *bottom* sides of the Namie fleece coat sample on an autoradiography plate. The missing corner in these photos was cut at a prior point and was used for further analysis.

Part of the fleece coat's right sleeve was cut with scissors and then sent to the [ATI](#) by Katsumi Shozugawa for further investigation. This now is the sample that is being investigated in this work. In figure 27, the *top* and *bottom* sides of the cut fleece coat sample are shown. The piece of cloth only weighs around 16.5 g, roughly 2.5% of the original mass of the coat.

2.1.1.2 Passive Air Samplers

The passive air samplers are based on a need to monitor environmental radioactivity, in order to be able to react quickly to nuclear accidents or similar releases of radionuclides. In this specific case, the samplers offer a cost-effective solution for radiation monitoring, even in the most remote places due to their energy independency. Additionally, by using the natural radioisotope ^7Be as a reference, it is also possible to calculate back the amount of air that had been sampled. Therefore, the samplers, in theory, could not only provide a measure for the absolute radioactivity in a given time frame, but also the specific radioactivity per unit volume. ^7Be is generated naturally in the atmosphere and the average concentrations per cubic meter of air are very well known.

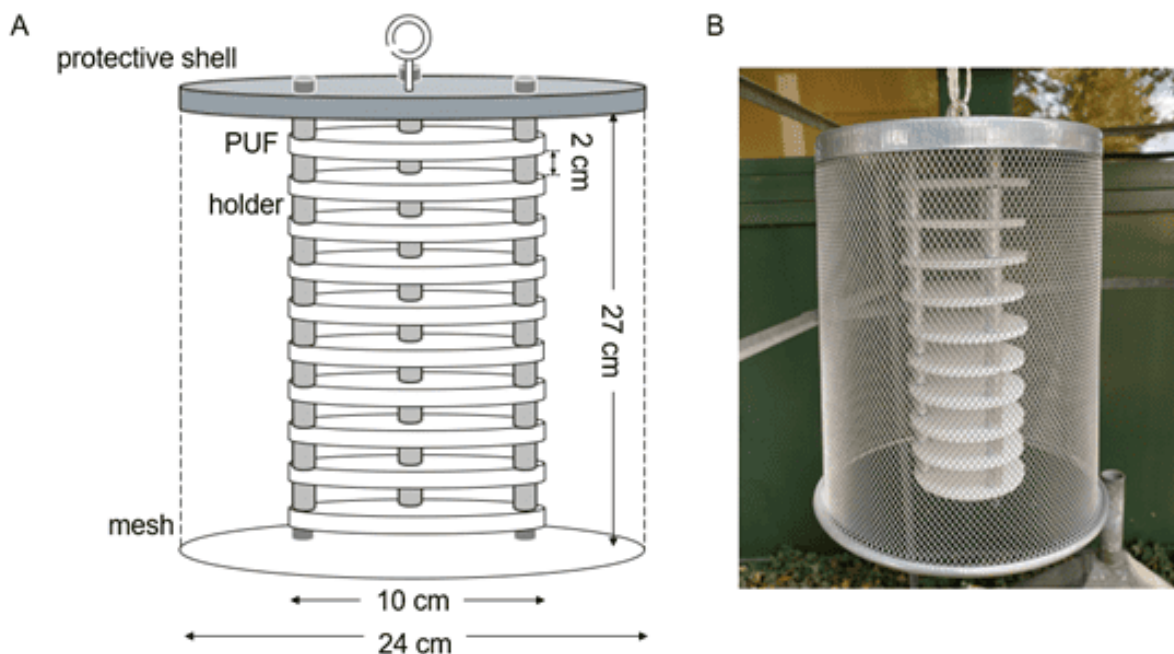


Figure 28: The setup for a passive air sampler using multiple polyurethane foam (PUF) disks with defined spaces and housed in a large cylindrical wire mesh. **A** Schematic with the relative dimensions of all the individual parts of the unit. **B** Photo of an assembled unit ready for particle collection. **Source:** Bin Feng, Fudan University

The passive samplers were designed by Bin Feng to ideally capture and trap coarse particles ($>1\ \mu\text{m}$) from the ambient air using the combined effects of diffusion, gravity settling, and turbulent inertial forces. The schematic and a photo of the assembled setup are shown in figure 28. Each unit is made up of 10 cylindrical PUF disks that are positioned on top of each other with a space of 2 cm in between for air flow. This increases the active area that is available for particle capture. The column of PUF disks is then mounted inside a larger wire mesh cylinder with top and bottom lids. This helps to keep animals out of the inside, and to protect from precipitation, but also modifies the air flow in a specific way. There are several circular holes in the bottom lid to reduce the influence of turbulence inside the sampler. The outside air can then travel through the wire mesh and the bottom openings. During stable conditions inside the sampler, i.e., little turbulence, in theory, this should block fine particles ($<1\ \mu\text{m}$) from entering, but pass coarse ones due to their larger inertia.



(a) Passive sampler disks A, B, and C.

(b) Passive sampler disks D, E, and G.

(c) Passive sampler disks H, I, and J.

Figure 29: Photos of all nine provided passive sampler disks on autoradiography plates that have been investigated for this thesis.

For the research reported here, nine sampler disks labeled A - J (excluding F) that have been



Figure 30: Photo of the sampling location amongst the forest vegetation with the passive sampler set up around 1 km from the Unit 1 RB at FDNPP for a good 3 months. **Source:** Katsumi Shozugawa, University of Tokyo

exposed to resuspended radioactive aerosols of the FDNPP fallout were provided. The three groups of three disks are shown in figure 29. They have been recovered from a passive sampler set up in a forest at the coordinates N37.412312, E141.025941, which is only about 1 km from the Unit 1 RB. A photo from the sampling location amongst the thick forest vegetation is shown in figure 30, as well as the fact that PUF disks A - J were mounted from the top to bottom in this case. The unit was placed there on July 14, 2022 and was left to sample the ambient air until October 24, 2022, i.e., for a period of a good three months. Notably, the air dose rate at the sampler location was measured to be around 19 $\mu\text{Sv/h}$.

After picking up the sampler at the end of the measurement period, all of the individual PUF disks have been weighed and examined for the two common radiocaesium isotopes using a gamma spectrometer. The results of the preliminary gamma spectrometric measurement are shown in table 8. Notably, no radioactivity of ^{134}Cs could be registered for any of the disks, though, there were two disks that did have measurable levels of ^{137}Cs .

2.2 Experimental Details

In this section, I will discuss all of the experimental details necessary for the analysis of the samples that were introduced in the previous section 2.1. Most importantly, this includes all of the utilized equipment and the main experimental procedures that were practiced in order to identify, find, and extract potential hot particle candidates. Each point will be shortly described and the necessary motivation behind the use will be explained.

2.2.1 Experimental Equipment

Firstly, to identify the radioisotopes contained in the samples and their respective activity, ultra-low-level gamma spectrometry at the low-level counting facility in the basement of the ATI was used. This consists of a 226 cm^3 HPGe detector connected to a PC-based multi-channel analyzer with preloaded filter. The detector was manufactured by Canberra™ (detector model GC5020)

Table 8: Analysis results for the 10 PUF disks after their pickup, including the weight, the ^{134}Cs and ^{137}Cs activities, and the detection limits (3h gamma spectrometry) following a good three months period of sampling. **Source:** Katsumi Shozugawa, University of Tokyo

PUF Disk	Weight [g]	^{134}Cs Radioactivity [Bq/kg]	^{134}Cs Det. Limit [Bq/kg]	^{137}Cs Radioactivity [Bq/kg]	^{137}Cs Det. Limit [Bq/kg]
J	1.28	ND	187.0	ND	201.7
I	1.28	ND	184.5	$>2\sigma$	160.9
H	1.27	ND	192.1	$>2\sigma$	168.9
G	1.29	ND	203.3	ND	189.3
F	1.27	ND	194.5	ND	210.5
E	1.29	ND	181.1	ND	149.2
D	1.29	ND	205.4	ND	175.8
C	1.26	ND	212.6	ND	213.3
B	1.27	ND	205.4	ND	172.2
A	1.27	ND	207.5	ND	179.3

and it features 2.0 keV energy resolution at the specified 1332 keV ^{60}Co peak with a 52.8% relative efficiency. In addition to this, the detector system is surrounded by a solid-cast virgin lead shielding with steel casings (ORTEC™ HBLBS1 shielding, total weight of 1134 kg). This makes it the best HPGe setup at the ATI in terms of the lower detection limit for most common radioisotopes, especially those expected in the samples here. Software readout was done using the supplied Genie™ 2000 program. A photo of the setup is shown in figure 31a. Clearly visible is the lead shielding with the steel casing and a surrounding additional layer of lead bricks forming a second layer of lead around the detector. Inside the main shielding, copper can be seen shining through at the top, which is part of the Z layering to increase shielding efficiency. The cylindrical detector is at the center of this large lead castle. Below it is a Dewar filled with liquid nitrogen which is used to cool the detector.

At the beginning, this setup was used to gauge the activity of the samples in their entirety and then some pieces of the fractionated samples. However, since this was relatively inefficient due to the very low activity of the samples, it was later on almost exclusively used to determine the activity of ^{137}Cs and, if possible, ^{134}Cs as well. This will be discussed in more detail in the upcoming sections. The measurement duration for most samples typically was a couple of days, in some rare cases – especially at the beginning – just a few hours would also be good enough for a clear spectrum. Samples were just placed directly on top of the detector window with only some minor plastic wrapping separating them.

Autoradiographic imaging plates (AIPs) were used extensively in this work due to their overall simplicity, the ability to profit off of parallelization, and last but not least their spatial resolution. For this purpose, a number of image plates of different types and with different sizes were used. This includes the following two types and their respective specifications, with each being available in a variety of sizes⁸ manufactured by DÜRR NDT [64, 65]:

- High sensitivity – GCR image plate (100 μm SR_b, white active surface), labeled GP...
- Normal resolution – HCR image plate (63 μm SR_b, white active surface), labeled HR...

Additionally, an image plate by the Packard Instruments Company (now Perkin Elmer) with a size of 12.5×19.2 cm was used extensively, especially for the exposure of the Namie cloth

⁸Typical sizes available at the ATI were 10×24 cm, 18×24 cm, and 24×30 cm in varying quantity.



(a) Photo of the low-level gamma spectrometry setup used extensively at the ATI for this thesis. The top shielding consists of the original factory shielding for this setup with an additional layer of lead bricks around that. The nitrogen dewar sits below the detector platform.



(b) Photo of the Scios 2 DualBeam FIB SEM setup used at the USTEM to do micro-surgery on the samples to extract potential hot particle candidates.

Figure 31: Photos of the low-level gamma spectrometry setup at the ATI and the Scios 2 DualBeam FIB SEM at the USTEM. Both used extensively in the course of this thesis.

samples (Type *SR*, *Super Resolution Phosphor Screens*, *Small*[66]). This plate originated from a different commercial line of digitized phosphor imaging equipment, but works essentially the same as the others. Unfortunately, not much specific information on this type of plate could be found, except for the statement that "SR (Super Resolution) storage phosphor screens are made from the finest grain phosphor crystals for highest resolution" [66].

The *autoradiographic imaging plates (AIPs)* are designed specifically for their use in computed radiography, which is a compromise between the old-fashioned film and the modern fully digital autoradiography. They are passive devices, meaning they do not require any power and cannot be read out live. However, when it comes to evaluating the results, it is as easy as scanning the image plates with a special scanner to get the digital data – no chemicals required, in contrast to old-fashioned film. A representative selection of image plates and their packaging with detailed model numbers is shown in figure 32.

The scanner that was used to evaluate all of the image plates at the ATI is the HD-CR



(a) Packaging of the Packard Inst. Co. AIP. (b) The Packard Inst. Co. AIP itself.

(c) Packaging of a representative DÜRR NDT AIP.

Figure 32: Small, representative selection of [autoradiographic imaging plates \(AIPs\)](#) from the two main manufacturers that were used in this thesis.

35 NDT by DÜRR NDT. This scanner is able to analyze image plates of a variety of different sizes and does not require a dark room. It works by reading out the latent image of the plate by shooting a finely focused laser beam at each *pixel*. The stimulated image plate pixel then emits blue light with an intensity that is proportional to the amount of incident radioactivity during exposure. This process is very similar to that used in optically stimulated luminescent dosimeters. The laser spot size for this device can be as small as $12.5\ \mu\text{m}$. All exposed image plates were evaluated using the *Sensitive 25 μm Blue IP – Binning* mode that, depending on the size, takes around 10 - 15 minutes on average to finish a scan and delivers the best results.

Before every new image plate exposure to the samples, all old data from previous or background exposures was erased using the *Erase Extra* command of the scanner. This pulled the image plate through the device once, while clearing all the pixels, making sure no data remains on it. In normal use, the plates that are scanned should be immediately re-usable, however, this extra step was done out of caution for ghosting or other artifacts.

In most cases, the image plates were put down straight on a tray with the active (white) side up, then the samples were positioned on top of this active side, so that it is later on comprehensible which exposed spots corresponded to what sample. Most of the time, the samples themselves were wrapped in a single layer of very thin plastic wrap in order to absorb as little radiation as possible for the best possible signal-to-noise ratio and the shortest necessary exposure time. It was also possible to wrap the AIP itself to prevent any contamination from the samples to the sensitive device, however, most of the time it was a lot more feasible to just individually wrap and label the samples themselves. That way, they would not get lost as easily and any accidental loss of hot particles from the samples themselves was minimized. The exposure time varied between the samples, but typically a day or two was well enough for the Namie flece samples and a couple of weeks or even months were necessary for the passive samplers in general. More on this will be reported in the later sections as well.

Readout and analysis of the data was done using the *D-Tect* software that is supplied by DÜRR NDT with the scanning device. The software was directly connected to the scanner and provided all the controls to select the necessary modes, start and stop the processing, as well as receiving the data from the image plate. Once a scan is finished, the entire image plate exposure is revealed in the program and the image can be adjusted and slightly modified depending on the needs. For the qualitative analysis of the existence of hot particles in a certain sample, this is

often enough. For further processing, *OptiQuant* was used, which is a similar, more feature-rich software to manipulate images developed by the former Packard Instruments Company.

To search for fairly large hot particles and to identify regions of interest in the samples, two standard light-optical microscopes at the [ATI](#) could be used. There was both a transmitted light microscope and a reflected light microscope in order to examine the samples for any abnormalities, for what could be large-scale hot particles.

Finally, to identify and extract small potential hot particles from the prepared samples at the [USTEM](#), initially two devices were used: The FEI Quanta 200 FEG [SEM](#) and the Scios 2 DualBeam [FIB SEM](#). The Quanta 200 is a standard [SEM](#) with the ability to detect both the emission of secondary electrons and backscattered electrons for imaging. In addition to this, the device is also able to perform X-ray microanalysis, which is of special importance for the determination of the atomic composition of the samples. Due to several limitations, this device has only been used once, though, namely at the very first analysis session at [USTEM](#). For the remainder of the analysis sessions, the [FIB SEM](#) had been used, an image of which is shown in figure [31b](#). This device can perform all of the tasks that the other [SEM](#) can do, only significantly better and more efficiently. In particular, the [FIB SEM](#) adds the ability to perform micro-surgery using the focused ion beam to extract potential hot particles from the larger sample matrix. This is done by inserting a fine needle with a tip size of around 5 - 10 μm and fusing the particle onto it using both the ion beam and a special gas mixture that is inserted into the chamber right on top of the sample location. The sole particle is then transferred onto a sample holder, where the process is repeated, fusing it to its new location. The ion beam can also be used to cut away material if needed. More on this will be discussed in section [2.2.2](#) and in the results.

In order to prevent charge buildup on the samples, due to the electron bombardment from the [SEMs](#), they were sputtered with an 8 nm thick layer of a 60/40 Au/Pd mixture before analysis⁹. This step was performed using a Quorum Q150T S fully automatic sputter coater (30 s, 30 mA setting). This mixture has been selected due to the expected absence of gold and palladium from the samples, as to not interfere with the subsequent [EDX](#) analysis.

2.2.2 Experimental Procedure

The following process was identical for all of the different samples, mostly only the measurement and exposure durations differed, depending on the amount of contamination in them. For this reason, it is hereby described only once and any specifics on the procedure relevant to the results presented in the next section [3](#) will be mentioned then. This section only stands to describe the general workflow and motivation behind the steps.

Before any work on finding and extracting hot particles can begin, it is – of course – crucial to identify and quantitatively determine the contained radioisotopes using a gamma spectrometer. This first step is important to gauge if any usable quantity of radioactivity is present and, especially in this case, if radiocaesium can be detected. In all of the samples, **only** radiocaesium and no other nuclides were found, which simplifies the search since any activity found will **always** correspond to the radiocaesium (more on this in section [3](#)). If this were not the case, subsequent measurement using autoradiographic imaging would always have a risk of potential false positives. On top of this, if the detected activity of the radiocaesium was very low to begin with, there is a risk of not being able to detect anything after just a few steps of the following process.

After this initial step, all of the samples that exhibit a reasonable activity of radiocaesium are used in the next analysis cycle. An overview of this procedure is shown in figure [33](#). In general, fractionation has been chosen as the tool of choice for this project since it has been proven to work well in studies (e.g., [\[46\]](#)) and it provides a simple workflow that can be repeated until a satisfactory result has been achieved. Despite being quite time-consuming, due to all

⁹Palladium was added to the gold mixture to prevent lump formation on the sample.

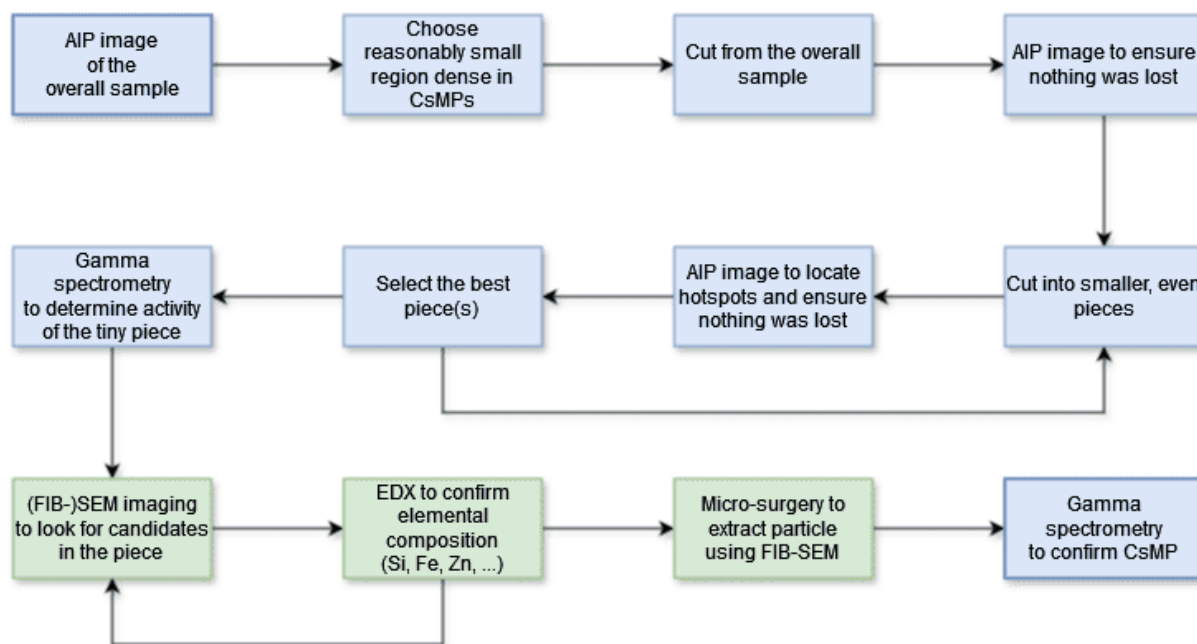
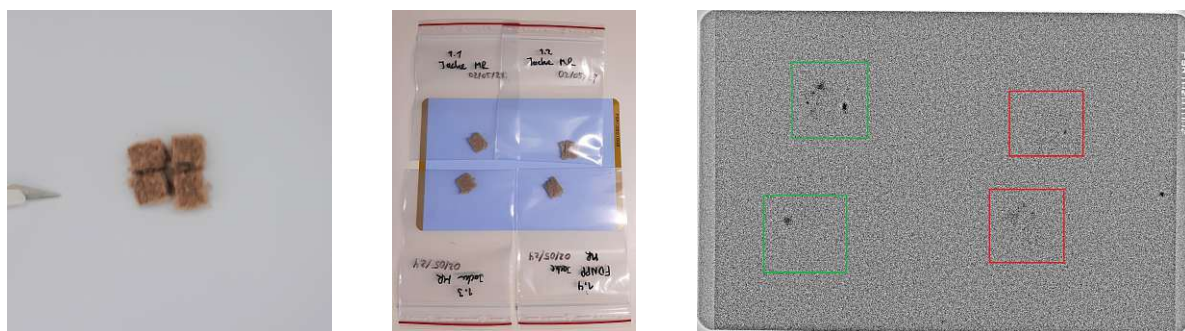


Figure 33: Schematic of the experimental procedure to find and extract CsMPs from a larger sample. Colored blue are all the steps that are performed in-house at the ATI, green are steps that had to be done at the USTEM. The looped parts are repeated until a satisfactory results is achieved or the sample is depleted.

of the involved autoradiographic imaging and gamma spectrometry, it is reliable and has very high chances of success in isolating particles from the rest of the sample matrix as mentioned previously.

The very first step in this chain is to produce an image of the sample using an AIP. This serves as a good overview of regions of interest and hotspots on the sample that might be worth investigating further. Ideally, this is a region dense in CsMPs, i.e., with many bright hotspots that are visible on the exposure. A best case scenario would be a single, very bright point on the edge of the sample. That way it is easy to cut from the rest of the larger sample and only requires little exposure time on the AIP. Next, the identified region of interest is cut from the bulk sample using a clean uncontaminated scalpel on a surface that is itself clean of any other radioisotopes that could easily interfere with the subsequent analysis. This step is done with great care as to not disturb the sample too much, since this could already lead to a loss of some particles that might fall off or get stuck on the scalpel or work surface. For this reason, it is also important to not cut exactly on top of the previously identified hotspots. The area should be large enough to fully contain the desired area of interest without too much excess. During this step, it might already be beneficial to look at the surface of the sample with an optical microscope for any visible particles. It is possible that larger particles containing CsMPs or even a large-scale CsMP itself could be already visible. In order to not contaminate the sensitive AIP, wrapping the sample in a thin layer of plastic wrap is required. Thicker material also works, however, it can quickly increase the exposure time needed for the same result.

After this, the cut sample that is freed from the bulk fiber matrix is then put onto an AIP for imaging, as to ensure that nothing was lost in the process, the hotspot did not move, and the expected arrangement of the hotspot(s) remains in relation to each other and to the edges of the sample. The samples are simply placed on top of the active (white) surface of the AIP and then a heavy object is carefully placed on top of it as a weight, e.g., a stack of paper. This is done to firmly press all of the samples close to the AIP surface for an even exposure and close contact ($1/r^2$ rule). On top of this, the paper protects the AIP from (UV) light that will interfere with the plate at long exposures. The whole assembly is then put away safely in a cabinet to not be



(a) Small piece of the Namie cloth sample with significant hotspots that has been quartered for further analysis.

(b) Individually wrapped and labeled pieces of the cloth on the AIP.

(c) Results of the exposed AIP. The green samples would stay in the isolation procedure, red samples would be rejected (for the time being).

Figure 34: Example of the three-step process that would repeat until the hotspot of interest has been isolated into as small of a piece as possible: (a) cutting the sample into even pieces; (b) producing an AIP image of the pieces; (c) selecting the most promising piece(s) for further processing.

touched or moved until it is done. Note must be taken on which side is currently being exposed since the self-absorption in the sample can greatly affect the results, even shielding hot particles from the other side. If necessary, both sides must be examined using an AIP exposure each.

After these initial four steps in figure 33, the next three steps will be repeated for as long as necessary. First, the sample is cut into even pieces – most of the time this will be cutting into halves or quartering for faster processing. This, again, absolutely requires a clean work surface and an uncontaminated scalpel to not introduce foreign radioisotopes. These cut samples are then individually wrapped in plastic wrap and labeled accordingly. In this case, the samples were simply numbered hierarchically, i.e., sample 1 will be cut into the sub-samples 1.1, 1.2, 1.3, and 1.4. Sample 1.1, for example, might then be cut again into smaller pieces labeled 1.1.1, 1.1.2, 1.1.3, and 1.1.4. This is repeated until the number becomes too long to handle, in which case the prefix is going to be relabeled from a number to a letter, e.g., 1.1.1.1.1.2 becomes A.2. All of the cut samples are then put onto a clean AIP for exposure and stowed away. After this, the AIP exposure is examined and the positions, as well as the intensities of the hotspots are viewed and compared to the previous AIP exposure. If done correctly, the activity should not have changed substantially, i.e., for the same exposure time, the brightness of the hotspots should be the same. If this is not the case, then it is easy to determine if whole particles have been lost by vanishing hotspots or if new foreign contamination has been introduced. Then the most promising hotspots are determined and their respective samples will be cut into pieces again and the whole process repeats as typical for fractionation. Hotspots that are too blurry or indistinct are rejected, as well as samples that exhibit no obvious hotspots. Typically, these are not worth the time and effort it takes for the whole process to conclude, especially since these are mostly too inactive to register on the gamma spectrometer anyways, therefore making it impossible to tell if and how much radiocaesium is contained. In that case, it is easier to search for a whole new area of interest that is more promising. Notes must be taken on which side is being exposed and most of the time, it is highly recommended to repeat the process for the opposite side, especially in the first few iterations when samples are still quite bulky.

A practical example for this three-step process is shown in figure 34. Figure 34a shows a sample of the Namie fleece cloth being quartered using a scalpel. These four pieces are then individually packaged in some type of thin plastic and put on an AIP for exposure, as shown in figure 34b. In this case, they were not wrapped in thin plastic wrap, but instead plastic bags were used. This already prolonged the exposure time quite significantly, so it was switched for subsequent measurements, except if there was an indication to do otherwise. A stack of paper

is placed on top of the AIP with the samples and the whole assembly is stowed away during exposure. In this case it took two days until the AIP was evaluated, the result of which can be seen in figure 34c. The black spots on the image are the regions where the plate was exposed to radiation. If they would have been over-exposed, there would be an additional bright white ring around them, which decreases the spatial resolution. For the selection process, only the best hotspots are being used for the next iteration. In this case, the two samples on the left (highlighted green) are quite promising, while the ones on the right (highlighted red) have almost no visible spots and are quite indistinct in nature. They get rejected from the process if an AIP exposure of the opposite surface results in a similar image, i.e., no reasonable hot particles are contained in these cloth samples.

Additionally, before cutting the samples again, it might be beneficial to view them under an optical microscope as a quick first assessment. Sometimes particles can be uncovered when cutting too close to the edges or especially when cutting smaller samples that already lost most of their volume. These could then be extracted using a very fine needle such as a cannula and investigated with the gamma spectrometer. Very large CsMPs include Type B, C, and D particles, which all feature average diameters in the hundreds of micrometers as shown in section 1.4.1.

Some studies also replaced the AIP step in this repeating process with gamma spectrometry (e.g., [46]). However, this practice was quite inefficient for the samples handled in this thesis for a couple of reasons. The only real benefits of this procedure seem to be that it is easier to do than AIP exposures, at every point of the process it is known exactly what isotopes and how much activity is in the samples, and the effect of self-absorption in the sample can be neglected. However, this comes at a number of disadvantages that can be quite significant. First, computed radiography is not significantly harder to perform if the equipment is available. After an initial measurement, it is also not needed to know the exact composition of the sample again and again since it will not be subject to change. Furthermore, a loss of activity after any of the steps described above can be easily seen in the radiograph, if (and only if) the exposure time remains the same. Anyways, there are two even more significant disadvantages: spatial resolution and time. AIP images will show where the plate has been exposed, so any small amount of radioactive material will be found and can be dealt with, for example, if a single strand with CsMPs flakes off the main sample¹⁰. On the other hand, gamma spectrometry can only give results for the bulk sample with no additional information about the distribution of the activity. The second issue is time, because doing an AIP exposure for the very same sample will always be quicker than gamma spectrometry. This is because, in contrast to the latter, the image plates are exposed not only by gamma, but also by beta radiation and the efficiency of absorption of β particles is much higher than that of γ rays in a given material. On top of this, sample exposures can be parallelized on a single AIP by just putting them next to each other and exposing them altogether. Since the subsequent image shows the spatial distribution of the samples, it is quite easy to discern one sample from the other. With gamma spectrometry, it would be necessary to measure each and every sample on its own, one after the other. Lastly, the spectrometer itself was needed for other purposes as well, so reserving it for months on end was impossible. All in all, these are the reasons why radiography was a choice much better suited for this application in almost every way.

After a couple of iterations of this fractionation, the most promising sample will get too small to be cut by hand with a scalpel and is ready to be passed on to the next few steps of the process (Fig. 33). The activity and radionuclide composition are measured using a gamma spectrometer, putting an emphasis on ^{137}Cs and ^{134}Cs . This is important when choosing what samples to investigate further at the USTEM using SEM imaging and it can already give an idea about the type of CsMP. The samples are then taken to the USTEM where the most promising

¹⁰In fact, this exact scenario occurred once with the Namie cloth sample. If gamma spectrometry had been used, it would have been much harder and more time-consuming to find the cause of the sudden decrease in activity of the sample after additional processing, since the extra flakes might not have been accounted for initially.

ones in terms of activity get put on a sample holder and are sputtered with the previously mentioned AuPd mixture to avoid charging issues with the electron beam. The holder is then put inside the SEM and the chamber is evacuated. The one and only goal for now is to scan each sample in its entirety and identify potential CsMPs on the basis of morphology and size. When a candidate has been identified, EDX measurements are taken to investigate the elemental composition. If this does not coincide with the necessary composition of a CsMP (e.g., no Si found), then the particle is rejected and the next one is examined. However, if the measurements agree with the expected elements of a CsMP to a large degree, the particle is extracted using the FIB.

For this purpose, a so-called *Cu FIB lift-out grid* has been fixed to another sample holder inside the evacuated chamber, where the individual particles will be later welded onto copper fingers, one entire grid by particle as to not interfere with gamma spectrometry later on. To lift out the particles from the sample, a needle is inserted into the chamber and placed near it. Objects blocking the direct path can be cut using the ion beam. The particle is then fused onto the needle using the ion beam and a tungsten gas¹¹ that results in the deposition of tungsten between the needle's tip and the particle's surface, forming a strong bond. In this thesis this is commonly referred to as *welding* the two together for easier understanding. The needle can then be carefully retracted from the bulk sample and positioned close to a Cu finger of the lift-out grid. The same process using the tungsten gas is then repeated to weld the needle tip with the particle to the finger. After this, the ion beam is used one last time to slice through the connection of the particle with the needle's tip. The CsMP candidate is now fixed to one of the Cu fingers of the lift-out grid and can subsequently be removed from the device and used for further analysis at the ATI.

Finally, the Cu grid with a single potential CsMP is put onto the gamma spectrometer to confirm the presence of radiocaesium. If at least *some* ¹³⁷Cs can be identified, it is confirmed to be, in fact, a CsMP with very high likelihood. Otherwise, the activity might either be below the lower detection threshold, or it simply is not a microparticle containing radiocaesium.

2.2.3 Experimental Challenges

There are a couple of challenges associated with the present project. These are related to the samples themselves, but also the entire extraction process that is described in the previous section 2.2.2. This short section highlights a few key challenges in these two categories that complicate the procedure. There is some speculation involved due to the complex nature of CsMPs.

Regarding the samples themselves, the presence of radiocaesium from the FDNPP accident has significantly reduced over the years, due to the natural decay of ¹³⁷Cs and ¹³⁴Cs – at the time of writing it has been around 13.5 years since the accident. With a half-life of 30.1 years for ¹³⁷Cs and 2.1 years for ¹³⁴Cs, assuming a ¹³⁴Cs/¹³⁷Cs ratio of ≈ 1 , only about 1% of the original ¹³⁴Cs and around 75% of the ¹³⁷Cs activity is still present in the samples. This results in a total loss of more than 60% of the initial radiocaesium, which is quite significant not only due to the difficulty of detecting the ¹³⁴Cs at this time, but also due to the overall reduction in detectable radiation, which can be quite low to begin with. Therefore, it is possible that the radiation emitted by a CsMP is simply too low in intensity to be picked up with any significance by the low-level gamma spectrometry setup at the ATI. But even if the ¹³⁴Cs was not detected, ¹³⁷Cs would still be enough to confirm the presence of a CsMP, even if the radiocaesium ratio could not be determined as was the case with the latest discovery of the Type E particles. In any case, measurements over longer periods of time, such as a few days, are necessary, in most cases, to get meaningful gamma spectrometry results. Another issue are bulk samples that likely contain multiple CsMPs before the FIB SEM extraction at the USTEM, but only emit comparatively little γ radiation in the order of 0.1 - 0.01 Bq. If this little activity was to be

¹¹Tungsten is only the most prominent ingredient that is deposited during the process forming the structural weld. It is not a pure tungsten gas, in fact, tungsten likely only is a very small part of it.

divided amongst multiple CsMPs, it is naturally much harder to detect every single particle. This is a large concern, since one would be unable to determine the presence of a CsMP with certainty. There are other ways, such as putting the extracted Cu grid with the particle on an AIP and exposing it for a few days, however, this would of course not be able to identify the radionuclide composition.

It might also be possible that a speculative, inactive twin of the CsMPs had been generated during the hydrogen explosions in the reactor buildings. If an uncontaminated mineral fiber of the HEPA filters was atomized and solidified without capturing any radiocaesium, these particles would have behaved identically and would be only distinguishable due to their inactive nature, which would be very hard to prove. Ultimately, they could either simply be below the lower detection threshold of the gamma spectrometer instead. This results in a similar issue to the low activity CsMPs that was described earlier. Eventually, this would require the use of significantly more complicated measurement setups and other workflows.

The workflow itself also introduced a couple of challenges, some of which could not be avoided at all. Firstly, the laboratory in which most of the sensitive work was done, such as cutting and packing the bulk samples, was also used for other radiochemistry work, possibly introducing contaminations unknowingly. Due to the extremely low activity of the CsMPs in comparison to any other work taking place in the same lab, it is easy to see that even the tiniest aerosols could accidentally land at the wrong spot and skew the results of AIP exposures or the gamma spectrometry. For this reason, it was absolutely crucial to maintain a clean work space by cleaning the surrounding area and equipment before each and every use. The same is true for the AIPs themselves, they had to remain uncontaminated throughout their usage, as to not interfere with any images. AIP exposures also had to be postponed, if any more pressing work had to be done in the same labs that included the use of radioisotopes with high activity, since it would also interfere with the exposures and lead to biased results.

As for the cutting and packing process itself, this is also a possible source of a loss in CsMPs, of course. Particles can be blown away by a slight draft, fall off of the sample and onto to the work surface, or simply stick to the scalpel during cutting. Recovery of such a lost particle would be next to impossible, due to the small size and the almost endless possibilities of their whereabouts. Although recovery is virtually impossible, such a loss would at least not go unnoticed. Missing one or several hotspots in the subsequent AIP images is a clear indication of a loss of an entire particle or even particle clusters. If only part of a cluster are lost, the drop in activity can still be observed if the exposure time remains the same between two images to compare the two. The one with the lower amount of activity will experience a smaller hotspot proportional to the missing exposure by radiation.

Additionally, it is also possible that CsMPs from near the surface of the sample get electrostatically attracted to the plastic wrap along with other particles and generic dust. In that case, it is also very difficult to recover the particles since they are entangled between a lot of other debris. Technically, the same procedure of fractionation of the contaminated piece of plastic wrap could work, however, if the particle could have been liberated from the bulk sample that easily, it will likely cling to other pieces of the subsequent packing that is necessary for the protection of the AIP. In this scenario it is likely that the CsMP only gets transferred from one material to the other without ever getting meaningfully fractionated¹².

Lastly, identifying actual CsMPs inside a sample of fibers or similar material can be very tough. Without a lot of prior experience, one can only rely on the existing morphological information, EDX spectra, and average sizes for the different known types of CsMPs. This, of course, reduces the chances of finding particles that behave in any way unexpectedly, especially if they look different from what is anticipated. Even in the best case scenario, when the sample only contains known types of CsMPs, the identification is still challenging. The sheer volume of a sample brought to SEM analysis – being limited by the amount of fractionation one can

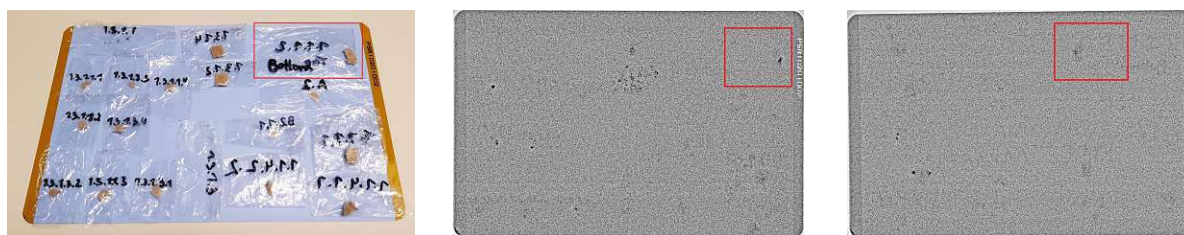
¹²This also happened once. The particle was freed from any form of fixation, making it impossible to be recovered.

perform by hand – makes searching for particles very time-consuming. Each and every fiber of the bulk sample has to be thoroughly searched and every potential CsMP has to be investigated using EDX. On top of this, at least half of the sample is covered at all times. This is because the back side of the sample cannot be viewed with the SEM (the sample is stuck to the sample holder using a bit of glue), and sometimes a fiber can occlude additional parts of the sample, for example.

3 Results

The goal was to identify, extract, and characterize potential CsMP contamination in both the Namie fleece coat and the passive air sampler disks. A representative section of the fleece coat sample was cut and thoroughly investigated, as well as all nine PUF passive sampler disks. Emphasis was put on the Namie fleece coat sample, because it was found to be significantly more contaminated by radiocaesium than the passive samplers. Before going into all of the detail regarding the specific samples, a number of general findings have been made regarding the samples and the process that are as follows:

1. The ^{134}Cs activity in all of the samples was extremely low, due to the long time gap between the accident and the evaluation. Because of this, most of the ^{134}Cs has already decayed and can no longer be detected by the ultra-low-level gamma spectrometry setup in most cases. For example, it was still possible to obtain a $^{134}\text{Cs}/^{137}\text{Cs}$ ratio for the large bulk sample of the fleece coat, however, after fractionation not a single sample could provide any meaningful ^{134}Cs signal.
2. The thickness of the plastic packaging can influence the exposure time on the AIP quite significantly. A considerable difference in hot spot size of the AIP image was observed between using a simple plastic bag and thin plastic wrap. The best results were obtained using just a single layer of plastic wrap simply to avoid contamination of the AIP.
3. Similarly, a considerable difference in exposure was found depending on which side of the sample made contact with the AIP. On large samples, hotspots that faced away from the imaging plate at the time of exposure were less noticeable. Depending on the thickness of the sample and the exposure time, this ranged from a slight decrease in intensity up to almost complete shadowing of the hotspot. This is because of self-absorption of the β radiation inside the sample. For this reason, all samples were exposed twice for their top and bottom surfaces if applicable. This ensures that no hot particle would be missed, especially if the orientation had changed accidentally during cutting, which was the case for some already quite small samples. A representative example of this effect is shown in figure 35.
4. Although rare, in some cases the labeling on the plastic wrapping of the samples was clearly visible in the exposed AIP images. This behavior could never be replicated after the initial appearance. No changes were made to the exposure location, utilized AIP, and sample packing procedure that would warrant the appearance of an artifact this significant. All labeling was done using a black permanent marker on the inside of the plastic wrap. The permanent marker and AIP were free of contamination. A drastic example of this exact behavior can be seen in figure 36. The source of this phenomenon could not be conclusively identified and it seemingly occurred randomly.
5. Significant contamination of some of the samples occurred once during the cutting and re-packing process after work with ^{134}Cs in the same laboratory. A tiny amount of the ^{134}Cs was detected on several wipe tests around the lab using the low-level gamma spectrometer. No contamination was detectable with any of the standard contamination detection equipment, however, this tiny amount of ^{134}Cs was enough to completely throw off the sensitive AIP exposures by a factor of 10 at least. Some of the radiocaesium apparently stuck to the plastic wrap, which had to be changed. Fortunately, it did not contaminate the insides of the packaging with the precious samples themselves. Therefore, special care had to be taken to always clean the work surface and tools before working with the samples.



(a) Highlighted in red: A fractionated sample of the Namie fleece coat, whose top and bottom sides were exposed for this representative test.

(b) Highlighted in red: The resulting exposure with the top side of the sample being closest to the surface of the AIP.

(c) Highlighted in red: The resulting exposure with the bottom side of the sample being closest to the surface of the AIP.

Figure 35: Difference in hotspot size and shape on the evaluated AIP image for the same sample, depending on which side was exposed due to self-absorption. Exposure time was ≈ 2 days in both cases.



(a) The AIP setup with all of the packaged samples lying on top of the imaging plate.

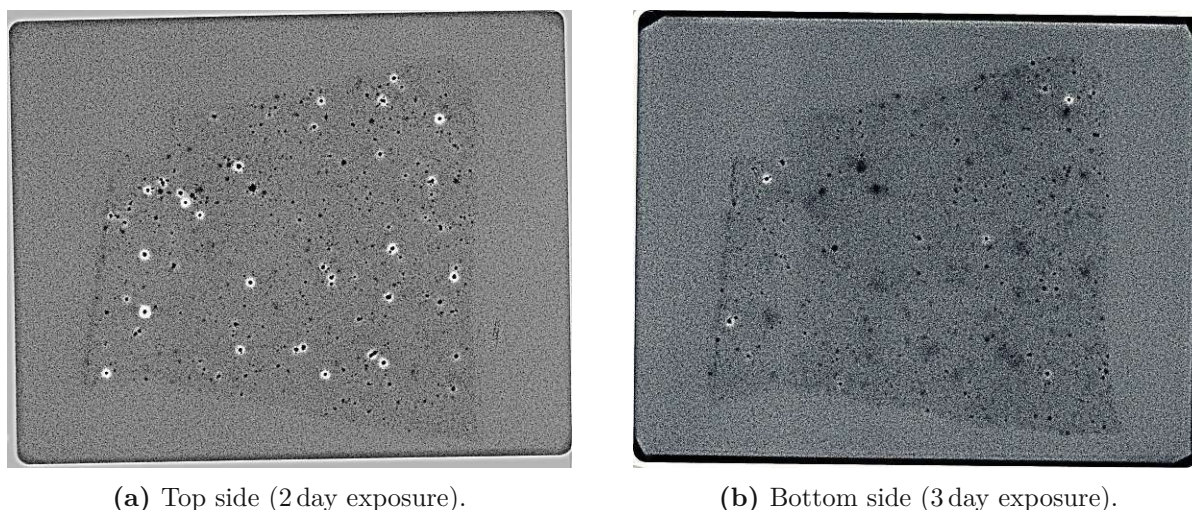
(b) The evaluated AIP exposure with clearly visible labeling artifact.

Figure 36: Rare case of an AIP artifact, where the permanent marker labeling on the plastic wrap can be clearly seen. In this extreme example, the labeling is as bright and sometimes even brighter than the proper sample hotspots themselves.

3.1 Namie Fleece Coat

Before doing any AIP exposures, the fleece coat sample in its entirety was analyzed using gamma spectrometry for close to three days. It was found to contain only radiocaesium of the isotopes ^{134}Cs and ^{137}Cs . Calculated back to the time of the accident, it contained a weighted average activity of $60.7 \pm 2.2 \text{ Bq } ^{134}\text{Cs}$ and $67.2 \pm 0.9 \text{ Bq } ^{137}\text{Cs}$. The resultant $^{134}\text{Cs}/^{137}\text{Cs}$ ratio therefore equates to 0.90 ± 0.03 , which correlates to the caesium ratio of Unit 1 as the possible source and corresponds well with the ratio of the entire fleece coat upon collection.

Next, the fleece coat sample was put on an AIP for radiography. Both top and bottom sides were exposed and an area of interest was identified that was easy to isolate and contained a large number of hotspots on the exposed image. It was subsequently cut from the bulk fleece sample and put on the AIP for exposure according to the work flow. The top and bottom side exposures of the fleece coat sample are shown in figure 37. These are not the original exposures that were done initially, though, recognizable by the missing top left corner. Due to a lack of large-enough image plates, the initial exposure was done with an AIP that would not fit the entirety of the sample, cutting off at the edges. For this reason, the radiography was repeated at a later point with an AIP of adequate size. In the resultant image, there is a clear difference between the top and bottom sides of the fleece, which is expected since one of the sides must have been the outer surface of the original fleece coat. Furthermore, as expected, the radioactivity is distributed very discretely in visible hotspots all over the two sides. The intensity of these spots randomly differs a lot over a broad range. On top of this, in some cases, self-absorption can be seen quite well,



(a) Top side (2 day exposure).

(b) Bottom side (3 day exposure).

Figure 37: AIP images of the top and bottom sides of the Namie fleece coat sample in its entirety. A literal corner was cut to investigate the material in this thesis.



(a) Photo of the bulk fleece with the cut corner.

(b) AIP image of the bulk fleece with the clearly missing corner and the piece of fleece that was further investigated.

Figure 38: The starting point of the fractionation process for the fleece sample was this corner material that was cut from the bulk sample. The AIP was exposed for ≈ 6 days.

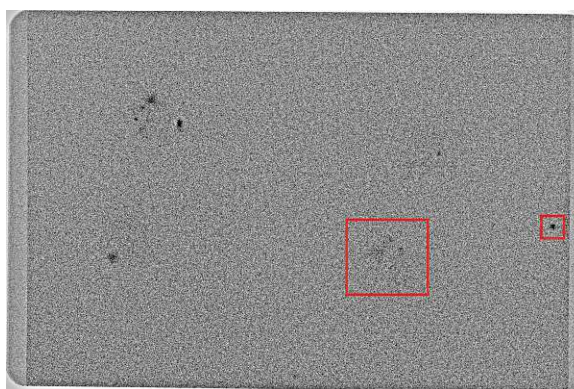
because the intensity of the same spot on both sides can be very different. For some hotspots, it can also be estimated that the source of the radiation lies in between the two surfaces. This is the case if the intensities on both sides are almost equal.

The corner that was cut from the sample and its AIP image can be seen in figure 38. This was a good starting point for the following fractionation process. It contained a large number of smaller hotspots and one of special interest near the middle. The rest of the fleece was left untouched and might be used in future studies of CsMPs. Figure 38b shows a comparison of the corner piece with the rest of the bulk fleece. The horizontal line near the top of the image is a readout artifact from the evaluation and does not otherwise affect the image results.

The new corner sample underwent the fractionation process for a few of months, during which the workflow was tested, fine-tuned (e.g., gamma spectrometer vs. AIP, exposure times, etc.), and complications (e.g., contaminations, loss of particles, etc.) were dealt with. At this point, it cannot be stressed enough that it is important to use AIPs regularly if not during the entire process as it was the case for this thesis. During the very first iteration of the fractionation cycle, where the corner piece was quartered, a tiny bunch of fleece fibers flaked off of the main sample and was only found during the evaluation of the AIP exposure. This is shown in figure



(a) Photo of the quartered corner piece during the very first fractionation cycle. The main sample and the tiny, detached fiber bundle are highlighted in red.



(b) AIP result with the hotspot of the detached bundle being much more prominent than the main sample itself. Both are highlighted in red.

Figure 39: Radioactive bundle of fibers detached from the main fractionated sample inside the plastic bag, highlighting the importance of radiography during the fractionation process.

39. This fiber bundle could have easily been missed, had it not been inside the plastic bag and on the image plate during exposure.

The fractionation process produced a total of 106 samples that were each ran through AIP exposures at least once, if large enough at least twice (front and back sides). A representation of this is shown in figure 40 – it shows a tree diagram of all the samples and their place in the hierarchy. The blue colored sample up top was the corner piece mentioned previously, which was the starting point for all the latter samples. The samples highlighted in green are those that were taken for further examination to the USTEM. All of these are labeled just like described in the previous section 2 with two exceptions. Sample labels containing the letter P typically were found detached from the main sample, i.e., in a small, inconspicuous bundle. Sample labels containing the letter F or FH were samples where a particle was caught inside the plastic wrap over and over again, completely detached from any of the original fibers. Typical exposure durations for the AIPs were between 1 - 3 days at most. Most of the hotspots on the AIP images were over-exposed on the three-day exposures (typically weekends), however, since spatial resolution does not need to be the best in that case, this was not an issue in any way.

In the end, five fractionated samples from the Namie fleece coat sample were selected for further processing at the USTEM. This included SEM imaging, EDX, and potential FIB SEM extraction. The samples and the respective results will be discussed in more detail in the following sections.

Die approbierte gedruckte Originalversion dieser Diplomarbeit ist an der TU Wien Bibliothek verfügbar
The approved original version of this thesis is available in print at TU Wien Bibliothek.

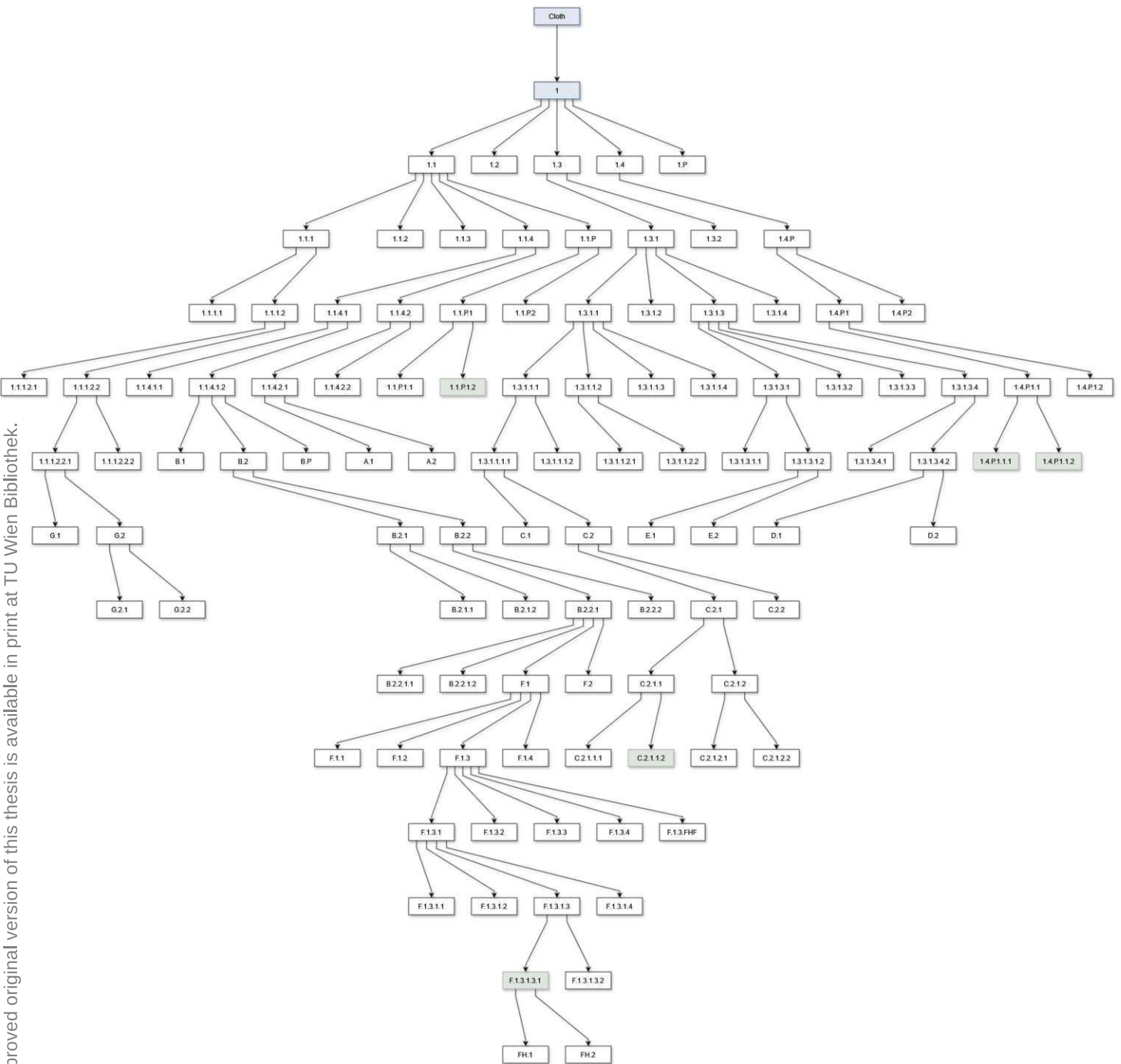


Figure 40: Hierarchical tree diagram of all the investigated samples of the Namie fleece coat sample. The blue color represents the starting point of the entire sample chain with the first sample piece cut from the bulk fleece. The green colored samples represent those that were examined at the **USTEM** using **SEM** imaging (5). In total 106 samples were produced from a small section of the bulk fleece.

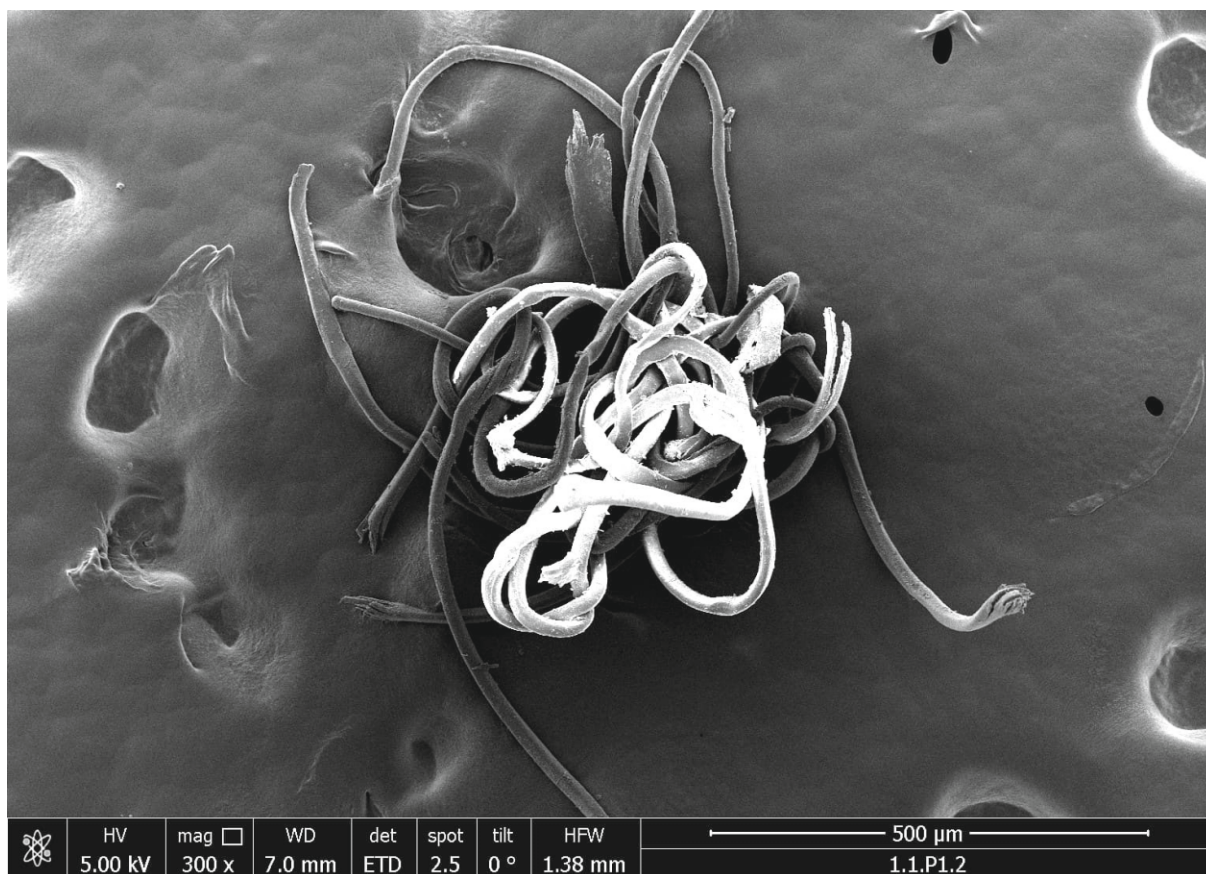


Figure 41: Overview image of sample 1.1.P.1.2 – Part 1/2.

3.1.1 Sample 1.1.P.1.2 – Part 1/2

The sample 1.1.P.1.2 was halved and the two parts were taken to the **USTEM** on two separate occasions, using different equipment. This was the first examination of one of the halves at **USTEM**, hence part 1/2.

According to gamma spectrometry, the entire sample contained a weighted average activity of 0.227 ± 0.058 Bq of ^{137}Cs pre-**USTEM**, calculated back to the time of the accident (3 h measurement period, 1.960σ). No ^{134}Cs could be detected. This is one of the highest activities among all of the individual samples that were taken to **USTEM**. An overview of the sample is shown in figure 41. As expected it shows a tight bundle of fibers with some charge issues in the middle in spite of sputtering it with the AuPd mixture. This image was taken with the FEI Quanta 200 FEG at **USTEM** (not the **FIB SEM**). Most of the fibers and particles on the surface contained largely of C and O, which was expected. Other than that, no abnormalities could be identified. Interestingly, upon activating the **EDX** mode of the device, particles specifically containing Si lit up brightly and it was much easier to find them than before. This phenomenon could not be reproduced with the **FIB SEM** at all.

Due to this, a spherical particle was found that resembled known **CsMPs** very well, both in morphology as well as in size. An image of it is shown in figure 42. Interestingly, to the right side of the particle, there seems to be a small crack or similar, which was probably the reasons why it took much more charge than any of the other regions. This small region probably was the source of a lot of image errors and artifacts due to the excess charging.

The elemental composition of the particle is shown in table 9. It can be seen that, with around 5%, Si is the third most common element in this sample by weight. This is far from the shares of C and O in the **EDX** spectrum. However, it has to be kept in mind that the depth of penetration which contributes to the overall **EDX** signal is a few micrometers large, which means that a large portion of the signal comes from the background fiber on which the sphere

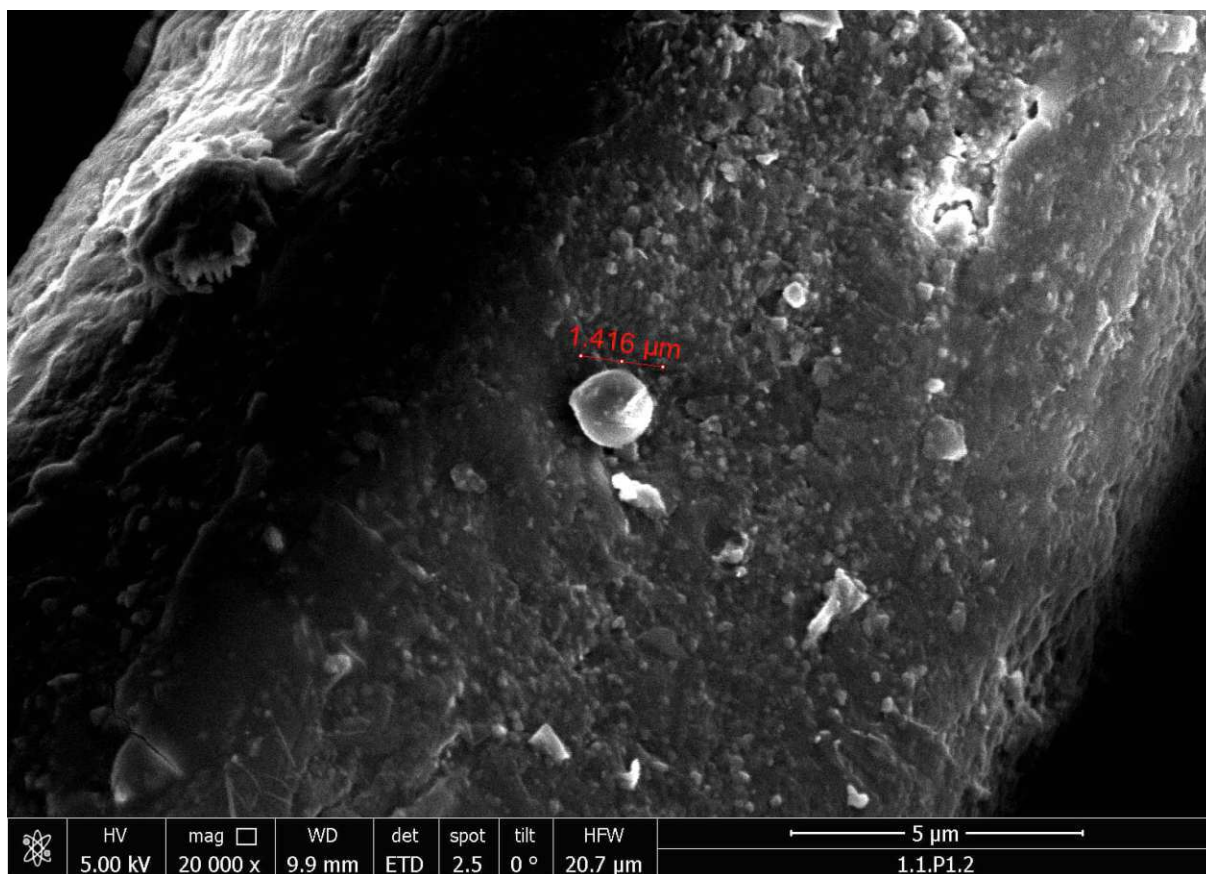


Figure 42: Image of the spherical particle that was brightly visible in EDX mode. This approximately 1.4 μm large particle was a potential CsMP-candidate. A possible crack can be seen to the right of the particle, this portion introduced charge issues.

Table 9: Elemental composition of the spherical particle obtained by EDX. C and O are over-represented to an uncertain degree due to the penetration depth of the electron beam and the small diameter of the particle.

Element	Mass %	Atomic %	Net Int.	Error %
C K	49.0	60.5	546.9	3.3
O K	34.0	31.4	396.2	7.8
Al K	1.9	1.1	52.8	7.1
Si K	9.2	4.8	269.2	3.2
Ca K	5.9	2.2	84.0	7.4

rests. The fibers mostly consist of C and O, hence naturally skewing the results in that direction. Other than Si, Al and Ca have also been found. Charging made it hard to document the entire extraction process of the particle. Images would often have heavy artifacting, especially after lifting the particle off of the fiber. For this reason, no further images of the process can be presented here. Anyways, some fibers needed to be cut in order to get sufficient access to the location of the particle. After this was done, the particle was picked up by the needle and transferred to a Cu lift-out grid as normally.

After the extraction, the entire lift-out grid was put on the ultra-low-level gamma spectrometer again for a thorough examination of 114 hours – no Cs-137 peaks could be identified in the spectrum. Taking into account the limits of the device (ISO 11929), with a **minimum detectable activity (MDA)** of 1.5×10^{-2} Bq and a decision level of 7.2×10^{-3} Bq, the confidence interval lower

limit was placed at 8.1×10^{-4} Bq and upper limit at 1.6×10^{-2} Bq (5% confidence level). The weighted mean activity lies just below the decision level for the spectrometer.

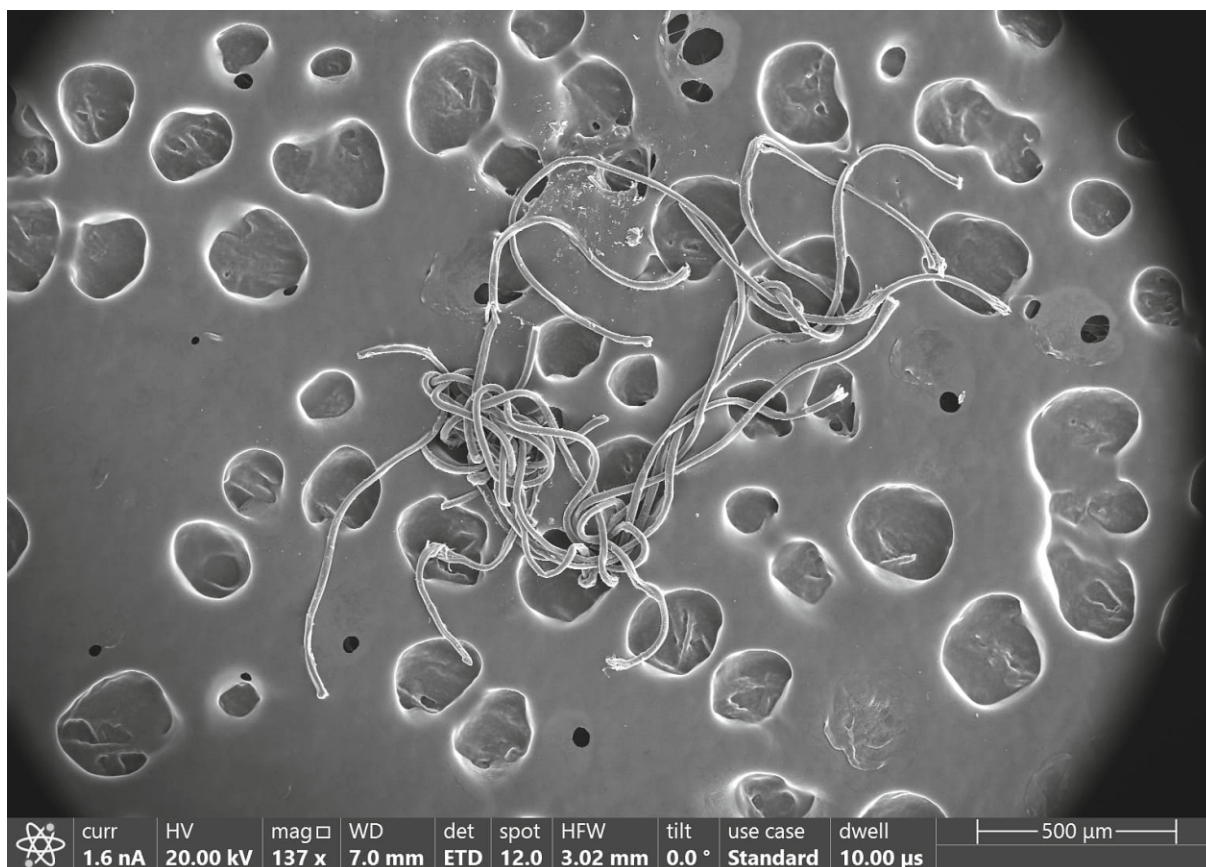


Figure 43: Overview image of sample 1.1.P.1.2 – Part 2/2.

3.1.2 Sample 1.1.P.1.2 – Part 2/2

This is the second part of the sample 1.1.P.1.2 that was left from the first [USTEM](#) examination. An overview of the bundle of fibers is shown in figure 43. This image was taken using the [FIB SEM](#) at a later examination date at the [USTEM](#) than the first half of the sample.

Unfortunately, no particles of interest could be identified morphologically that also passed the [EDX](#) checks. Particles with traces of Na, Al, Ca, and Cu were quite common to see with one also exhibiting traces of Si. By far the most common elements were C and O again as expected. Therefore, no particles were extracted from this sample.

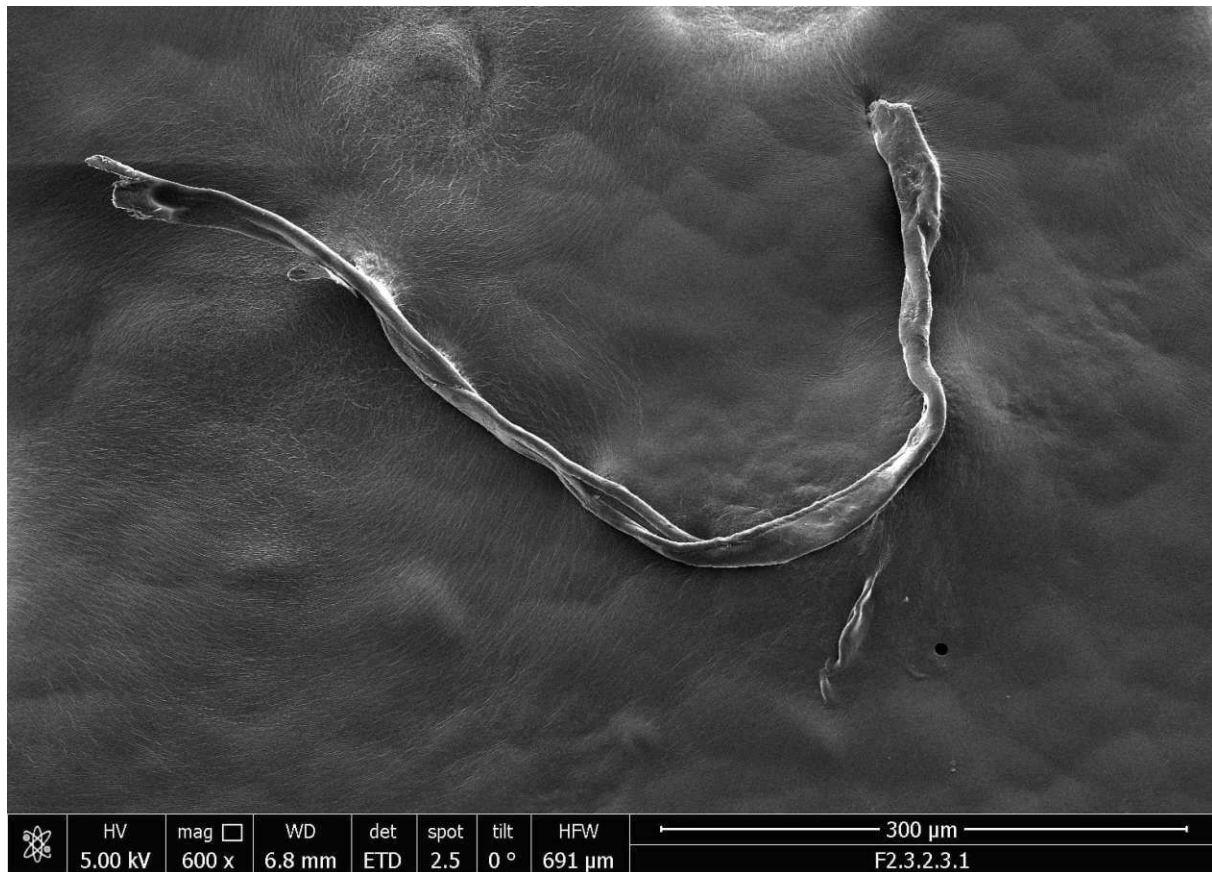


Figure 44: Overview image of sample F.1.3.1.3.1.

3.1.3 Sample F.1.3.1.3.1

The sample F.1.3.1.3.1 originated from a series of tries to recover a hotspot (i.e., an individual particle or cluster of particles) on the AIP images that was stuck to the insides of the plastic wrap after one of the fractionation steps. Originally, it was part of a standard bundle of fibers from the Namie cloth similar to the others. It was also looked into on the first day using the conventional SEM. The yield was not great, however a large fiber could be recovered, an overview of which is shown in figure 44. According to gamma spectrometry, this sample contained a weighted average activity of 0.249 ± 0.026 Bq of ^{137}Cs pre-USTEM, calculated back to the time of the accident (18 h measurement period, 1.960σ). No ^{134}Cs could be detected.

Unfortunately, no particles of interest could be identified morphologically that also passed the EDX checks. Particles with traces of Ca were by far the most prevalent ones next to, of course, the usual primary elements C and O. Traces of Mg, Al, and Cl were also found. Anyways, no particles were extracted from this sample.

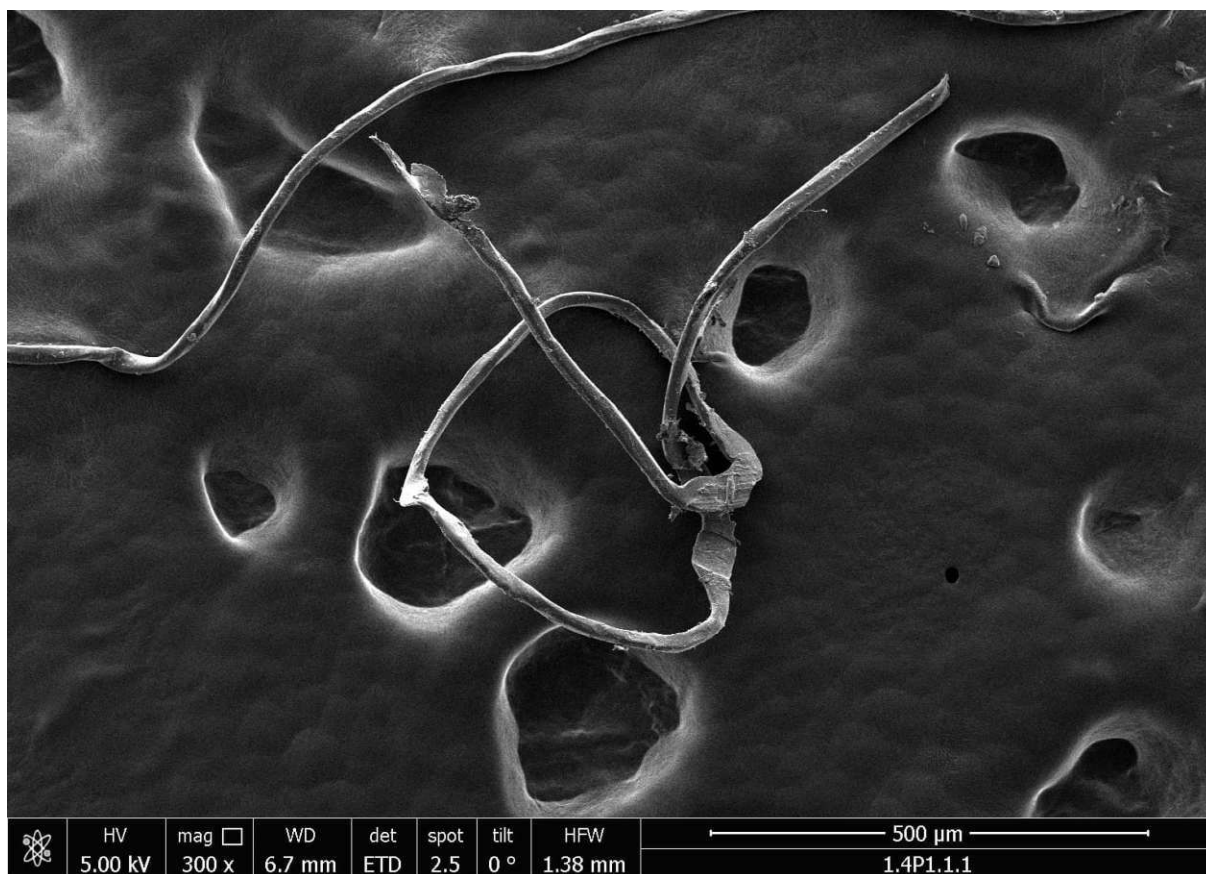


Figure 45: Overview image of sample 1.4.P.1.1.1.

3.1.4 Sample 1.4.P.1.1.1

This sample (1.4.P.1.1.1) together with the next one (1.4.P.1.1.2) were produced by halving of a common precursor sample. This was done by carefully pulling fibers apart under a standard optical microscope using two fine canulae. The precursor sample was only visible as a single, fairly bright hotspot on the AIP images. After the physical separation, interestingly, both samples had nearly identical levels of ^{137}Cs . A weighted average activity of $0.016 \pm 0.008 \text{ Bq}$ of ^{137}Cs was measured for this sample using gamma spectrometry, calculated back to the time of the accident (89 h measurement period, 1.960σ). No ^{134}Cs was found. An overview of the sample is shown in figure 45. It only consisted of a few fibers carefully pulled from the rest of the precursor sample and even fewer made it from the plastic wrap onto the sample holder. As a result, two large fibers were mainly analyzed. These are shown in the overview image.

In this sample, not a lot of CsMP candidates could be identified, most particles either turned out to be part of, or related to the fiber itself, or just do not contain a significant amount of Si. One particle was found to contain traces of Al, Si, and Fe next to the usual C and O. However, the main focus was another particle that looked less spherical but more angular in nature. At first, it was also looked at with the FEI Quanta 200 FEG. For this reason, it too lit up brightly in EDX mode and was thus quickly identified as a potential CsMP. An image of the particle is shown in figure 46. It shows a more angular particle that is roughly $2.4 \mu\text{m}$ in diameter. Although not the usual CsMP from a morphological standpoint, the EDX spectrum looked very promising, the results of which are shown in table 10. Although, C and O are, again, overrepresented due to the penetration depth, it contained large amounts of Si, Ca, and Ti, as well as some Al. This would fairly well match up with known EDX spectra of CsMPs, which is the reason we decided to extract it.

The lift-out process for the particle is documented with the images shown in figure 47. It starts with the extraction needle being positioned right next to it and ends with welding the

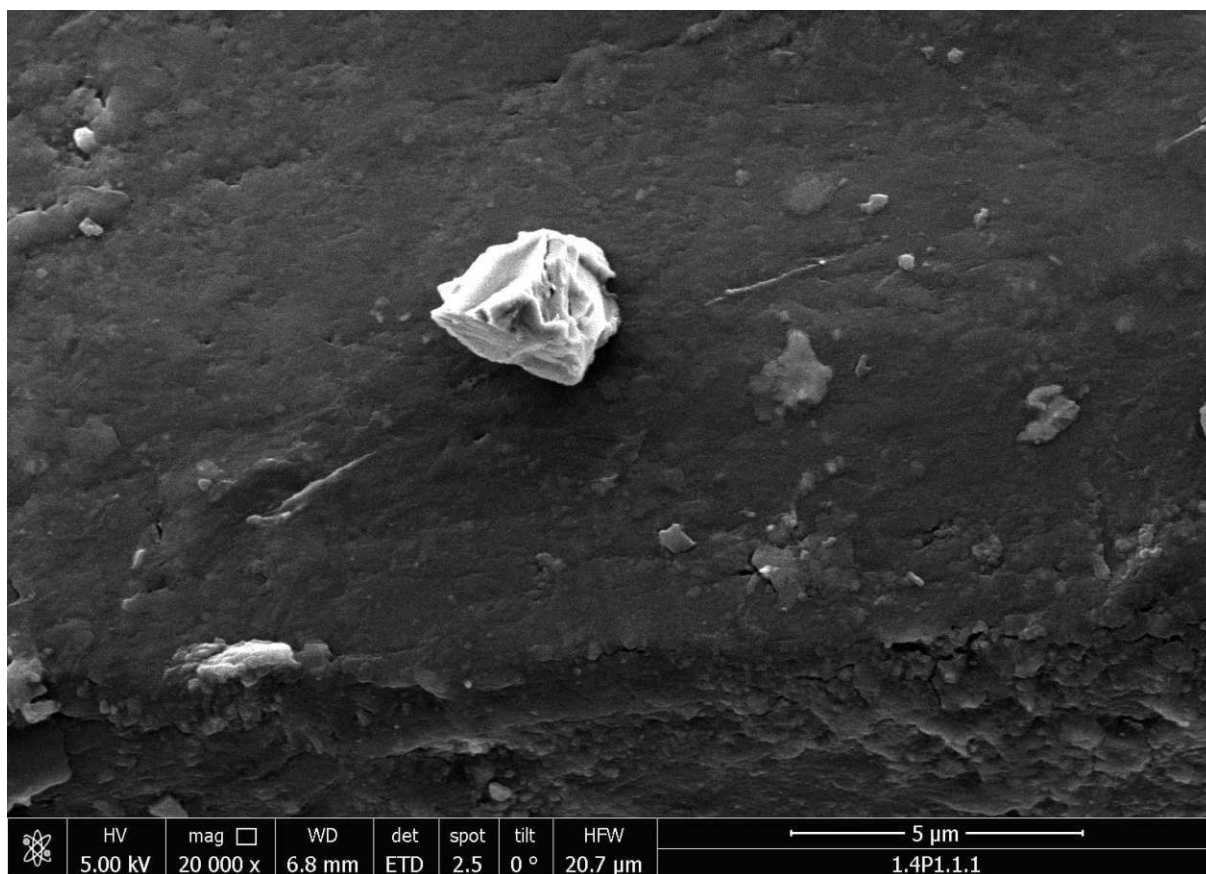
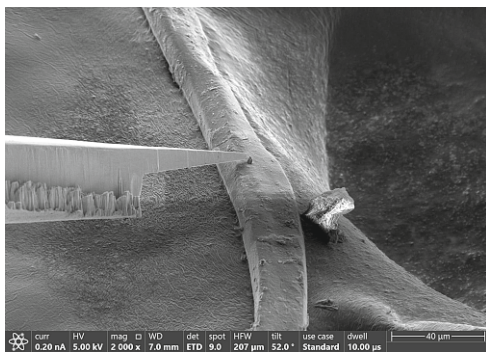


Figure 46: Image of the angular particle that was brightly visible in EDX mode. This approximately 2.4 μm large particle was a potential CsMP-candidate.

Table 10: Elemental composition of the angular particle obtained by EDX. C and O are over-represented to an uncertain degree due to the penetration depth of the electron beam and the small diameter of the particle.

Element	Mass %	Atomic %	Net Int.	Error %
C K	25.4	39.8	217.8	3.9
O K	33.9	39.9	280.8	7.8
Al K	1.5	1.1	32.6	6.4
Si K	9.5	6.4	221.9	2.8
Ca K	15.0	7.1	179.8	2.9
Ti K	14.1	5.5	139.1	2.9
Fe K	0.5	0.2	3.4	46.1

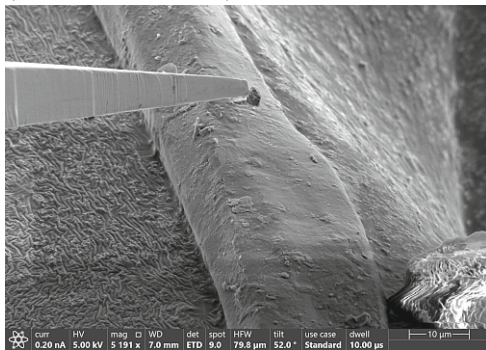
particle to the Cu lift-out grid and cutting the weld connecting it with the needle. The step-by-step process was shortly described in section 2. Finally, the lift-out grid with the single particle was taken back to the ATI and put on the ultra-low-level gamma spectrometer. It, unfortunately, was not able to identify any ^{137}Cs after a 116 h measurement period. Taking into account the limits of the device (ISO 11929), with an MDA of 1.5×10^{-2} Bq and a decision level of 7.2×10^{-3} Bq, the confidence interval lower limit was placed at 3.2×10^{-4} Bq and upper limit at 1.3×10^{-2} Bq (5% confidence level). The weighted mean activity lies significantly below the decision level for the spectrometer.



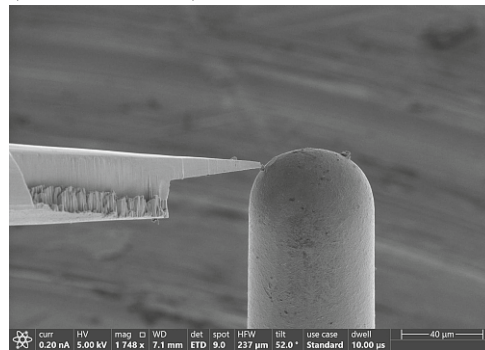
(a) Extraction needle next to the particle (far electron image).



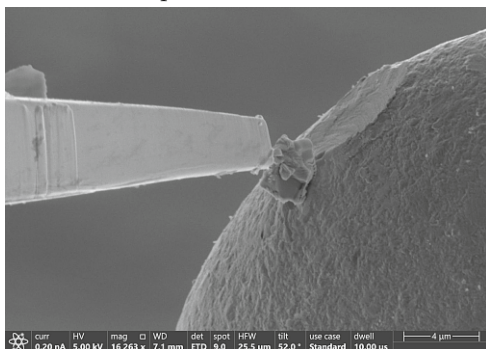
(b) Extraction needle next to the particle (near ion image).



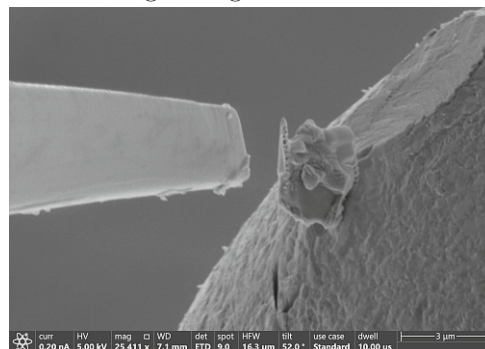
(c) Particle welded to the needle and lifted from the sample.



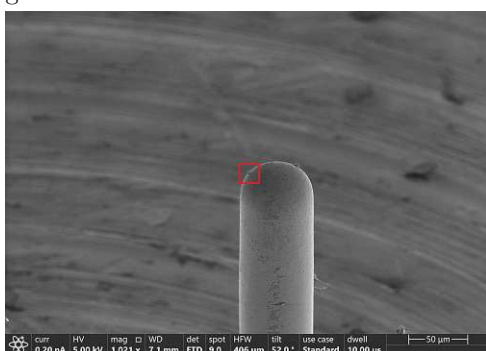
(d) Needle with particle on its tip next to the lift-out grid finger.



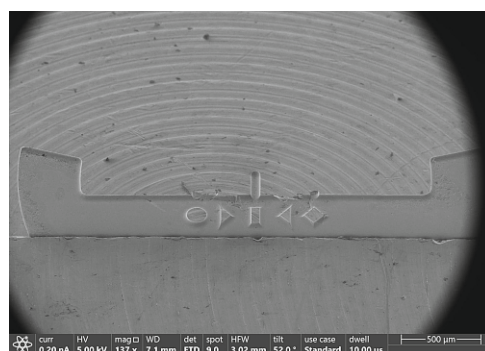
(e) Particle welded to the lift-out grid finger.



(f) Weld between the particle and needle is cut.



(g) Particle welded to lift-out grid, see red highlighting.



(h) The entire lift-out grid with one tip for the single particle.

Figure 47: Images of the entire extraction process for the angular particle, i.e., a potential CsMP, starting from the insertion of the extraction needle up to the weld onto the Cu lift-out grid and cutting from the needle.

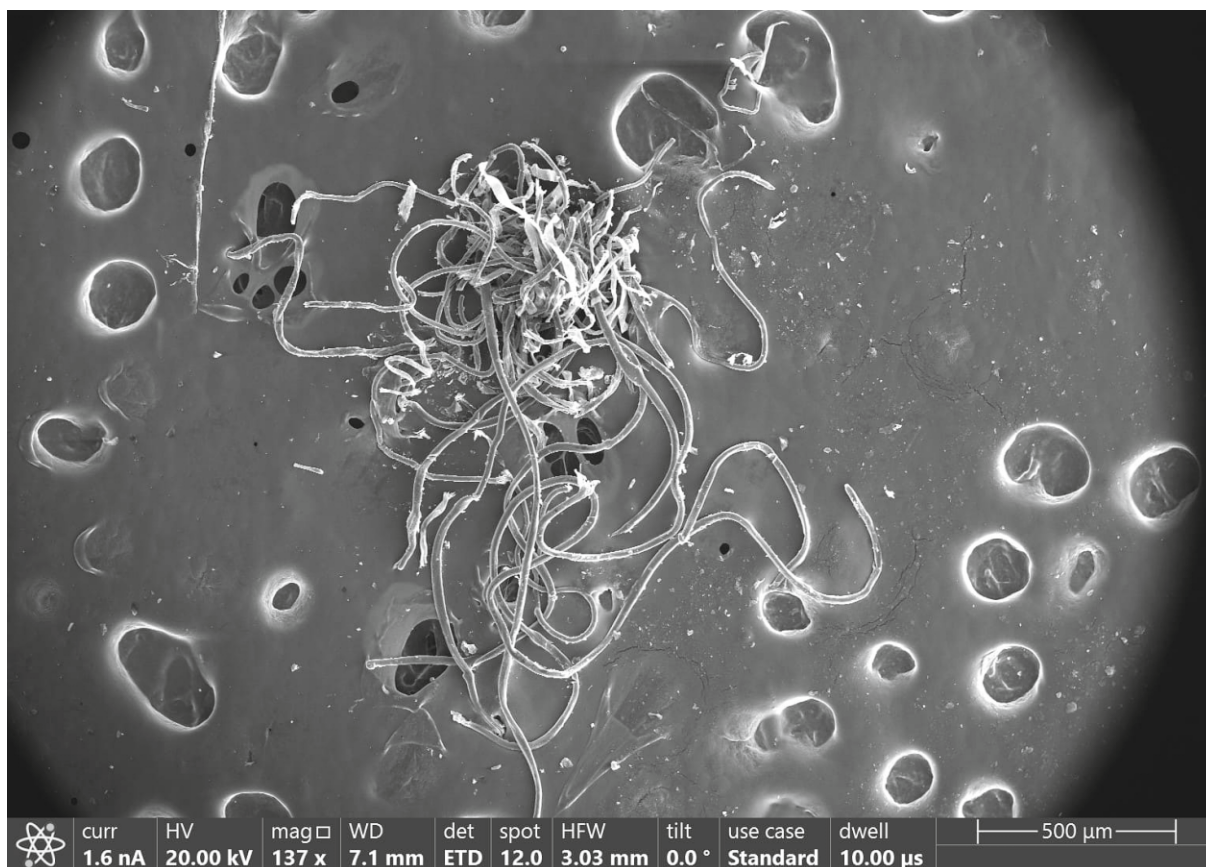


Figure 48: Overview image of the top region of sample 1.4.P.1.1.2 with the main bulk of the fleece fibers.

3.1.5 Sample 1.4.P.1.1.2

As mentioned in section 3.1.4, this sample had about the same activity as its *sibling*. The gamma spectrometer was able to detect 0.015 ± 0.006 Bq of ^{137}Cs , as of the time of the accident (68 h measurement period, 1.960σ). Again, no ^{134}Cs was found. Overview images of the regions of the sample are shown in figures 48 and 49. One specific fiber in the sample was extremely long (multiple mm) compared to the fibers from any of the other bundles. Though too long to fit into the images, the fiber has been searched along its entire length. Two particles were found that were the main focus of this sample. The first particle mainly contained C and O with about 6 atom % of Si. No other elements were significant enough for detection in this particle, therefore it was less interesting than the following particle.

The second particle was a lot more promising since it fit both the morphologic description of a CsMP and also included some of the elements typically expected in CsMPs. An image of the particle can be seen in figure 50. The data gathered from the EDX spectrum in table 11 revealed significant amounts of Al and Si, but also traces of Na, Mg, K, Ca, and Fe. There is also a significant higher ratio of O/C when compared to any of the previous microparticles or even the fibers themselves, indicating a potentially higher number of oxides in the sample (e.g., SiO_2). In any case, due to the small size, the fiber behind the microparticle still skewed the results in favor of C and O, so the relative amount of Si, Al, etc. will likely be significantly higher in reality.

This particle was successfully extracted from the bulk sample. The extraction process can, again, be seen in figure 51. In principle, the same procedure as discussed previously is repeated for each particle that needs to be lifted out. In the case of this sample, the spherical microparticle was the only one being promising enough to justify an extraction. After this, the lift-out grid with the particle was placed on the gamma spectrometer again, this time together with another

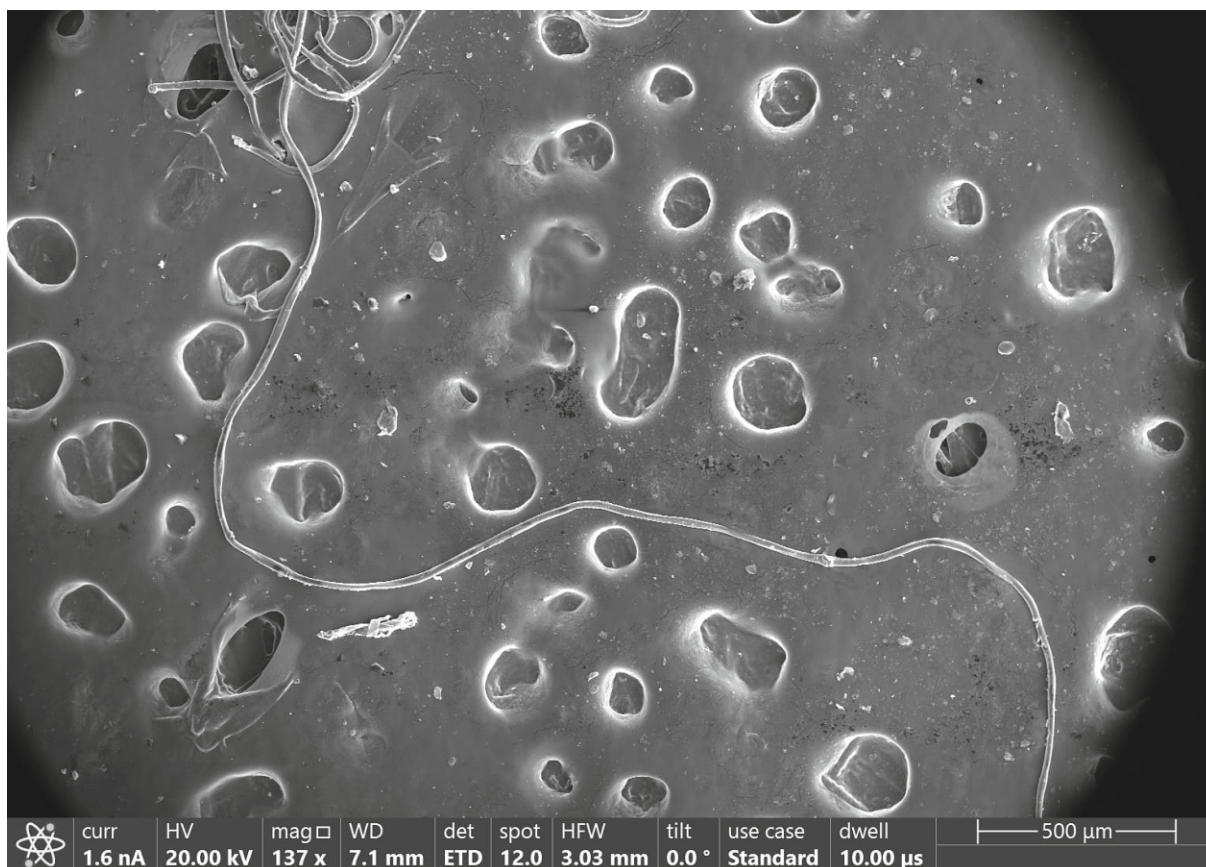


Figure 49: Overview image of the bottom region of sample 1.4.P.1.1.2 with a single fiber stretching over large portions of the sample holder.

microparticle from one of the passive air samplers¹³, just to increase the amount of potential radioactivity from the samples on the detector in relation to the constant background radiation. This saved time and increased the chances to detect anything at all, due to all of the previous experiences with no detection of any radiation from the extracted microparticles at all. After a 114 h long measurement, no ^{137}Cs could be identified. Once again, taking into account the detection limits (ISO 11929), with an MDA of 1.5×10^{-2} Bq and a decision level of 7.4×10^{-3} Bq, the confidence interval lower limit was placed at 1.4×10^{-4} Bq and upper limit at 1.0×10^{-2} Bq (5% confidence level). The weighted mean activity lies significantly below the decision level for the spectrometer.

¹³This will be presented in the next section 3.2. It was extracted on the same day, so both needed to be measured anyways.

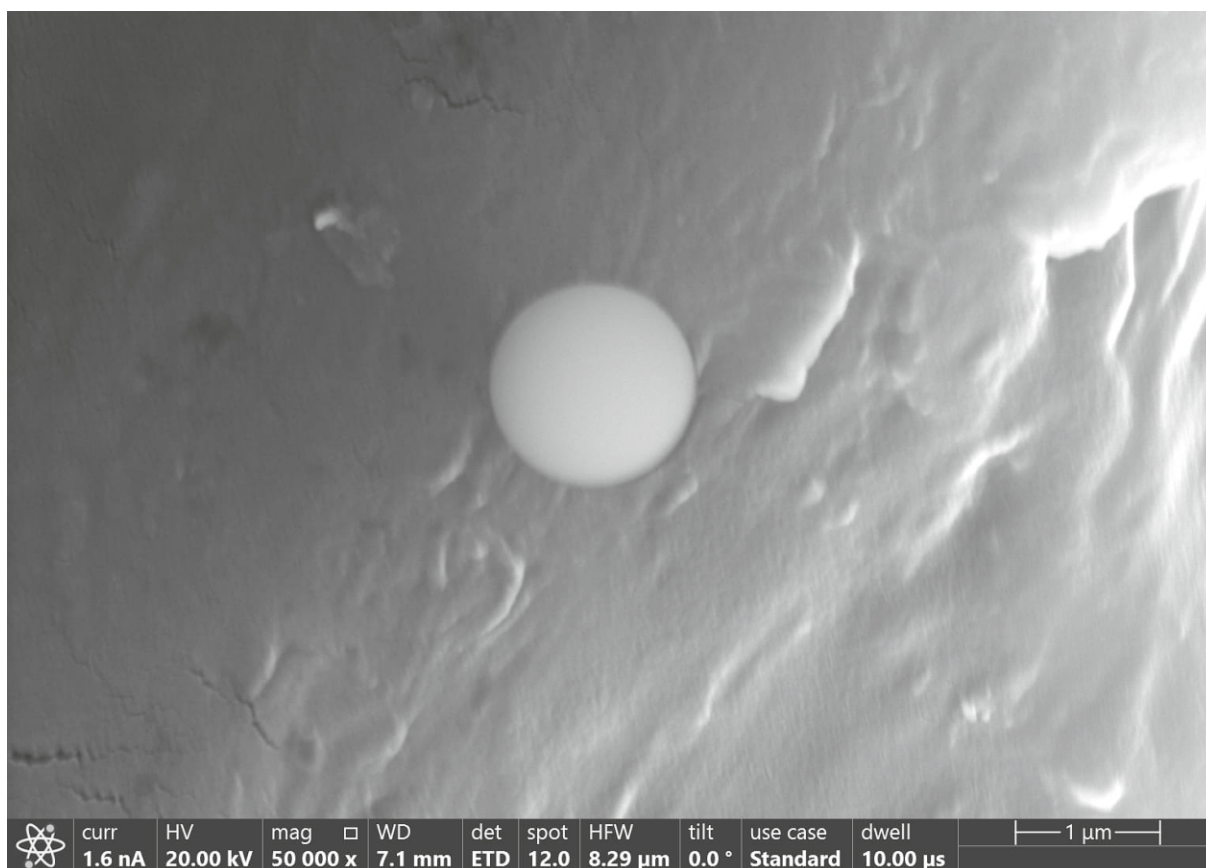
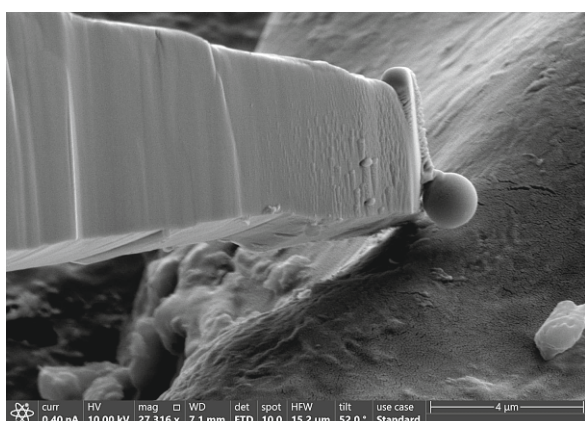


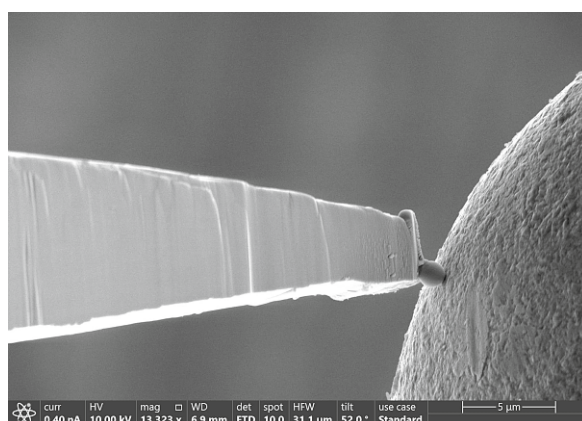
Figure 50: Image of the perfectly spherical particle that was found on a fleece fiber. This approximately 1.4 μm large particle was a potential CsMP-candidate due to its shape, size, and elemental composition.

Table 11: Elemental composition of the perfectly spherical particle obtained by EDX. C and O are over-represented to an uncertain degree, due to the penetration depth of the electron beam and the small diameter of the particle. Pd and Au stem from the sputtering process.

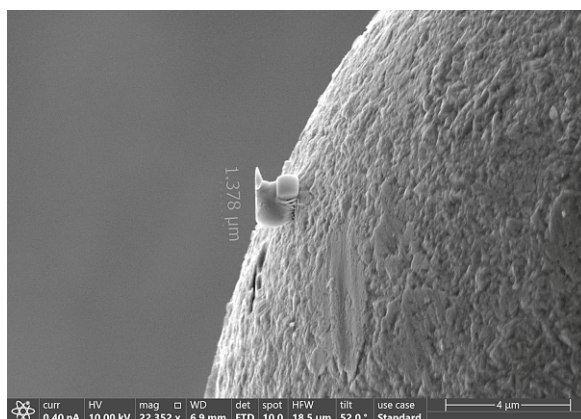
Element	Mass %	Mass % Error	Atomic %	Atomic % Error
C K	25.5	±0.2	36.9	±0.3
O K	47.0	±0.3	51.0	±0.3
Na K	0.9	±0.0	0.7	±0.0
Mg K	0.4	±0.0	0.3	±0.0
Al K	6.6	±0.1	4.2	±0.0
Si K	7.4	±0.1	4.6	±0.0
K K	0.8	±0.0	0.3	±0.0
Ca K	0.5	±0.0	0.2	±0.0
Ti K	0.2	±0.0	0.1	±0.0
Fe K	2.0	±0.1	0.6	±0.0
Cu K	0.2	±0.1	0.1	±0.0
Pd L	3.3	±0.1	0.5	±0.0
Au L	5.1	±0.3	0.4	±0.0



(a) Particle welded to the extraction needle and lifted off of the sample.



(b) Needle with particle on its tip position next to the Cu lift-out grid tip, where the particle will be welded to.



(c) Particle welded to lift-out grid and cut from the needle.

Figure 51: Images of the extraction process for the spherical particle, i.e., potential CsMP, starting from the welding to the extraction needle up to the weld onto the Cu lift-out grid and cutting from the needle.

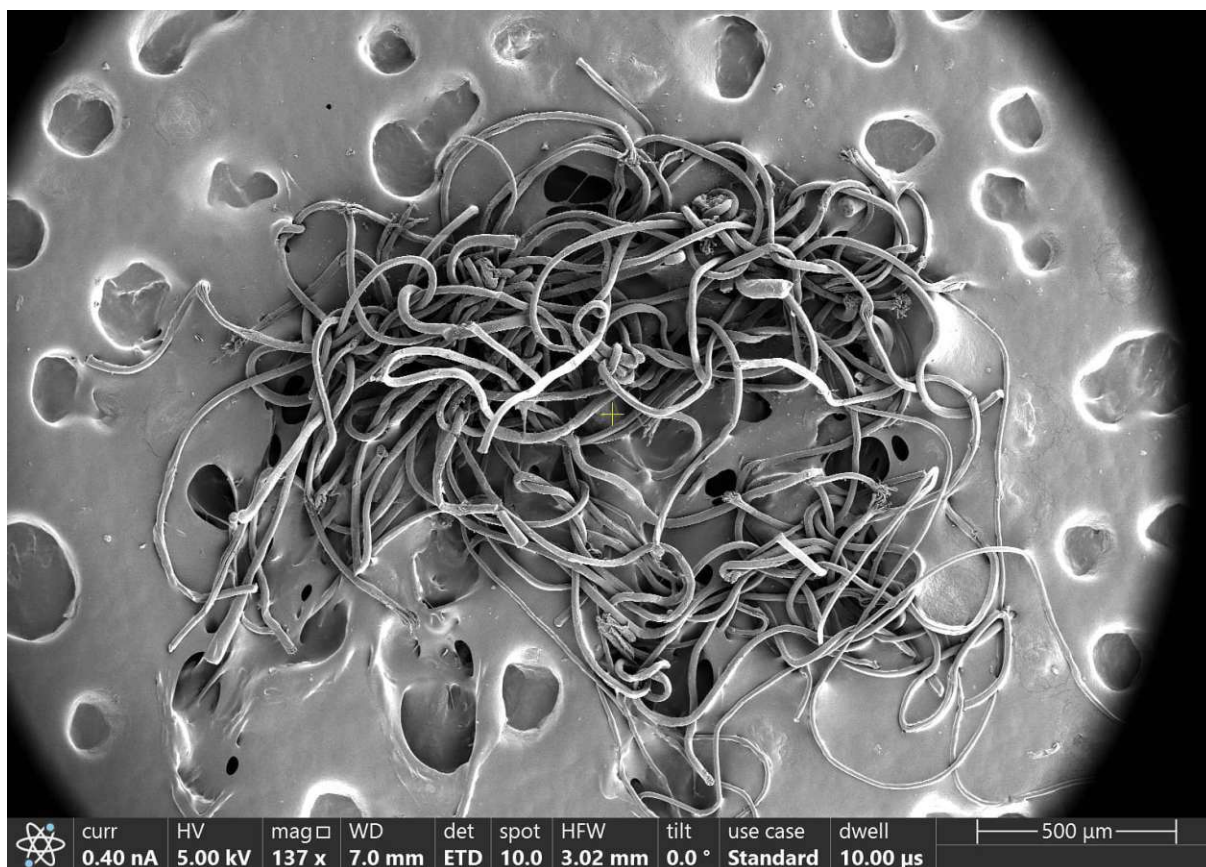
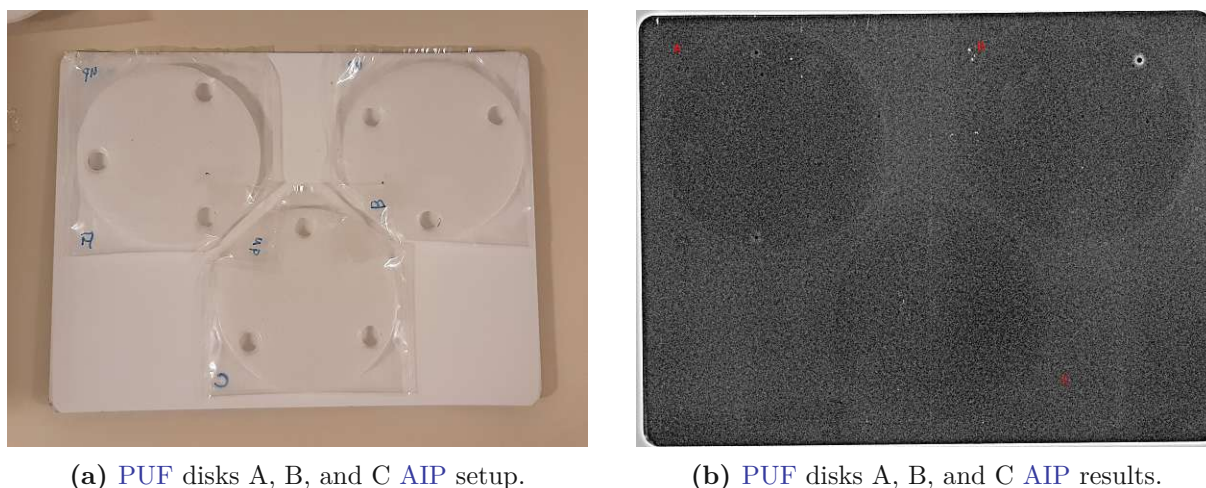


Figure 52: Overview image of sample C.2.1.1.2.

3.1.6 Sample C.2.1.1.2

Sample C.2.1.1.2 was by far the one with the most fractionation steps that made it intact to the **USTEM**. Like the others, it too was a bundle of fibers from the coat, this time still fairly large in order to minimize the risk of another loss of particles. At the end of the process, the usual gamma spectrometry detected a weighted average activity of 0.121 ± 0.081 Bq of ^{137}Cs , calculated back to the time of the accident (1 h measurement period, 1.960σ). No ^{134}Cs could be detected. The overview image of the sample is shown in figure 52.

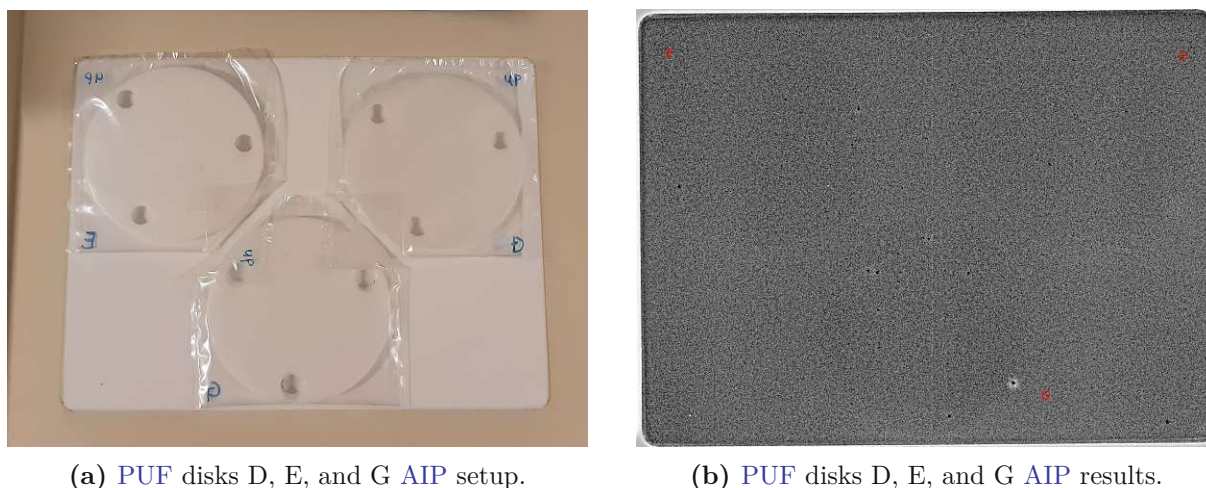
Unfortunately, no particles of interest could be identified morphologically that also passed the **EDX** checks. Some particles with traces of Na, Mg, Al, and Ti have been found, together with the abundant C and O. Not a single particle with traces of Si could be identified. Therefore, no particles were extracted from this sample.



(a) PUF disks A, B, and C AIP setup.

(b) PUF disks A, B, and C AIP results.

Figure 53: Setup and radiography results of the PUF disks A, B, and C after ≈ 11 weeks of exposure on an AIP.



(a) PUF disks D, E, and G AIP setup.

(b) PUF disks D, E, and G AIP results.

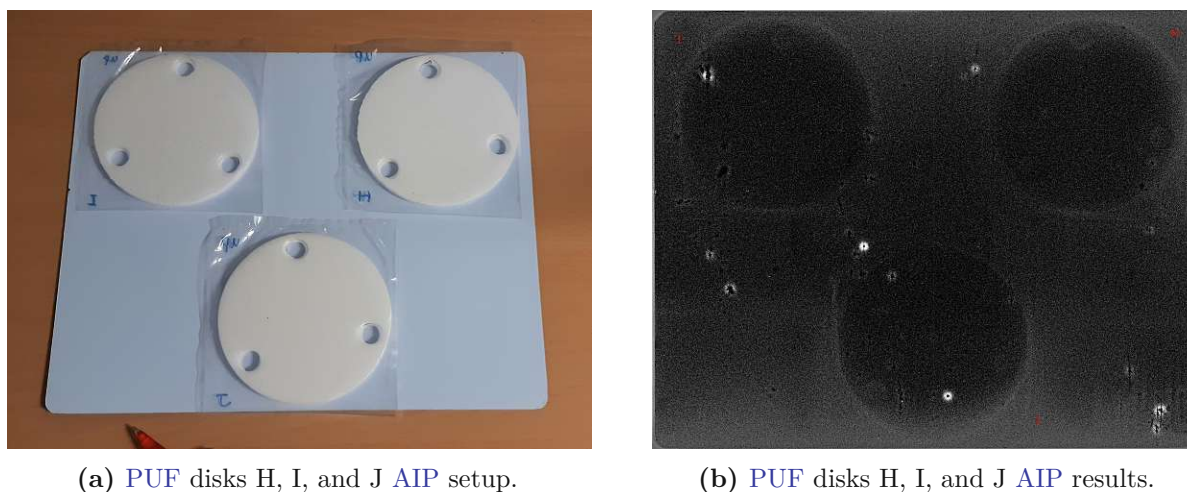
Figure 54: Setup and radiography results of the PUF disks D, E, and G after ≈ 11 weeks of exposure on an AIP.

3.2 Passive Air Samplers

All nine passive sampler PUF disks were put on AIPs for a long-term exposure of 2 - 3 months due to their overall low radioactivity, especially when compared to the Namie fleece coat. This was done to provide a reasonable starting point for the search of any hot particles since previous AIP exposures of the samplers were usually done for weeks as well. The disks were placed on the AIPs similar to the setups used for the Namie fleece sample, but this time only in groups of three due to space constraints, so three image plates were used in total.

In the end, the AIPs were exposed for 10 weeks and 5 days before they were evaluated. The results of all the exposures are shown in figures 53, 54, and 55. On the AIP images, there are a lot of hotspots visible that have nothing to do with the samplers themselves, this can be seen especially well for the sampler H, I, and J (Fig. 55). Only the hotspots that are located directly inside the contours of the PUF disks were further analyzed, everything around that was likely coming from the ambient environment and was only visible due to the prolonged AIP exposure.

Interestingly, there were three very bright spots inside the outline of the samplers: one on B (Fig. 53), one on G (Fig. 54), and one on J (Fig. 55). To gauge the radioactivity emitted by these hot particles, these disks underwent an incremental reduction in exposure time. This was mainly done to compare them to the Namie fleece sample, where the relation between AIP



(a) PUF disks H, I, and J AIP setup.

(b) PUF disks H, I, and J AIP results.

Figure 55: Setup and radiography results of the PUF disks H, I, and J after ≈ 11 weeks of exposure on an AIP.

hotspot size and activity detected in gamma spectrometry had already been well explored. Most samples from the fleece cloth that required 2 - 3 days of AIP exposure to be clearly visible, would only register just over the MDA of the gamma spectrometer, i.e., this was the main boundary for further analysis. The exposure time was reduced to ≈ 4 weeks, then ≈ 2 weeks and after this still over-exposed the hotspots, one last exposure of 2 days was made. This still over-exposed the particle on disk B and barely registered that on disk G. The disks H, I, and J were carefully repackaged to thinner plastic wrap between one of these steps, in order to shorten the exposure time even more, however unfortunately, the particle on disk J could not be located again after this. It was probably lost during the repacking process. The main focus was therefore put on the particle found on disk B. It was by far the most promising from all of the passive sampler PUF disks and its activity was on a reasonable level – this is where the following sample PS.B.P.1 originated from.

3.2.1 Sample PS.B.P.1

This sample was a large particle that was found directly on the surface of passive sampler disk B inside the region of the hotspot on the AIP image. It was therefore in accordance with the naming scheme used for the Namie coat samples labeled "Passive Sampler B Particle 1". The particle could then be simply picked up from the surface using tweezers, photos of it are shown in figure 56. It resembles a small grain of dirt or similar material. An additional AIP exposure of the particle only confirmed that this was indeed the origin of the bright hotspot. Before taking it to the USTEM, gamma spectrometric measurements of the particle were made. 0.151 ± 0.018 Bq of ^{137}Cs were detected, calculated back to the time of the accident (24 h measurement period, 1.960σ).

Upon placing the grain of dirt on the sample holder of the FIB SEM it crumbled. All of the debris was spread on the surface of the holder to make it easier to search for hot particles. An overview image of this is shown in figure 57. Most of what can be seen are smaller, irregular particles of dirt of various different sizes, but there are also a few fibers in the material. This sample was searched twice on two separate occasions at the USTEM, just because of the sheer complexity of the dirt debris. Only very few round(-ish) particles could be found. Other than this, most of them were jagged in appearance. Regarding the elemental composition, most of the material contained mainly of C and O, of course. However, generally, most regions also had good trace amounts of Al and Si ($\approx 2 - 5\%$). Some regions also exhibited traces of Ti, and there were a couple of salty particles with high contents of Na, Mg, and Cl.

The first of two particles that was identified to be promising and needed to be extracted was



(a) Photo of the passive sampler disk with the particle inside the AIP hotspot region highlighted in red.



(b) Photo of the large particle through an optical microscope at low magnification.

Figure 56: Photos of the large particle that was found directly on the surface of passive air sampler PUF disk B, registering significantly on the AIP.

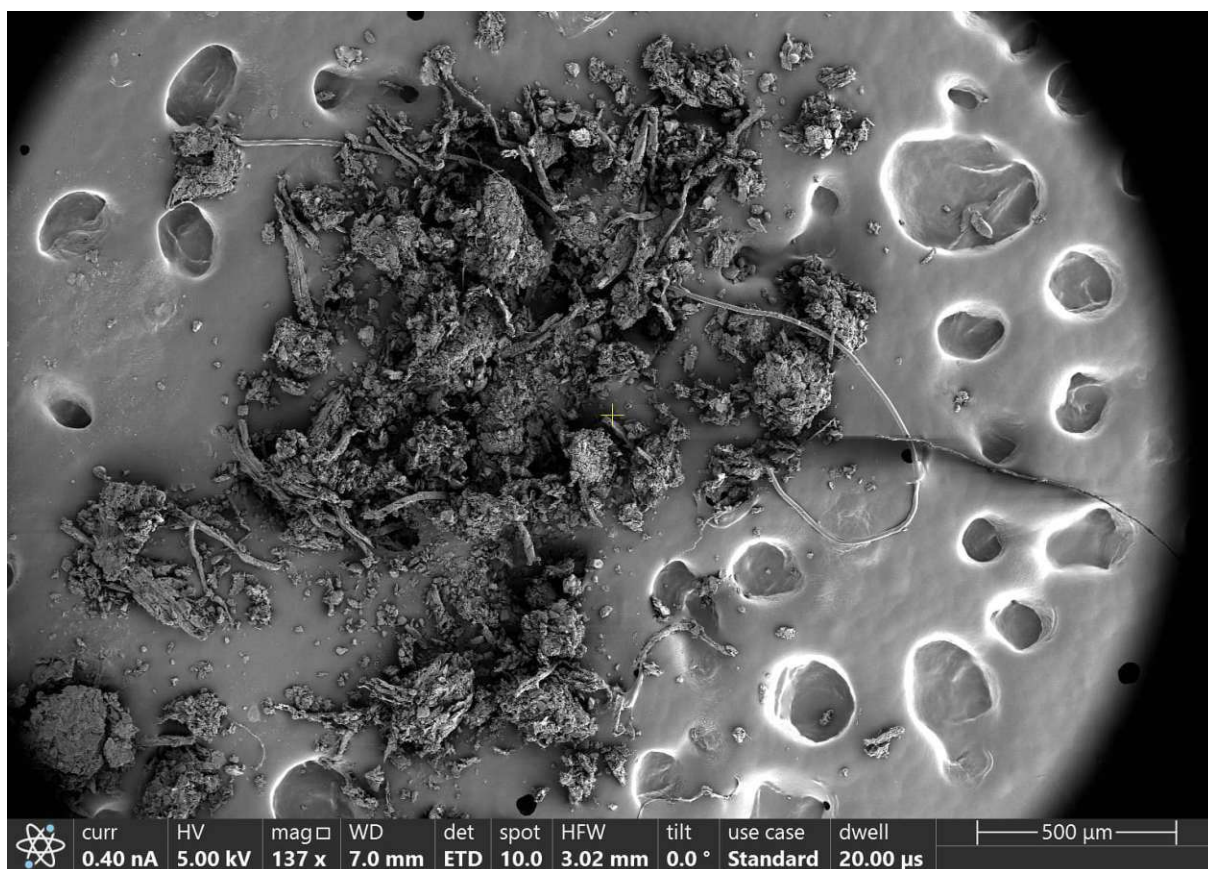


Figure 57: Overview image of sample PS.B.P.1.

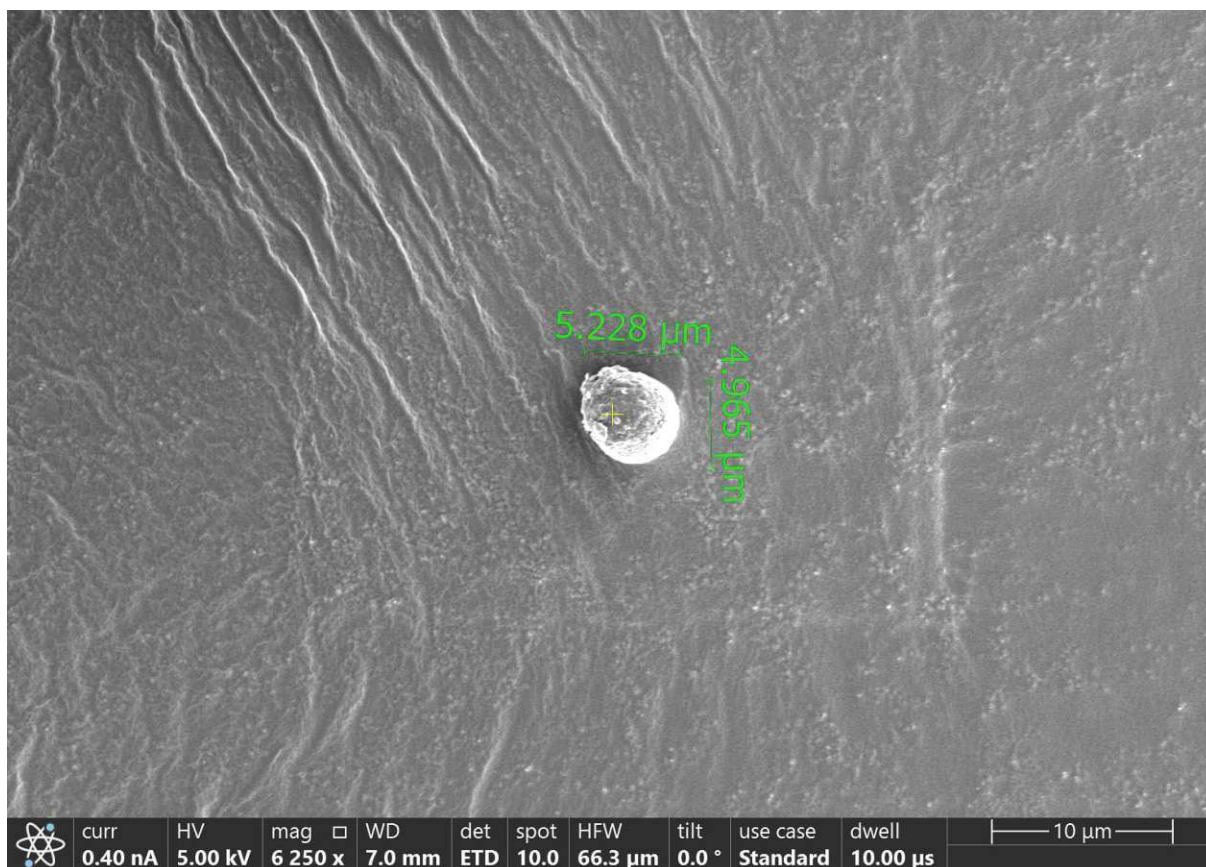


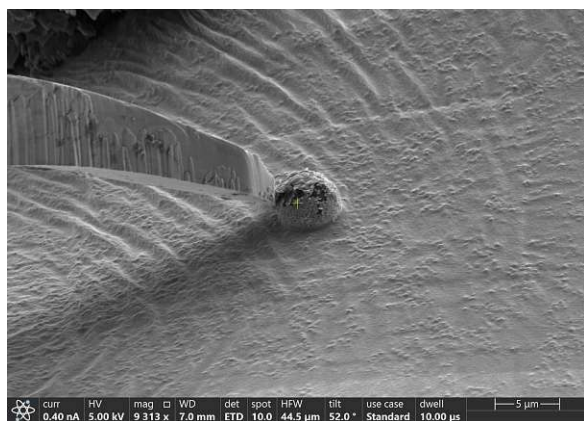
Figure 58: Image of the first spherical particle that was found in the dirt particle debris. This approximately 5 μm large particle was a potential CsMP-candidate due to its shape, size, and elemental composition.

Table 12: Elemental composition of the first spherical particle shown in figure 58, obtained by EDX. C and O are likely over-represented to a slight, but uncertain degree due to the penetration depth of the electron beam and the small diameter of the particle. Pd and Au stem from the sputtering process.

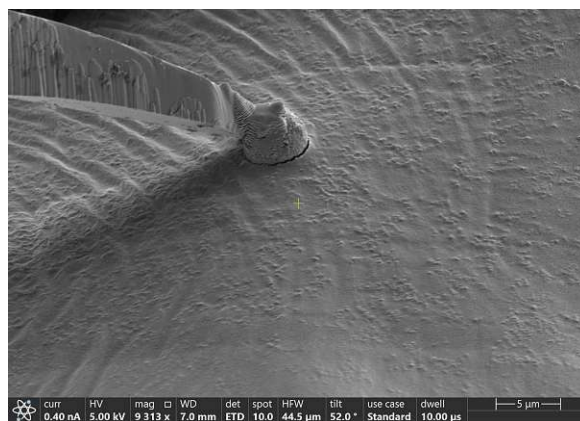
Element	Mass %	Mass % Error	Atomic %	Atomic % Error
C K	2.1	± 0.1	13.6	± 0.3
O K	5.0	± 0.2	24.4	± 1.1
Al K	0.9	± 0.1	2.7	± 0.4
Si K	3.7	± 0.2	10.5	± 0.5
Pd L	40.0	± 2.1	29.6	± 1.6
Au M	48.2	± 1.6	19.2	± 0.6

found a bit outside of the main field of debris, directly on the glue of the sample holder. It was approximately 5 μm in diameter and spherical – an image of it is shown in figure 58. Regarding the elemental composition, the results of the EDX are shown in table 12. The particle consisted mostly of C, O, and Si, as well as large amounts (atomic %) of Pd and Au from the sputtering process. This high Si content together with traces of Al and its morphology made the particle a potential CsMP.

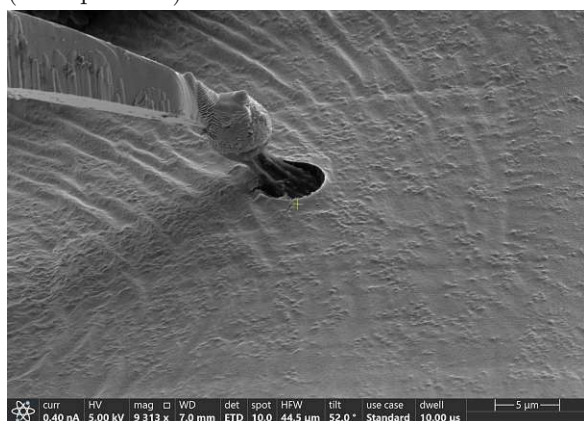
The extraction process was uncomplicated due to the fact that the sample was far away from any other debris and it just sat on the sample holder's surface. Some images from the process are shown in figure 59. After this, the Cu lift-out grid with this new particle was, once again, put



(a) Particle with extraction needle before welding (W deposition).



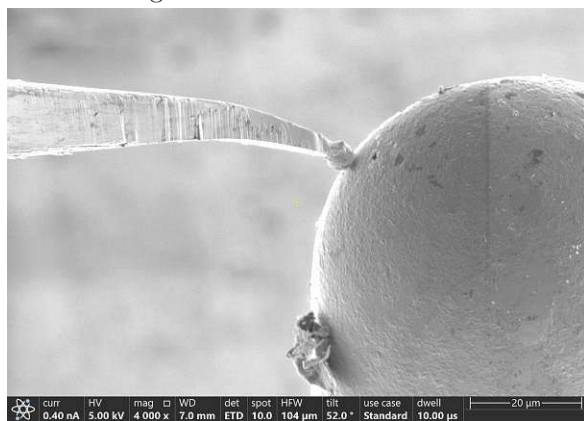
(b) Particle after being welded to the needle tip.



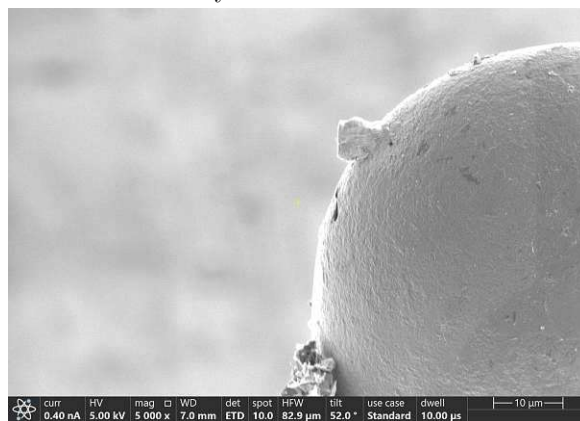
(c) Needle is being lifted off the sample holder with some of the glue still stuck to it.



(d) Needle and particle have lifted off and are now able to move freely.

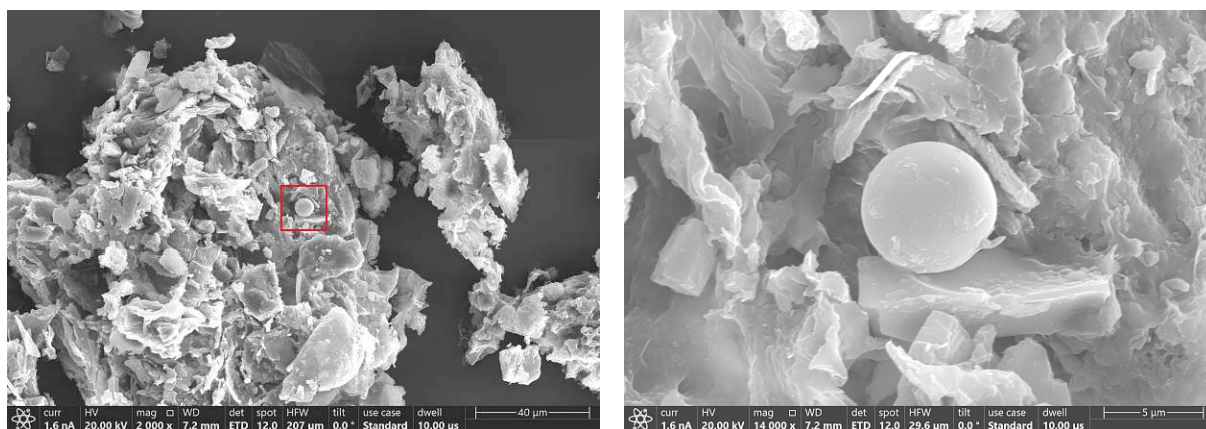


(e) Particle is being positioned to the lift-out grid finger before welding.



(f) Particle fixated to the lift-out grid finger, cut free from the needle tip.

Figure 59: Extraction process of the first spherical particle obtained from the passive sampler PUF. Note how the glue of the sample holder behaves upon lift-off: it keeps sticking to the particle and elongates until it breaks apart, but after this, the residue does not retract back into the sample holder surface, instead it stays straightened up.



(a) Large-scale overview image of the second spherical particle and the surrounding debris.

(b) Zoomed view of the second perfectly spherical particle.

Figure 60: Images of the second spherical particle that was found in the dirt particle debris. This approximately $6.8\ \mu\text{m}$ large particle was a potential CsMP-candidate due to its shape, size, and elemental composition.

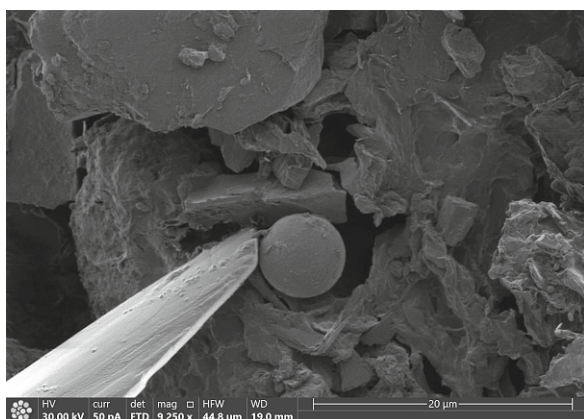
on the gamma spectrometer at the ATI like all of the other samples before it. The device was unable to identify any radioactivity from the sample whatsoever over the 149 h measurement period. Taking into account the limits of the device (ISO 11929), with an MDA of 1.3×10^{-2} Bq and a decision level of 6.4×10^{-3} Bq, the confidence interval lower limit was placed at 7.9×10^{-5} Bq and upper limit at 7.2×10^{-3} Bq (5% confidence level). The weighted mean activity was actually computed to be negative due to background subtraction.

The second, and also the last microparticle that was found and extracted, was also probably the most promising of them all. Overview images of it are shown in figure 60. It is perfectly spherical with a diameter of around $6.8\ \mu\text{m}$ and sits directly in the field of debris from the dirt particle. The EDX data also looked very promising with large contents of Si and O, as well as Al and traces of Fe. This microparticle was the one with the highest Si contents of all the microparticles researched both in mass % and atomic %. The results of the EDX measurement is shown in table 13. The particle was only found on the second search through this sample, despite its distinct morphology, but it did not set itself apart much from all of the background debris, especially to the left of it (see Fig. 60a).

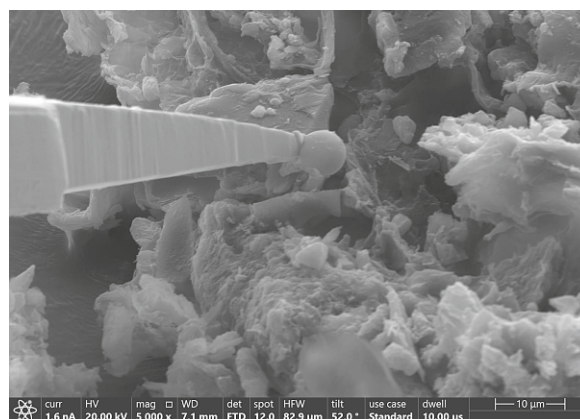
The extraction was straightforward in this case and completed flawlessly. The needle was placed next to the microparticle on a side that had less debris in its way and then the usual process took place. This has been documented on some images as well, see figure 61. The obtained lift-out grid with the fixated particle has been put on the gamma spectrometer with another microparticle extracted from the Namie fleece coat sample (see section 3.1.5), which has been described previously in that section. The same results there are true for this particle too: After a 114 h long measurement, no ^{137}Cs could be identified. Taking into account the detection limits (ISO 11929), with an MDA of 1.5×10^{-2} Bq and a decision level of 7.4×10^{-3} Bq, the confidence interval lower limit was placed at 1.4×10^{-4} Bq and upper limit at 1.0×10^{-2} Bq (5% confidence level). The weighted mean activity lies significantly below the decision level for the spectrometer.

Table 13: Elemental composition of the second spherical particle shown in figure 60, obtained by EDX. C and O are likely over-represented to a slight, but uncertain degree due to the penetration depth of the electron beam and the small diameter of the particle. Pd and Au stem from the sputtering process.

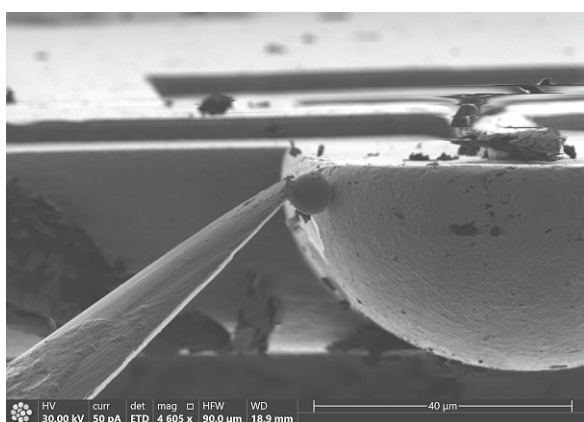
Element	Mass %	Mass % Error	Atomic %	Atomic % Error
C K	7.9	±0.1	13.9	±0.2
O K	42.5	±0.3	56.1	±0.4
Na K	1.0	±0.0	0.9	±0.0
Mg K	0.5	±0.0	0.4	±0.0
Al K	7.6	±0.1	6.0	±0.0
Si K	26.3	±0.1	19.8	±0.1
K K	0.7	±0.0	0.4	±0.0
Ca K	0.4	±0.0	0.2	±0.0
Ti K	0.2	±0.0	0.1	±0.0
Fe K	1.6	±0.1	0.6	±0.0
Cu K	0.3	±0.1	0.1	±0.0
Pd L	3.6	±0.1	0.7	±0.0
Au L	7.3	±0.6	0.8	±0.1



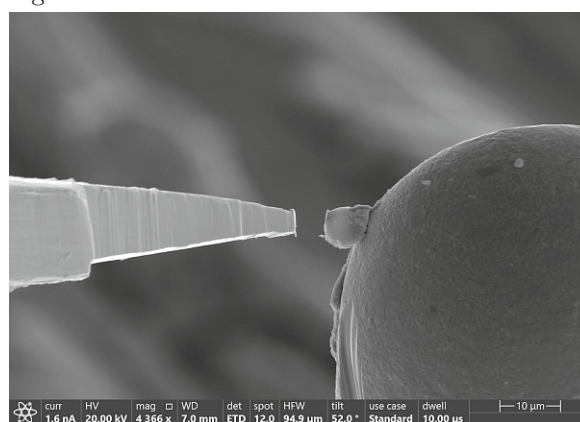
(a) Particle next to the needle before welding.



(b) Particle picked up with the needle after welding.



(c) Needle with particle next to the Cu lift-out grid before welding.



(d) Particle fixated to the lift-out grid with connection to the needle cut.

Figure 61: Extraction process of the second spherical particle that was obtained from inside the field of debris on the passive sampler disk.

4 Conclusion

Radioactive microparticles play a big role in the dispersion of fallout from all kinds of nuclear sources, be it nuclear weapons tests, nuclear power plant accidents, or other incidents in similar facilities of the nuclear industrial complex. They can be a great asset in nuclear forensics due to their unique properties that highly depend on the type of release, the formation and release scenario itself, the included radioisotopes, and the subsequent dispersion into the environment. On the civilian side of nuclear power, they have played an especially large role in the investigations of the Chornobyl (1986) and the Fukushima Daiichi Nuclear Power Plant (FDNPP) (2011) accidents. In the case of FDNPP, a novel type of microparticle has been discovered after the hydrogen explosions in several units of the power plant: glassy, mostly spherical microparticles rich in the radiocaesium isotopes ^{134}Cs and ^{137}Cs . These so-called **caesium microparticles (CsMPs)** are thought to have formed during the hydrogen explosions that occurred in the **reactor buildings (RBs)** of the site, mainly due to the interaction of the **high-efficiency particulate air (HEPA)** and **pre-HEPA** filters with the extreme heat from the explosions and the prior releases of radiocaesium from the **reactor pressure vessels (RPVs)**. These hot particles are also a good indicator of the unit of origin at FDNPP, which makes it possible to investigate the events that occurred before, during, and shortly after the hydrogen explosions in the respective unit. One indicator is of special importance in this regard – the $^{134}\text{Cs}/^{137}\text{Cs}$ ratio. It corresponds to the specific unit of origin fairly well, so by measuring only these two radioisotopes, it is possible to pinpoint the location of formation of each particle. The particle's size, morphology, and any other special characteristics can then be used to research the formation mechanisms.

One challenge associated with these CsMPs is the fact that they come in very different shapes and sizes. That is why previous studies established a system to categorize them by their characteristics and assigning them letters depending on the type, i.e., category, starting with Type A (the first identified type of CsMP), up to Type E particles (the most recent findings). Most of those found to date are either rounded in shape or spherical, which hints at the prevalent formation mechanism of melting and atomization of the HEPA mineral fibers during the explosions in the RBs. They can also be challenging to identify in environmental samples due to their small size. The fact that the accident occurred well over 13 years ago poses another difficulty in search for CsMPs – after all more than half of the total radiocaesium activity has already decayed attributing mostly to the short-lived isotope ^{134}Cs .

In order to research the distribution and behavior of CsMPs, two types of samples have been analyzed in this thesis. The first one was a piece of a common fleece coat that was located inside a house inside the difficult-to-return zone, completely untouched for years after the accident. This piece was contaminated with a well-measurable amount of both ^{134}Cs and ^{137}Cs , despite it being hung on a coat hanger inside the locked building. The other type of sample was a novel passive air sampler that was specifically engineered to capture aerosols with special regards to trap radioactive particles that might be resuspended in the environment. A passive air sampler consisting of ten **polyurethane foam (PUF)** disks, had been positioned in the area surrounding FDNPP years after the accident, and still were able to capture some radioactive material from the air.

These samples were investigated using a standard approach of fractionation together with **autoradiographic imaging plates (AIPs)**, with the main focus being the fleece coat sample due to the overall higher activity. Gamma spectroscopy was utilized to quantify the activity of the fractionated samples, as well as to determine the isotopic composition. With <1 Bq, calculated back to the time of the FDNPP accident, the activity of all fractionated samples was quite low, making it impossible to measure any amounts of ^{134}Cs in an effort to determine the $^{134}\text{Cs}/^{137}\text{Cs}$ ratios of the individual particles. Despite that, most of these samples registered quite well on 1 - 2 day long AIP exposures, this is especially true for all of the fleece coat samples and 3 of the 9 passive air sampler disks. The other 6 disks, unfortunately, had to be exposed for longer durations, mostly weeks, in order to make some hotspots visible. This already made it highly unlikely that any detection of radiocaesium in the subsequently extracted particles would be

possible, especially since it would require an exceedingly time-intensive process to isolate these weak hotspots on top of this.

In total, 106 samples were produced by the fractionation process (see Fig. 33) of the fleece coat sample. From these 106 analyzed fleece samples, the best five made it to the next step together with one very promising particle collected from the surface of one of the passive air sampler PUF disks. The six samples were analyzed using a scanning electron microscope (SEM) at the University Service Facility for Transmission Electron Microscopy (USTEM) on multiple separate occasions and searched for potential CsMPs on the basis of shape and size, i.e., the known morphologies that have been established in previous studies. This process turned out to be quite challenging and time-intensive in itself, because the samples had to be investigated in great detail, due to the large number of other irrelevant microparticles and the large size of most of the samples compared to the small scale of the typical CsMP. When a candidate particle had been identified, energy-dispersive X-ray spectroscopy (EDX) was used to determine the elemental composition, which is a crucial indicator for the presence of a CsMP. The main focus was placed on the search for Si-rich particles, with importance on Al, Ca, Ti, Fe, and Zn as well. If the EDX results were satisfactory, then the particle was carefully extracted using the focused ion beam (FIB) SEM and fixated on a copper lift-out grid that was taken back to the Atominstitut (ATI) for gamma spectrometric measurements.

This way, a total of 5 potential CsMPs could be extracted. Each of them was placed on the detector to confirm or deny the presence of the required radiocaesium, most likely only ^{137}Cs anyways, due to the relatively short half-life of ^{134}Cs . In the end, no conclusive evidence for the presence of radiocaesium in any of the five extracted particles could be found using the ultra-low-level gamma spectrometry setup at the ATI. After this, all five lift-out grids with the microparticles were directly placed on an AIP with no material in between and exposed for 24 h to rule out the possibility of a presence of pure α - or β -emitters. On top of that, this took advantage of the higher efficiency of the AIP. No conclusive results were achieved using this method, so it is highly likely that no radioactive particles were extracted from any of the samples, despite their promising morphology and elemental composition.

In the future, more efficient methods to isolate hotspots on the AIP images and particles in the SEM examinations are going to be a great improvement to accelerate the entire process. AIPs will probably still be a key tool in the search for radioactive microparticles, due to their spatial resolution and high efficiency for beta radiation, as well as their ability to parallelize exposures for multiple samples at a time. The largest constraint by far is the time needed to do all these tasks, especially since devices like the FIB SEM require lengthy lead times. To help this, it might be worth to decrease the size of the samples even more in order to facilitate and accelerate the search during SEM imaging. It might have also been helpful to cut larger sections of the fleece to cover more potential CsMPs and then restrict processing even more, to only allow the very best ones to continue down the extraction chain. Instead of cutting the fleece coat samples in the centers, it would have been better to somehow slice them into thin disks. Though significantly harder to do, this would have significantly helped with the self-absorption issues that were encountered and prevented the need to expose most of the samples twice.

Interestingly, no particles fitting the characteristics of a CsMP with a diameter of $\geq 10\ \mu\text{m}$ was found. Now, this might be either due to the simple fact that none were present on the samples in the first place. It might have also been due to the fact that these particles are more easily disturbed and flaked off of the bulk samples. This is unlikely, however, because the loss in radioactivity would have been noticed during the AIP exposures in between the sample cutting steps. In the end, one can only speculate what makes up the bulk of the radioactive hotspots on the fleece coat sample, it probably either is in the form of microparticles $\leq 10\ \mu\text{m}$, likely $\lesssim 1\ \mu\text{m}$ in diameter, or the particles feature a much more complex morphology than anticipated and were not recognized as such. Regarding the passive air sampler, it might be possible that the wrong particle properties were taken into account. Due to the fact that the samplers only trap aerosols that were resuspended years after the original fallout, these might be quite different

from the spherical particles of the initial fallout. It is possible that these might be, in fact, much more irregular and edged because of years of weathering. In addition to this, the fact that the sampler was designed to trap only coarse particles makes it unlikely that a large number of small microparticles as previously expected was deposited.

Either way, this thesis offers a potential starting point for the future investigation of the samples discussed, with an outline of the workflow, the necessary procedures, and the commonly encountered microparticles. Importance was also placed on the larger understanding of the [FDNPP](#) accident, hot particles in general, and a thorough overview of the state of the research on [CsMPs](#), with their associated formation mechanisms, tying all of this together. Special emphasis is placed on the fleece coat sample, where only a single, literal corner was cut for analysis to conserve as much as possible. This provides future research with more than enough material to repeat and improve upon all of the methods used in this work. It is possible that searching different sections of the fleece with improved versions of the processes proposed here will be able to reveal more about the nature of the contamination and [CsMPs](#) in general.

References

- [1] International Atomic Energy Agency. *The Fukushima Daiichi Accident*. Non-serial Publications. International Atomic Energy Agency, Vienna, 2015.
- [2] Tokyo Electric Power Co., TEPCO; IAEA Imagebank. Fukushima Daichi Nuclear Power Station. (Fukushima, Japan). https://www.flickr.com/photos/iaea_imagebank/8388174045/, 2007. Accessed: 2024-09-16.
- [3] Tokyo Electric Power Co., TEPCO. Overview of facility of Fukushima Daiichi Nuclear Power Station. https://www.tepco.co.jp/en/nu/fukushima-np/outline_f1/index-e.html. Accessed: 2024-09-17.
- [4] NOAA: National Centers for Environmental Information. On This Day: 2011 Tohoku Earthquake and Tsunami. <https://www.ncei.noaa.gov/news/day-2011-japan-earthquake-and-tsunami>. Accessed: 2024-09-18.
- [5] Tokyo Electric Power Company, TEPCO. Roadmap towards Restoration from the Accident at Fukushima Daiichi Nuclear Power Station. https://web.archive.org/web/20110524023705/https://www.meti.go.jp/english/speeches/pdf/20110417_a.pdf, Apr 2011. Accessed: 2024-10-29.
- [6] Tokyo Electric Power Company, TEPCO. Roadmap towards Restoration from the Accident at Fukushima Daiichi Nuclear Power Station. https://www.tepco.co.jp/en/press/corp-com/release/betu11_e/images/110417e12.pdf, Apr 2011. Accessed: 2024-10-29.
- [7] Tokyo Electric Power Company, TEPCO. Roadmap on the Way to Decommissioning. <https://www.tepco.co.jp/en/hd/decommission/project/roadmap/index-e.html>. Accessed: 2024-10-29.
- [8] M. C. Honda, T. Aono, M. Aoyama, Y. Hamajima, H. Kawakami, M. Kitamura, Y. Masumoto, Y. Miyazawa, M. Takigawa, and T. Saino. Dispersion of artificial caesium-134 and -137 in the western north pacific one month after the fukushima accident. *Geochemical Journal*, 46(1):e1–e9, 2012.
- [9] International Atomic Energy Agency. *Environmental Transfer of Radionuclides in Japan following the Accident at the Fukushima Daiichi Nuclear Power Plant*. Number 1927 in TECDOC Series. International Atomic Energy Agency, Vienna, 2020.
- [10] H. Hoshi, M. Hirano, M. Iijima, and T. Homma. Severe accident analyses of fukushima-daiichi units 1 to 3. In *Side event by Government of Japan at 56th IAEA General Conference*. Vienna, Austria, volume 17, 2012.
- [11] Government of Japan. Additional report of the japanese government to the iaea-the accident at tepco's fukushima nuclear power stations. https://web.archive.org/web/20111204083554/http://www.meti.go.jp/english/earthquake/nuclear/iaea/iaea_110911.html, 2011. Accessed: 2024-10-30.
- [12] Nuclear NISA et al. Regarding the evaluation of the conditions on reactor cores of unit 1, 2 and 3 related to the accident at fukushima daiichi nuclear power station. <https://web.archive.org/web/20130218191741/http://www.nsr.go.jp/archive/nisa/english/press/2011/06/en20110615-5.pdf>, 2011. Accessed: 2024-10-30.
- [13] Institut de radioprotection et de surete nucleaire – IRSN. Fukushima, one year later initial analyses of the accident and its consequences. Technical report, Institut de radioprotection et de surete nucleaire-IRSN, France, March 2012.

- [14] M. Anne, I. Korsakissok, D. Quélo, J. Groëll, M. Tombette, D. Didier, E. Quentric, O. Saunier, J.-P. Benoit, and O. Isnard. Atmospheric Dispersion and Deposition of Radionuclides from the Fukushima Daiichi Nuclear Power Plant Accident. *Elements*, 8(3):195–200, 06 2012.
- [15] M. Anne, I. Korsakissok, D. Quélo, O. Saunier, J. Groëll, D. Didier, D. Corbin, J. Denis, M. Tombette, V. Winiarek, M. Bocquet, E. Quentric, and J.-P. Benoit. État de la modélisation pour simuler l'accident nucléaire de la centrale Fukushima Daiichi. *Pollution Atmosphérique : climat, santé, société*, March 2013.
- [16] K. G. Rubinshtein, E. M. Nabokova, R. Yu. Ignatov, M. M. Smirnova, R. V. Arutyunyan, V. N. Semenov, O. S. Sorokovikova, A. V. Fokin, D. A. Pripachkin, and D. V. Dzama. Software package of atmospheric radionuclide distribution models and its use for assessing the radiation conditions after the fukushima dai-ichi nuclear power plant accident. *Russian Meteorology and Hydrology*, 37(9):586–597, Sep 2012.
- [17] R. V. Arutyunyan, L. A. Bolshov, D. A. Pripachkin, V. N. Semyonov, O. S. Sorokovikova, A. L. Fokin, K. G. Rubinstein, R. Yu. Ignatov, and M. M. Smirnova. Estimation of radionuclide emission during the march 15, 2011 accident at the fukushima-1 npp (japan). *Atomic Energy*, 112(3):188–193, Jul 2012.
- [18] K. S. Dolganov, A. V. Kapustin, A. E. Kisselev, D. Yu. Tomashchik, S. V. Tsaun, and T. A. Yudina. Real-time calculation of the accident at the fukushima-1 npp (japan) using the sokrat code. *Atomic Energy*, 114(3):161–168, Jul 2013.
- [19] International Atomic Energy Agency. *Environmental Consequences of the Chernobyl Accident and their Remediation: Twenty Years of Experience*. Number 8 in Radiological Assessment Reports Series. International Atomic Energy Agency, Vienna, 2006.
- [20] J. E. Ten Hoeve and M. Z. Jacobson. Worldwide health effects of the fukushima daiichi nuclear accident. *Energy Environ. Sci.*, 5:8743–8757, 2012.
- [21] A. Hasegawa, K. Tanigawa, A. Ohtsuru, H. Yabe, M. Maeda, J. Shigemura, T. Ohira, T. Tominaga, M. Akashi, N. Hirohashi, T. Ishikawa, K. Kamiya, K. Shibuya, S. Yamashita, and R. K. Chhem. Health effects of radiation and other health problems in the aftermath of nuclear accidents, with an emphasis on fukushima. *The Lancet*, 386(9992):479–488, 2015.
- [22] S. Yasumura, M. Hosoya, S. Yamashita, K. Kamiya, M. Abe, M. Akashi, K. Kodama, and K. Ozasa. Study protocol for the fukushima health management survey. *Journal of Epidemiology*, 22(5):375–383, 2012.
- [23] International Atomic Energy Agency. *Radioactive Particles in the Environment: Sources, Particle Characterization and Analytical Techniques*. Number 1663 in TECDOC Series. International Atomic Energy Agency, Vienna, 2011.
- [24] G. Steinhauser. Anthropogenic radioactive particles in the environment. *Journal of Radio-analytical and Nuclear Chemistry*, 318:1629–1639, 2018.
- [25] B. Salbu, V. Kashparov, O. C. Lind, R. Garcia-Tenorio, M. P. Johansen, D. P. Child, P. Roos, and C. Sancho. Challenges associated with the behaviour of radioactive particles in the environment. *Journal of Environmental Radioactivity*, 186:101–115, 2018. II International Conference on Radioecological Concentration Processes (50 years later).
- [26] C. Papastefanou. Escaping radioactivity from coal-fired power plants (cpps) due to coal burning and the associated hazards: a review. *Journal of Environmental Radioactivity*, 101(3):191–200, 2010.

- [27] K. Bunzl. Probability for detecting hot particles in environmental samples by sample splitting. *Analyst*, 122:653–656, 1997.
- [28] P. Dale, I. Robertson, and M. Toner. Radioactive particles in dose assessments. *Journal of Environmental Radioactivity*, 99(10):1589–1595, 2008. Natural Radiation.
- [29] E.A. Caffrey, M.P. Johansen, and K.A. Higley. Voxel modeling of rabbits for use in radiological dose rate calculations. *Journal of Environmental Radioactivity*, 151:480–486, 2016. Special Issue: ICRER Barcelona 2014.
- [30] A.M. Kabdyrakova, S.N. Lukashenko, A.T. Mendubaev, A.Ye. Kunduzbayeva, A.V. Panitskiy, and N.V. Larionova. Distribution of artificial radionuclides in particle-size fractions of soil on fallout plumes of nuclear explosions. *Journal of Environmental Radioactivity*, 186:45–53, 2018. II International Conference on Radioecological Concentration Processes (50 years later).
- [31] G.R. Crocker, J.D. O'Connor, and E.C. Freiling. Physical and radiochemical properties of fallout particles. *Health Physics*, 12(8):1099 – 1104, 1966. Cited by: 24; All Open Access, Green Open Access.
- [32] A.B. Kersting, D.W. Efurud, D.L. Finnegan, D.J. Rokop, D.K. Smith, and J.L. Thompson. Migration of plutonium in ground water at the nevada test site. *Nature*, 397(6714):56 – 59, 1999. Cited by: 824.
- [33] G. Steinhauser, A. Brandl, and T. E. Johnson. Comparison of the chernobyl and fukushima nuclear accidents: A review of the environmental impacts. *Science of The Total Environment*, 470-471:800–817, 2014.
- [34] F. Stäger, D. Zok, A.-K. Schiller, B. Feng, and G. Steinhauser. Disproportionately high contributions of 60 year old weapons-137cs explain the persistence of radioactive contamination in bavarian wild boars. *Environmental Science & Technology*, 57(36):13601–13611, 2023. Pmid: 37646445.
- [35] V. Kashparov, V. Yoschenko, S. Levchuk, D. Bugai, N. Van Meir, C. Simonucci, and A. Martin-Garin. Radionuclide migration in the experimental polygon of the red forest waste site in the chernobyl zone – part 1: Characterization of the waste trench, fuel particle transformation processes in soils, biogenic fluxes and effects on biota. *Applied Geochemistry*, 27(7):1348–1358, 2012. 25 years after the Chernobyl power plant explosion: Management of nuclear wastes and radionuclide transfer in the environment.
- [36] M. Zhurba, V. Kashparov, N. Ahamdach, B. Salbu, V. Yoschenko, and S. Levchuk. The “hot particles” data base. In Deborah H. Oughton and Valery Kashparov, editors, *Radioactive Particles in the Environment*, pages 187–195, Dordrecht, 2009. Springer Netherlands.
- [37] A. Sakaguchi, P. Steier, Y. Takahashi, and M. Yamamoto. Isotopic compositions of ²³⁶u and pu isotopes in “black substances” collected from roadsides in fukushima prefecture: Fallout from the fukushima dai-ichi nuclear power plant accident. *Environmental Science & Technology*, 48(7):3691–3697, 2014. Pmid: 24601520.
- [38] Y. Miyamoto, K. Yasuda, and M. Magara. Size distribution of radioactive particles collected at tokai, japan 6 days after the nuclear accident. *Journal of Environmental Radioactivity*, 132:1–7, 2014.
- [39] K. Adachi, Mizuo Kajino, Yuji Zaizen, and Yasuhito Igarashi. Emission of spherical cesium-bearing particles from an early stage of the fukushima nuclear accident. *Scientific reports*, 3:2554, 08 2013.

- [40] M. Chino, H. Terada, H. Nagai, G. Katata, S. Mikami, T. Torii, K. Saito, and Y. Nishizawa. Utilization of $^{134}\text{Cs}/^{137}\text{Cs}$ in the environment to identify the reactor units that caused atmospheric releases during the fukushima daiichi accident. *Scientific Reports*, 6(1):31376, Aug 2016.
- [41] A.C. Chamberlain. Environmental impact of particles emitted from windscale piles, 1954–1957. *Science of The Total Environment*, 63:139–160, 1987.
- [42] A.J. Cresswell and D.C.W. Sanderson. Evaluating airborne and ground based gamma spectrometry methods for detecting particulate radioactivity in the environment: A case study of irish sea beaches. *Science of The Total Environment*, 437:285–296, 2012.
- [43] A. Bolsunovsky, M. Melgunov, A. Chuguevsky, O. C. Lind, and B. Salbu. Unique diversity of radioactive particles found in the yenisei river floodplain. *Scientific Reports*, 7, 12 2017.
- [44] Y.M. Amin, Mayeen Uddin Khandaker, A.K.S. Shyen, R.H. Mahat, R.M. Nor, and D.A. Bradley. Radionuclide emissions from a coal-fired power plant. *Applied Radiation and Isotopes*, 80:109–116, 2013.
- [45] A. Hidaka. Origin of cs-bearing silicate glass microparticles observed during fukushima accident and recommendations on nuclear safety. *Journal of Radioanalytical and Nuclear Chemistry*, 332(6):1607–1623, Jun 2023.
- [46] Y. Igarashi, T. Kogure, Y. Kurihara, H. Miura, T. Okumura, Y. Satou, Y. Takahashi, and N. Yamaguchi. A review of cs-bearing microparticles in the environment emitted by the fukushima dai-ichi nuclear power plant accident. *Journal of Environmental Radioactivity*, 205-206:101–118, 2019.
- [47] T. Ono, Y. Iizawa, Y. Abe, I. Nakai, Y. Terada, Y. Satou, K. Sueki, K. Adachi, and Y. Igarashi. Investigation of the chemical characteristics of individual radioactive microparticles emitted from reactor 1 by the fukushima daiichi nuclear power plant accident by using multiple synchrotron radiation x-ray analyses (**in Japanese**). *Bunseki Kagaku*, 66(4):251–261, 2017.
- [48] N. Yamaguchi, T. Kogure, H. Mukai, K. Akiyama-Hasegawa, M. Mitome, T. Hara, and H. Fujiwara. Structures of radioactive cs-bearing microparticles in non-spherical forms collected in fukushima. *Geochemical Journal*, 52:123–136, 03 2018.
- [49] Y. Satou, K. Sueki, K. Sasa, H. Yoshikawa, S. Nakama, H. Minowa, Y. Abe, I. Nakai, T. Ono, K. Adachi, and Y. Igarashi. Analysis of two forms of radioactive particles emitted during the early stages of the fukushima dai-ichi nuclear power station accident. *Geochemical Journal*, 52(2):137–143, 2018.
- [50] Z. Zhang, J. Igarashi, Y. Satou, K. Ninomiya, K. Sueki, and A. Shinohara. Activity of ^{90}Sr in fallout particles collected in the difficult-to-return zone around the fukushima daiichi nuclear power plant. *Environmental Science & Technology*, 53(10):5868–5876, 2019. Pmid: 31034221.
- [51] K. Morooka, E. Kurihara, M. Takehara, R. Takami, K. Fueda, K. Horie, M. Takehara, S. Yamasaki, T. Ohnuki, B. Grambow, G. T. W. Law, J. W. L. Ang, W. R. Bower, J. Parker, R. C. Ewing, and S. Utsunomiya. New highly radioactive particles derived from fukushima daiichi reactor unit 1: Properties and environmental impacts. *Science of The Total Environment*, 773:145639, 2021.
- [52] Z. Macsik, L. A. Hudston, K. N. Wurth, D. Meininger, C. Jesinghaus, T. J. Tenner, B. E. Naes, M. Boswell, K. Shozugawa, S. P. LaMont, R. E. Steiner, and G. Steinhauser. Identification, isolation, and characterization of a novel type of fukushima-derived microparticle. *Journal of Radioanalytical and Nuclear Chemistry*, 331(12):5333–5341, Dec 2022.

- [53] G. Furuki, J. Imoto, A. Ochiai, S. Yamasaki, K. Nanba, T. Ohnuki, B. Grambow, R. C. Ewing, and S. Utsunomiya. Caesium-rich micro-particles: A window into the meltdown events at the fukushima daiichi nuclear power plant. *Scientific Reports*, 7(1):42731, Feb 2017.
- [54] K. Fueda, T. Komiya, K. Minomo, K. Horie, M. Takehara, S. Yamasaki, H. Shiotsu, T. Ohnuki, B. Grambow, G. T. W. Law, R. C. Ewing, and S. Utsunomiya. Occurrence of radioactive cesium-rich micro-particles (csmgs) in a school building located 2.8 km south-west of the fukushima daiichi nuclear power plant. *Chemosphere*, 328:138566, 2023.
- [55] Y. Sanada and T. Torii. Aerial radiation monitoring around the fukushima dai-ichi nuclear power plant using an unmanned helicopter. *Journal of Environmental Radioactivity*, 139:294–299, 2015.
- [56] National Center for Biotechnology Information. PubChem Compound Summary for CID 24261, Silicon Dioxide. <https://pubchem.ncbi.nlm.nih.gov/compound/Silicon-Dioxide>. Accessed: 2024-09-30.
- [57] H. Hagiwara, K. Kondo, and A. Hidaka. The formation mechanism of radiocesium-bearing microparticles derived from the fukushima daiichi nuclear power plant using electron microscopy. *Journal of Radioanalytical and Nuclear Chemistry*, 331(12):5905–5914, Dec 2022.
- [58] NRA (Nuclear Regulation Authority). Review meeting of analysis for Fukushima Daiichi nuclear power plant accident (in Japanese). <https://www.nra.go.jp/data/000345034.pdf>, 2021. Accessed: 2024-09-30.
- [59] A. Hidaka. Formation mechanisms of insoluble cs particles observed in kanto district four days after fukushima daiichi npp accident. *Journal of Nuclear Science and Technology*, 56(9-10):831–841, 2019.
- [60] A. Hidaka. Identification of carbon in glassy cesium-bearing microparticles using electron microscopy and formation mechanisms of the microparticles. *Nuclear Technology*, 208(2):318–334, 2022.
- [61] L. Zheng, B. Yan, B. Peng, H. Li, Z. Jiang, and S. Ueda. A proposed formation mechanism of the type-a radiocaesium-bearing microparticles released from units 2/3 during the fukushima daiichi nuclear power plant accident. *Journal of Nuclear Materials*, 563:153623, 2022.
- [62] H. Laffolley, C. Journeau, and B. Grambow. Simulant molten core–concrete interaction experiments in view of understanding fukushima daiichi nuclear power station cs-bearing particles generation mechanism. *Scientific Reports*, 14(1):6611, Mar 2024.
- [63] H. Hagiwara, H. Funaki, N. Shiribiki, M. Kanno, and Y. Sanada. Characterization of radiocesium-bearing microparticles with different morphologies in soil around the fukushima daiichi nuclear power plant. *Journal of Radioanalytical and Nuclear Chemistry*, 331(1):415–426, Jan 2022.
- [64] Dürr Ndt. HD-CR 35 NDT – Installation and operating instructions. https://www.duerr-ndt.com/files/downloads/hd-cr_35_ndt/manual/9000-608-130_2206V004_en.pdf. Accessed: 2024-10-08.
- [65] Dürr Ndt. Imaging Plates For Computed Radiography. https://www.duerr-ndt.de/files/downloads/imaging_plates/literature/WPR0100038_NDT_Imaging_Plates.pdf. Accessed: 2024-10-08.

- [66] PerkinElmer Inc. Cyclone® Plus Storage Phosphor System: The Only Personal Radiometric Phosphor Imager for Quantitative Filmless Autoradiography. https://resources.perkinelmer.com/corporate/content/relatedmaterials/productnotes/prd_cycloneplusstoragephosphor.pdf. Accessed: 2024-10-08.

A Analyses at the USTEM

In this section I want to present a selection of the remaining SEM images and EDX spectra from the examinations at the USTEM that did not make it to any kind of extraction, because the EDX results did not reveal the appropriate elemental composition of the typical CsMPs or other more promising candidates were prioritized. However, even though they are likely not related to CsMPs in any way, it might be helpful to show what kind of other particles are to be expected when investigating these types of samples. Therefore, it might be of assistance when choosing what microparticles to search for.

A.1 Namie Fleece Coat

A.1.1 Sample 1.1.P.1.2 – Part 1/2

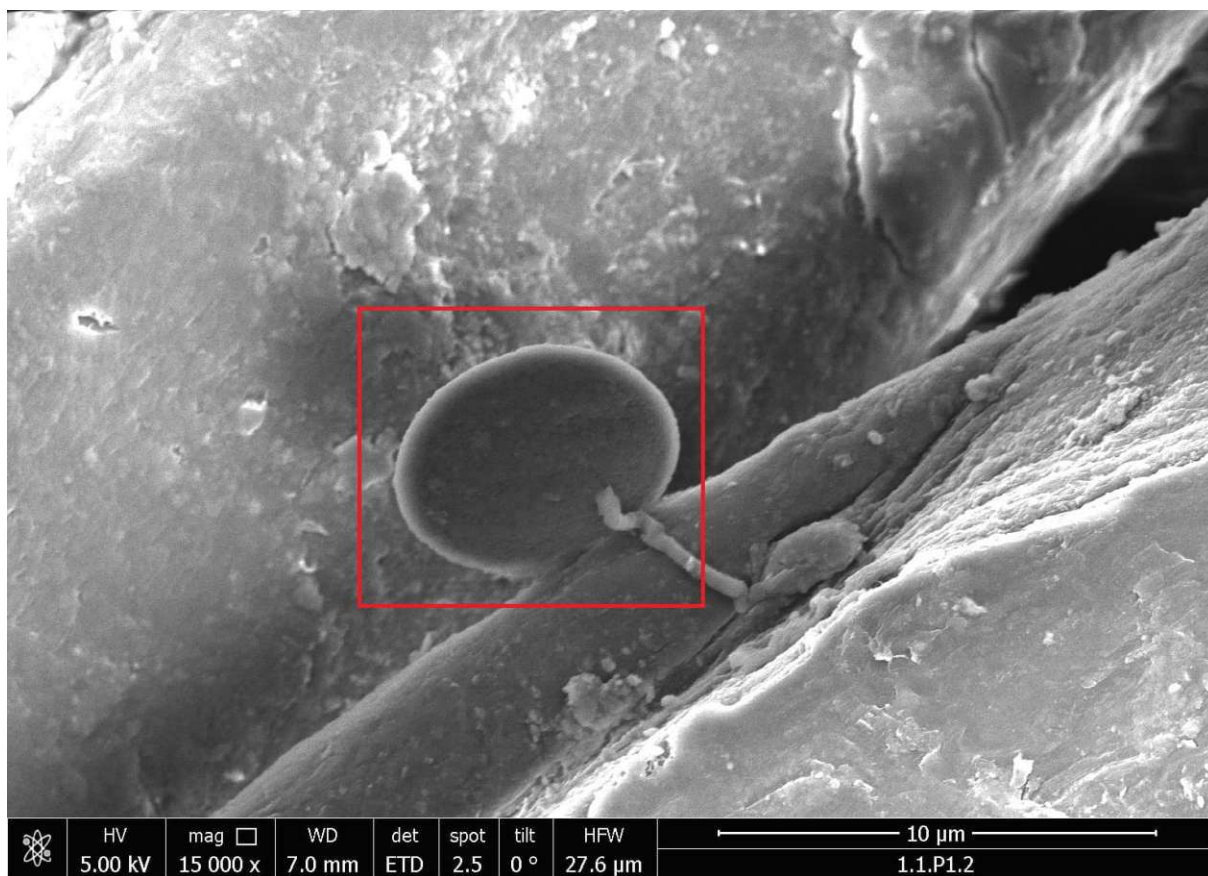


Figure 62: Image of a large oval-shaped structure attached to the side of one of the fleece fibers. The red section was scanned using EDX to determine the elemental composition.

Table 14: EDX results for the oval microparticle in figure 62 (30 s live time measurement).

Element	Mass %	Atomic %	Net Int.	Error %
C K	67.2	73.4	504.4	4.9
O K	31.7	26.0	159.4	8.9
Na K	0.7	0.4	5.5	38.6
Al K	0.3	0.1	3.6	67.2
Si K	0.2	0.1	2.5	71.5

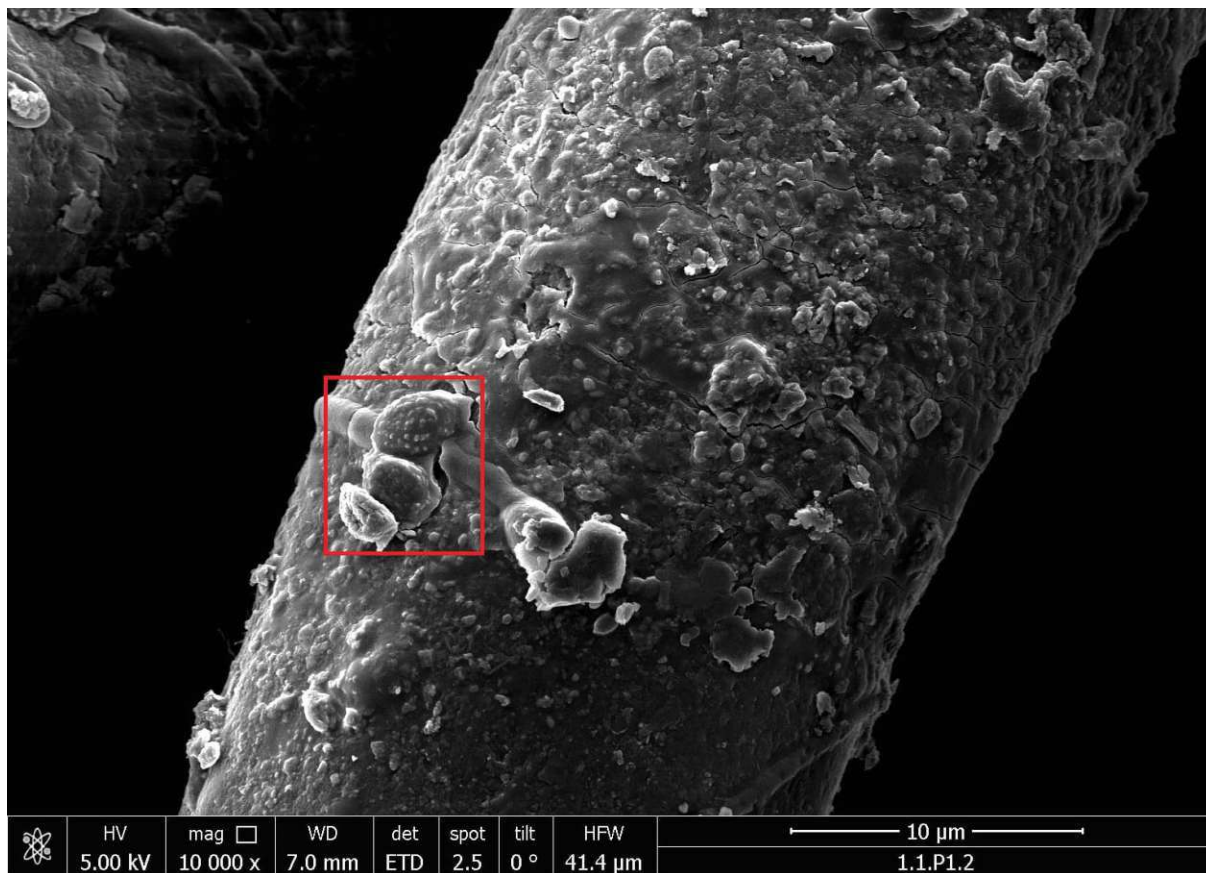


Figure 63: Image of multiple round structures with fibrous parts attached to the side of one of the fleece fibers. The red section was scanned using EDX to determine the elemental composition.

Table 15: EDX results for the micro-structures in figure 63 (30 s live time measurement).

Element	Mass %	Atomic %	Net Int.	Error %
C K	65.6	71.6	344.3	5.2
N K	4.1	3.8	6.2	42.5
O K	29.2	24.0	98.0	10.1
Na K	0.7	0.4	3.7	51.5
Al K	0.5	0.2	4.1	57.4

A.1.2 Sample 1.1.P.1.2 – Part 2/2

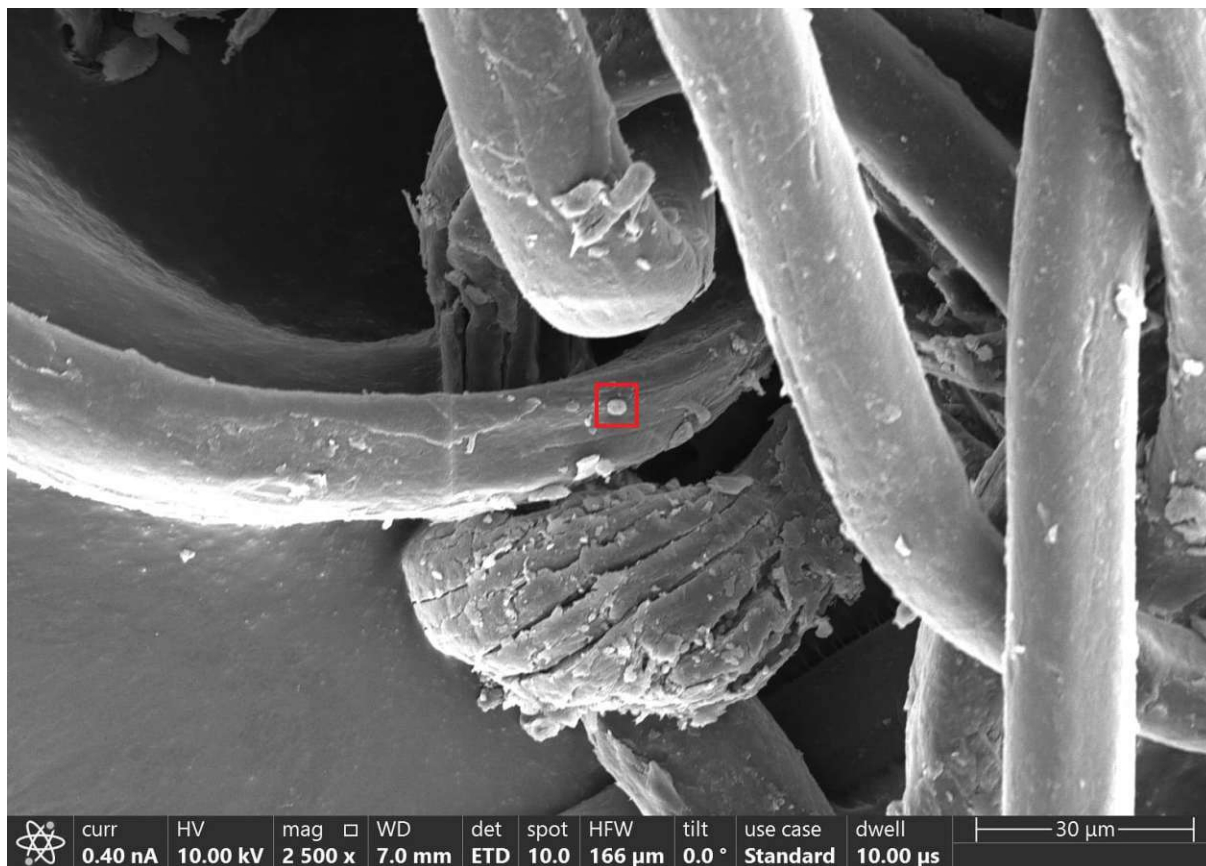


Figure 64: Image of a spherical microparticle on one of the fleece fibers. The red section was scanned using EDX to determine the elemental composition.

Table 16: EDX results for the spherical microparticle in figure 64.

	Mass %	Mass % Error	Atom %	Atom % Error
C K	6.8	±0.2	35.9	±1.3
O K	4.9	±0.2	19.7	±1.0
Al K	0.4	±0.0	1.0	±0.1
Si K	0.3	±0.1	0.7	±0.1
Ca K	4.2	±0.1	6.6	±0.2
Ti K	0.5	±0.1	0.7	±0.2
Fe K	0.7	±0.2	0.9	±0.2
Cu K	2.7	±0.3	2.7	±0.3
Pd L	22.3	±0.7	13.4	±0.4
Au L	57.1	±2.1	18.5	±0.7

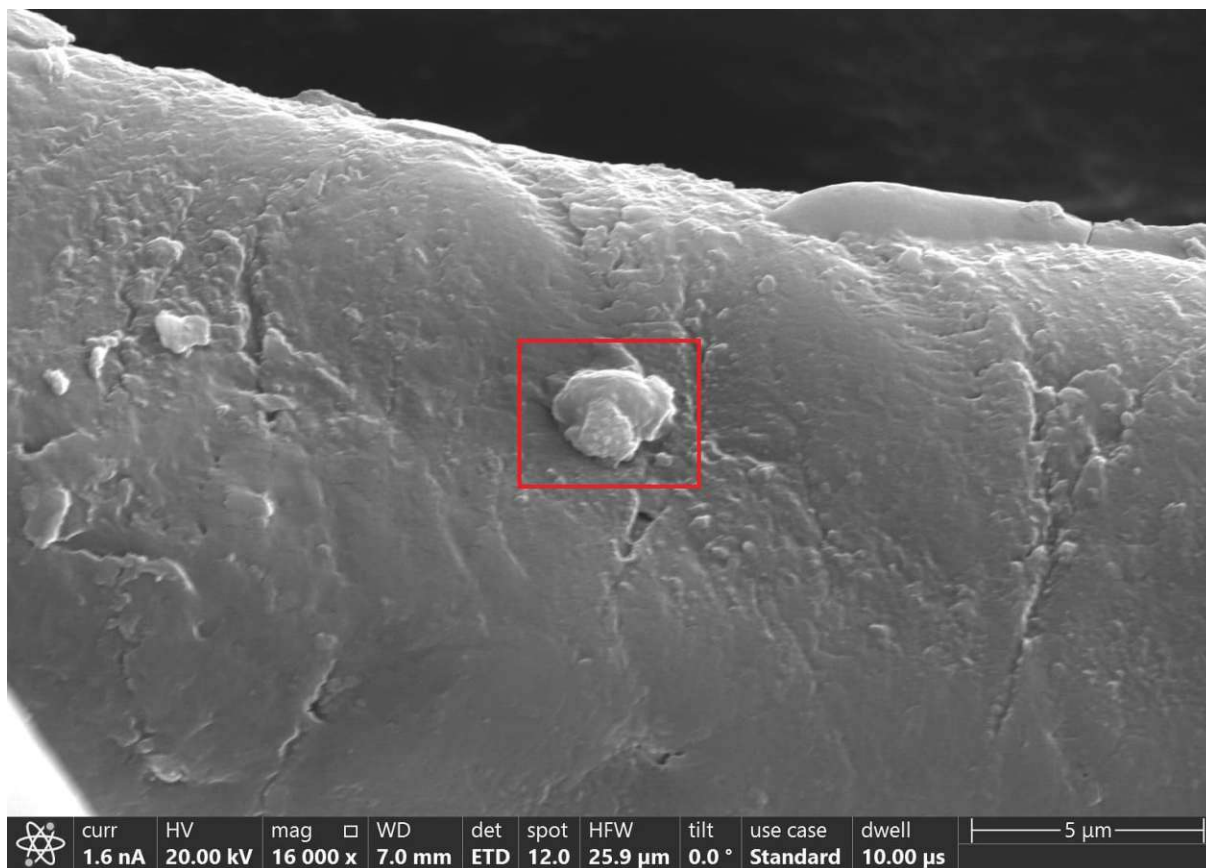


Figure 65: Image of an irregularly rounded structure on one of the fleece fibers. The red section was scanned using EDX to determine the elemental composition.

Table 17: EDX results for the irregularly rounded microparticle in figure 65.

	Mass %	Mass % Error	Atom %	Atom % Error
C K	35.5	±0.4	47.7	±0.6
N K	14.0	±0.8	16.1	±0.9
O K	32.0	±0.4	32.3	±0.4
Na K	2.3	±0.1	1.6	±0.0
Al K	0.1	±0.0	0.1	±0.0
Cl K	0.4	±0.0	0.2	±0.0
K K	0.7	±0.0	0.3	±0.0
Ca K	0.5	±0.0	0.2	±0.0
Ti K	0.2	±0.0	0.1	±0.0
Fe K	0.1	±0.0	0.0	±0.0
Cu K	0.4	±0.1	0.1	±0.0
Pd L	4.1	±0.1	0.6	±0.0
Au L	9.5	±0.4	0.8	±0.0

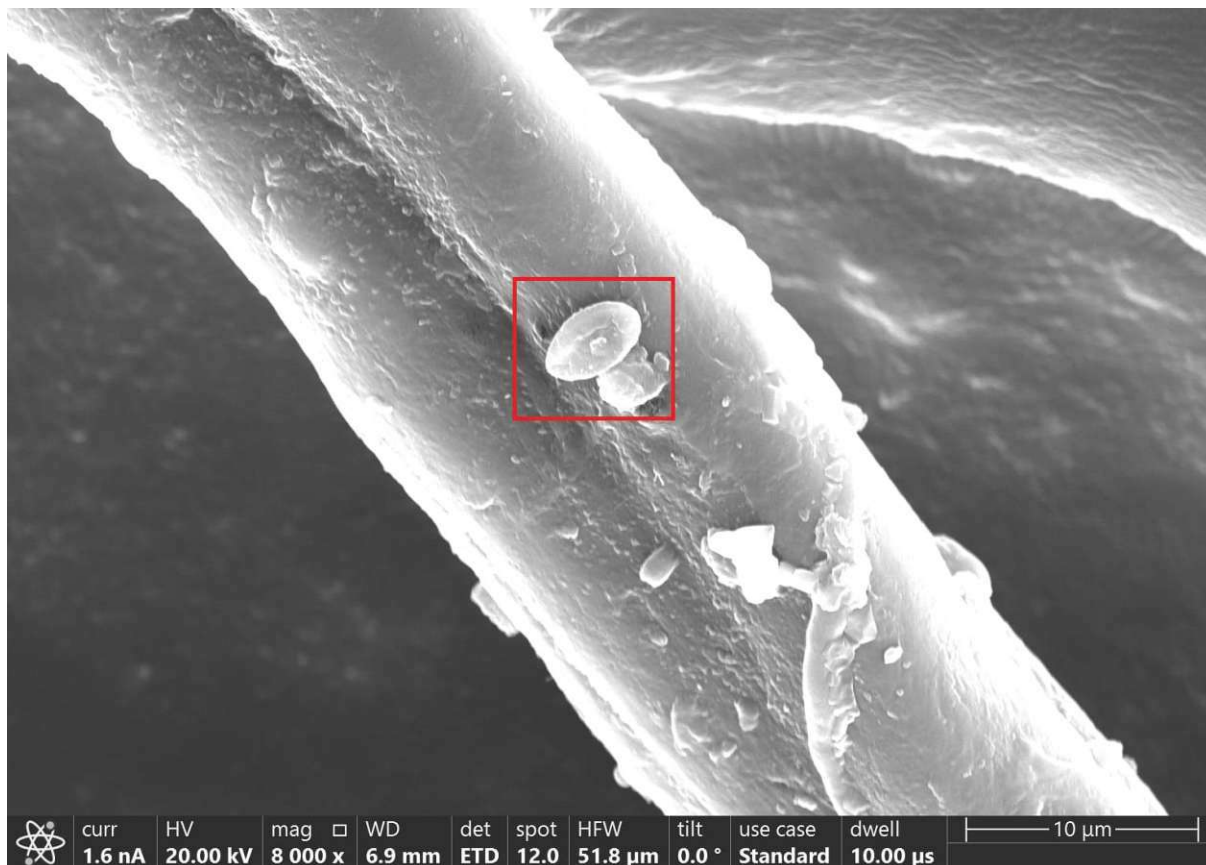


Figure 66: Image of an ellipsoidal microparticle on one of the fleece fibers. The red section was scanned using EDX to determine the elemental composition.

Table 18: EDX results for the ellipsoidal microparticle in figure 66.

	Mass %	Mass % Error	Atom %	Atom % Error
C K	35.3	±0.3	56.3	±0.4
N K	10.0	±0.9	13.7	±1.2
O K	20.3	±0.4	24.4	±0.5
Na K	0.8	±0.0	0.7	±0.0
Mg K	0.2	±0.0	0.2	±0.0
Al K	0.5	±0.0	0.3	±0.0
Si K	0.3	±0.0	0.2	±0.0
Ca K	0.8	±0.1	0.4	±0.0
Ti K	0.4	±0.0	0.2	±0.0
Pd L	8.0	±0.3	1.4	±0.0
Au L	23.4	±0.9	2.3	±0.1

A.1.3 Sample F.1.3.1.3.1

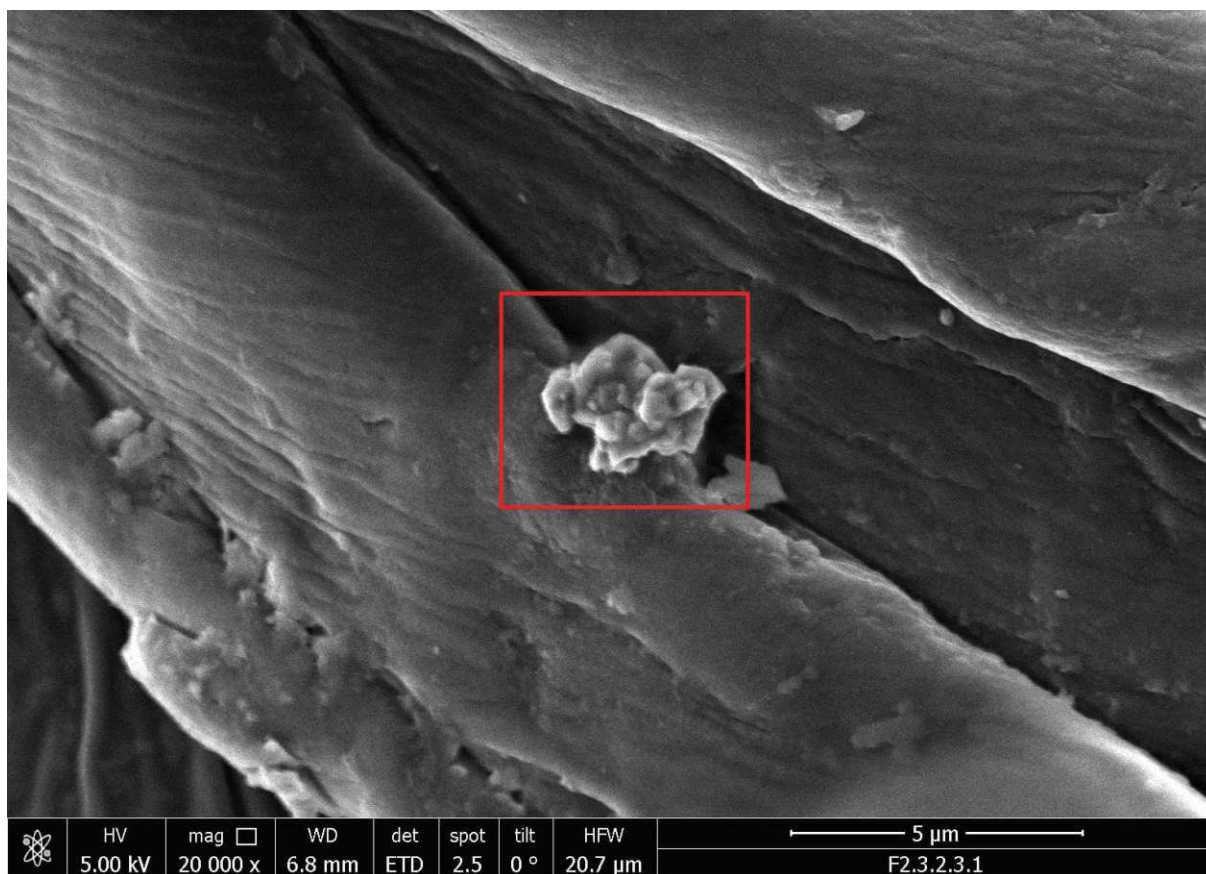


Figure 67: Image of a largely irregular, jagged microparticle on a fleece fiber. The red section was scanned using EDX to determine the elemental composition.

Table 19: EDX results for the largely irregular, jagged microparticle in figure 67 (30 s live time measurement).

Element	Mass %	Atomic %	Net Int.	Error %
C K	24.2	41.9	37.6	5.0
O K	23.5	30.5	20.8	13.0
Al K	1.4	1.1	4.0	33.2
Si K	0.5	0.4	1.7	67.5
Ca K	50.4	26.1	79.1	5.3

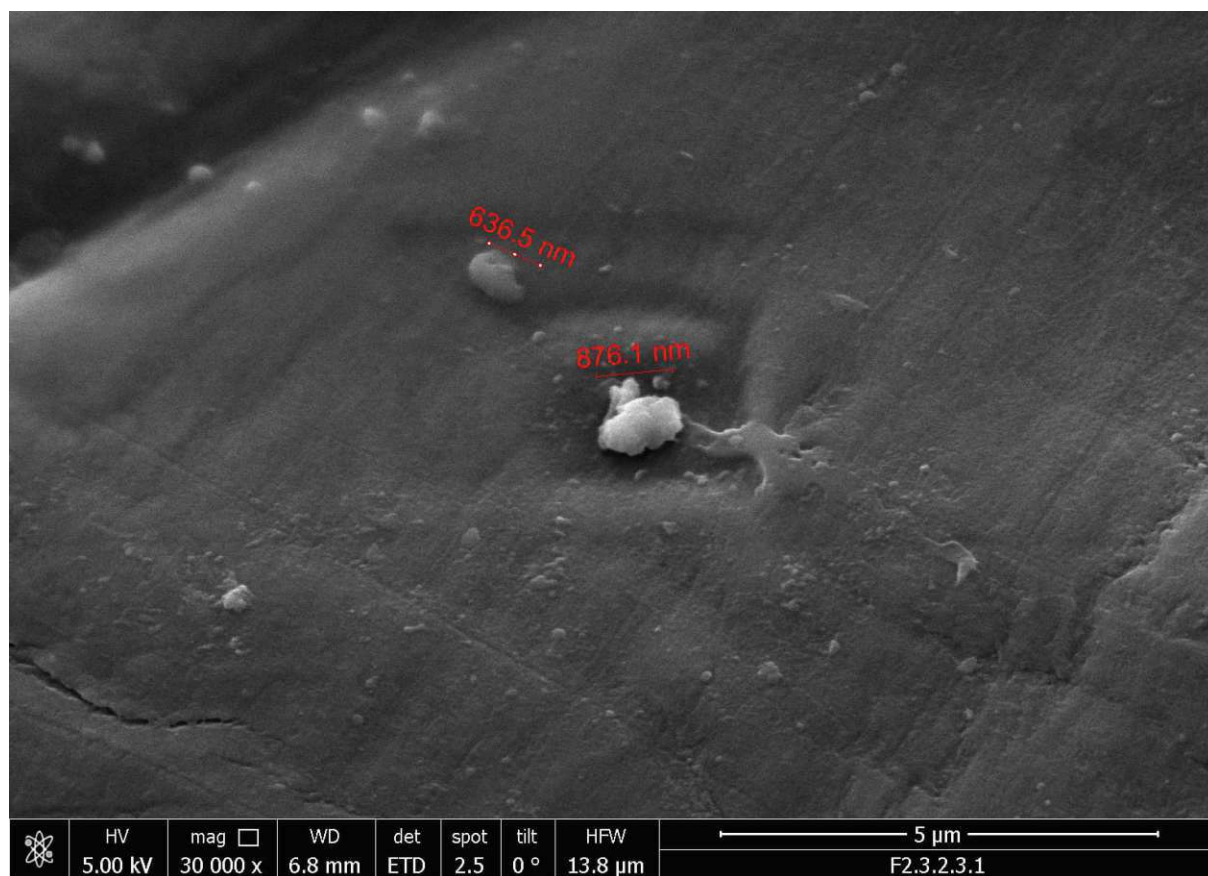


Figure 68: Image of two small and irregular microparticles on a fleece fiber.

Table 20: EDX results for the two small and irregular microparticles in figure 68 (30 s live time measurement). Due to the small size of the particles, this measurement is likely biased to a large degree towards the fleece fiber in the background.

Element	Mass %	Atomic %	Net Int.	Error %
C K	60.5	66.9	304.5	4.7
N K	3.1	2.9	4.9	36.0
O K	36.0	29.9	126.4	8.4
Al K	0.5	0.2	3.9	36.5

A.1.4 Sample 1.4.P.1.1.1

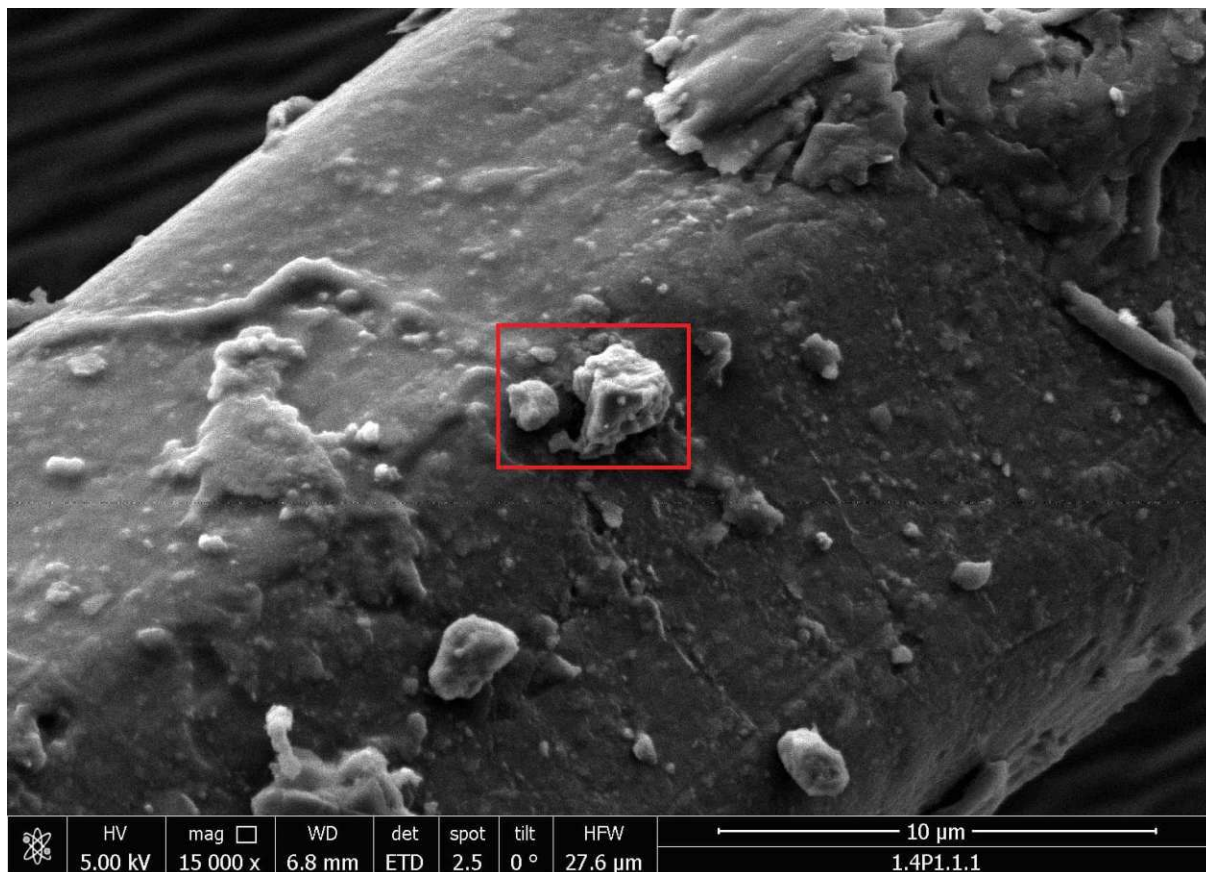


Figure 69: Image of a couple of irregular microparticles, some are rounded, on a fleece fiber with one fairly large prominent particle in the middle. The red section was scanned using EDX to determine the elemental composition.

Table 21: EDX results of the fairly large microparticle in figure 69 (30 s live time measurement).

Element	Mass %	Atomic %	Net Int.	Error %
C K	50.5	60.8	557.7	2.4
O K	38.0	34.4	445.9	7.2
Al K	4.4	2.4	105.7	5.0
Si K	1.9	1.0	49.4	9.1
P K	0.8	0.4	15.4	22.3
Fe K	4.4	1.1	31.6	14.1

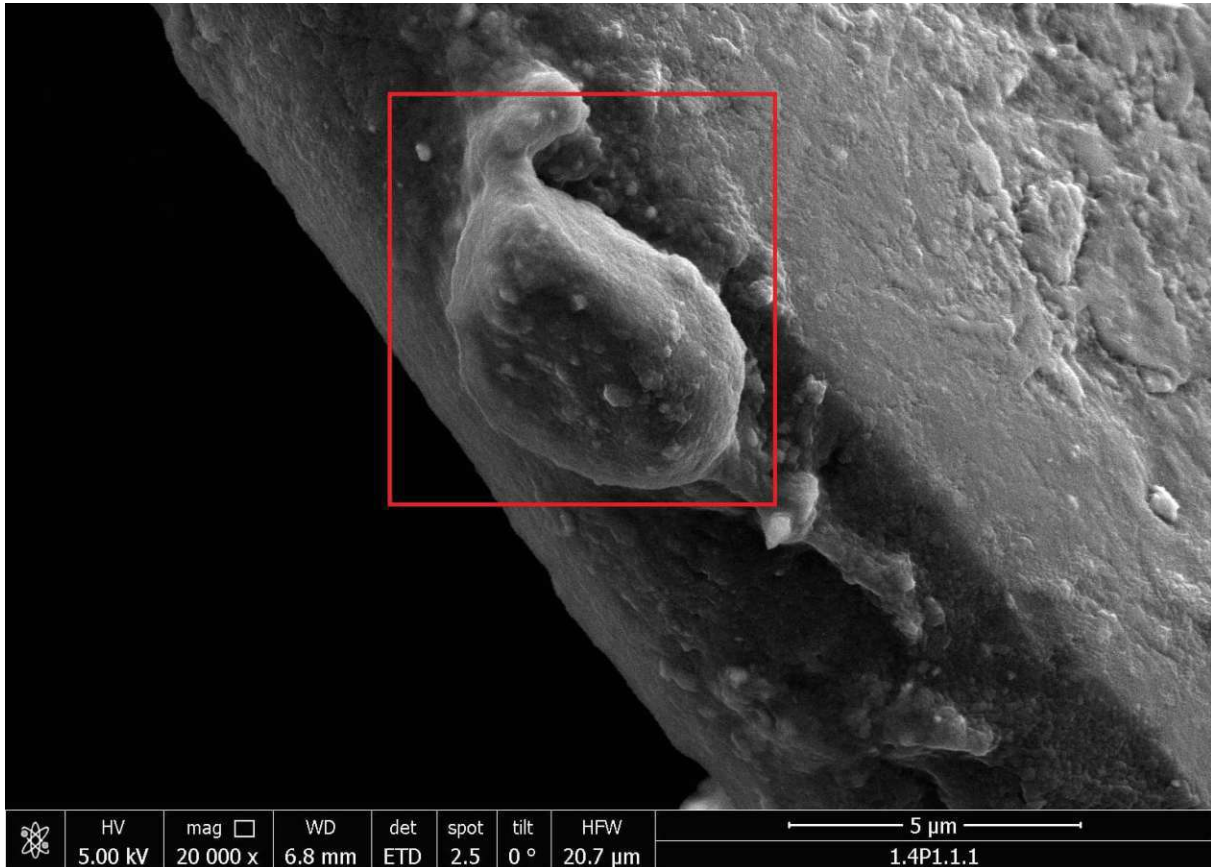


Figure 70: Image of a rounded particulate structure that is fused to the fleece fiber. The red section was scanned using EDX to determine the elemental composition, however, the measurement was not completed or no EDX data was saved to save on time. In that case, the outcome was clearly visible to not be part of a CsMP.

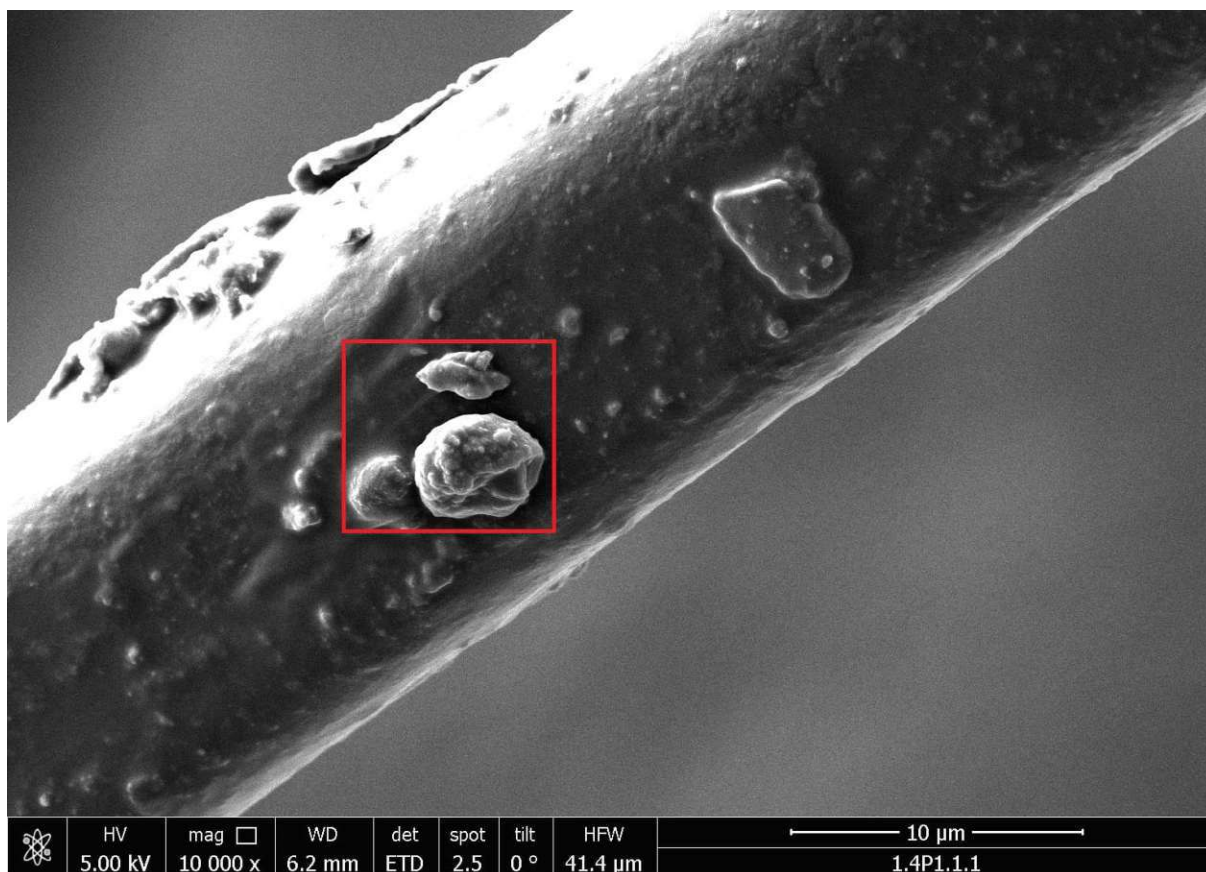


Figure 71: Image of a couple of irregular microparticles, with one prominent rounded particle sitting next to much smaller ones. The red section was scanned using [EDX](#) to determine the elemental composition, however, the measurement was not completed or no EDX data was saved to save on time. In that case, the outcome was clearly visible to not be part of a [CsMP](#).

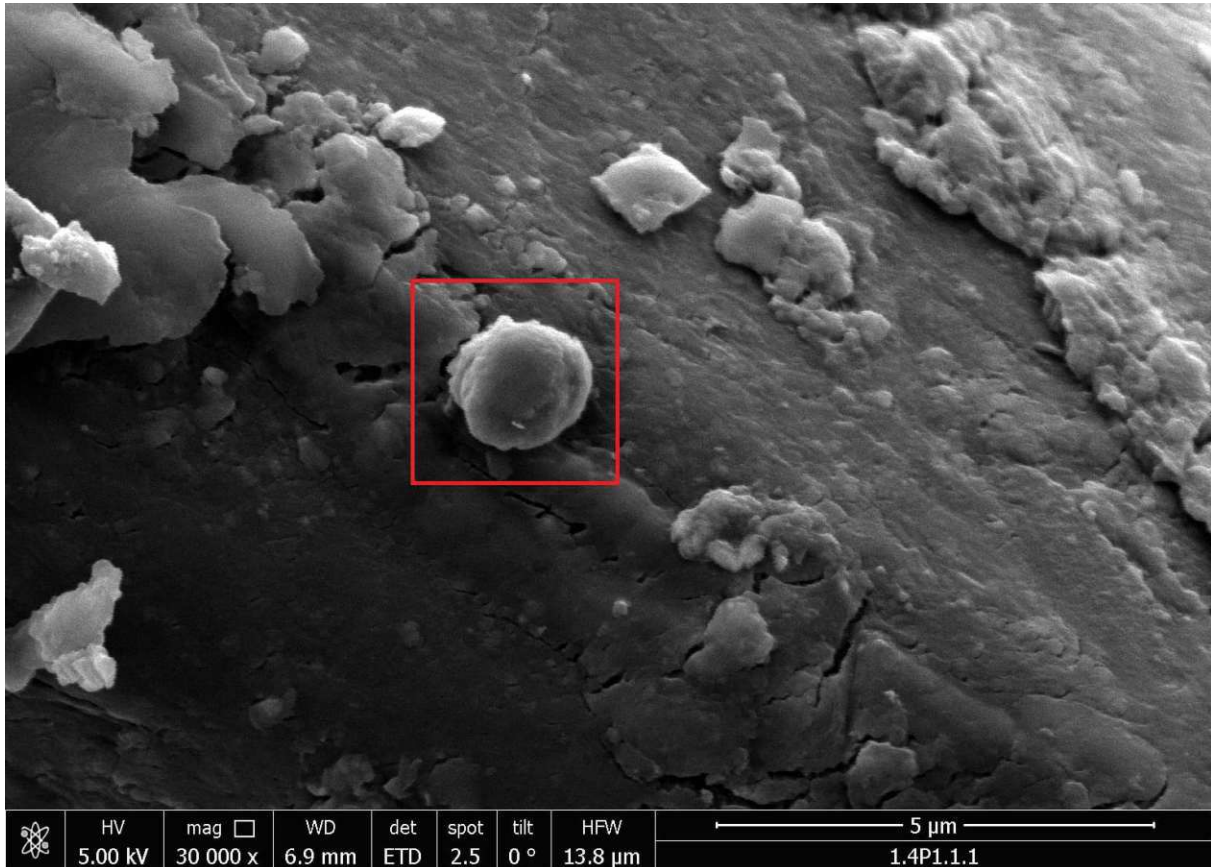


Figure 72: Image of a single fairly spherical microparticle that has been found amongst a field of flakes on the fiber. The red section was scanned using EDX to determine the elemental composition, however, the measurement was not completed or no EDX data was saved to save on time. In that case, the outcome was clearly visible to not be part of a CsMP.

A.1.5 Sample 1.4.P.1.1.2

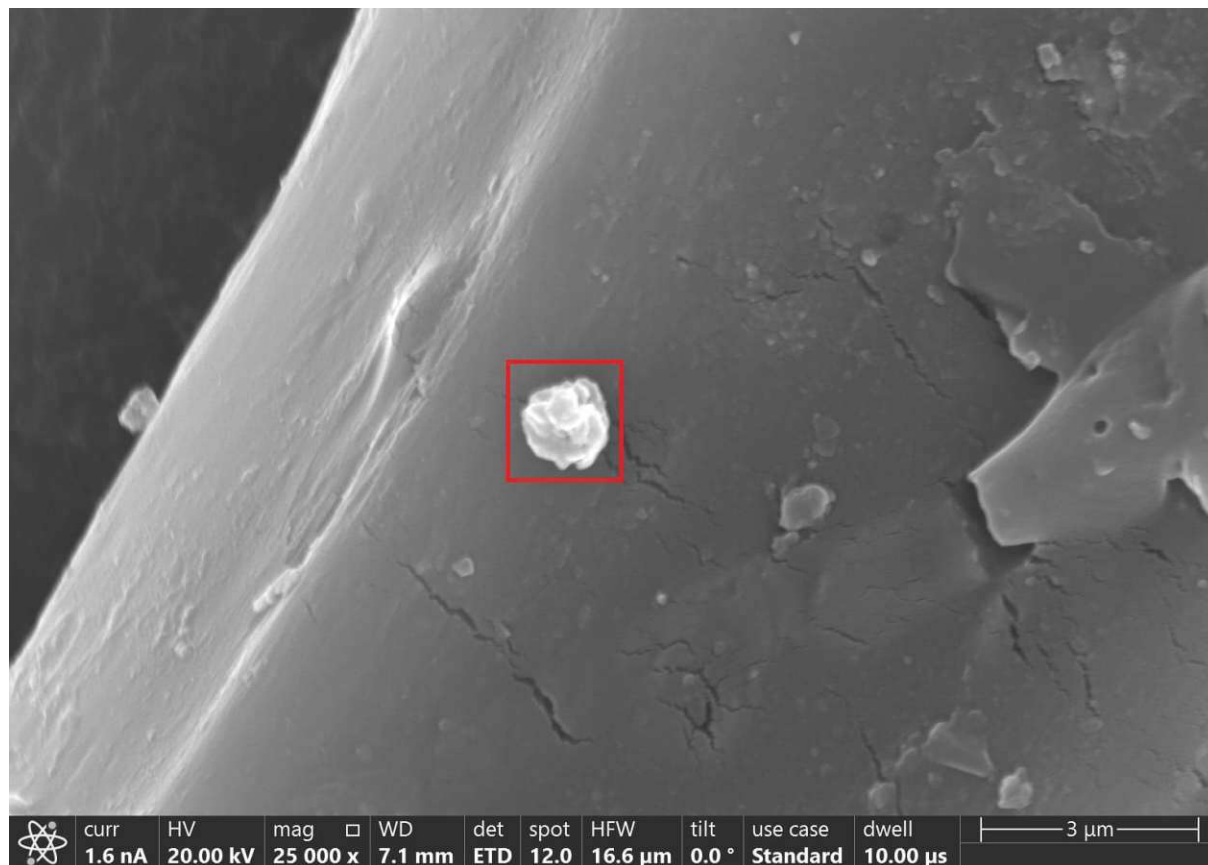


Figure 73: Image of a single irregular microparticle that stands out easily from the rest of its surroundings. The red section was scanned using EDX to determine the elemental composition.

Table 22: EDX results of the bright irregular microparticle in figure 73.

	Mass %	Mass % Error	Atom %	Atom % Error
C K	32.7	±0.2	57.7	±0.3
O K	23.1	±0.3	30.6	±0.4
Al K	0.2	±0.0	0.1	±0.0
Si K	8.3	±0.1	6.3	±0.1
Cl K	0.4	±0.0	0.2	±0.0
Ti K	0.2	±0.0	0.1	±0.0
Cu K	0.7	±0.1	0.2	±0.0
Pd L	10.9	±0.3	2.2	±0.1
Au L	23.4	±1.1	2.5	±0.1

A.1.6 Sample C.2.1.1.2

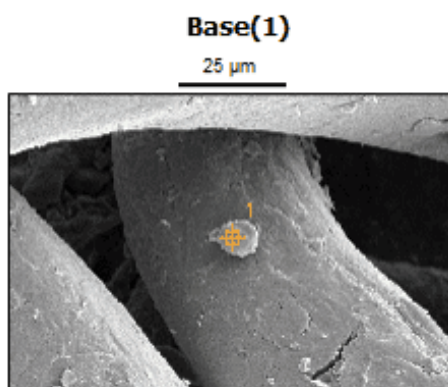


Figure 74: Image of a large spherical microparticle hidden in between a number of fleece fibers. The orange cross marks the point that was targeted for the EDX measurement.

Table 23: EDX results of the large spherical microparticle in figure 74.

	Mass %	Mass % Error	Atom %	Atom % Error
C K	3.3	± 0.1	25.8	± 0.5
O K	1.4	± 0.2	8.1	± 1.0
Na K	0.4	± 0.1	1.7	± 0.4
Al K	0.5	± 0.1	1.9	± 0.5
Pd L	42.0	± 2.9	37.4	± 2.6
Au M	52.4	± 2.3	25.1	± 1.1

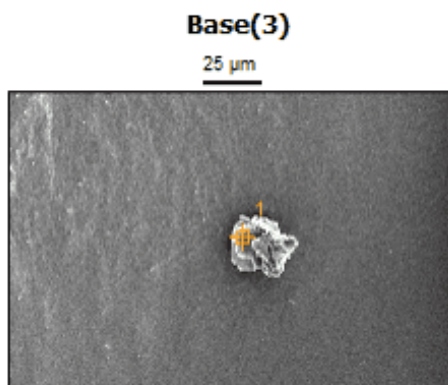
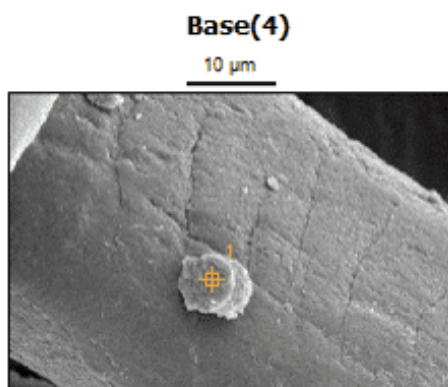


Figure 75: Image of a large irregularly jagged microparticle on one of the fleece fibers. The orange cross marks the point that was targeted for the EDX measurement.

Table 24: EDX results of the large jagged microparticle in figure 75.

	Mass %	Mass % Error	Atom %	Atom % Error
C K	1.8	±0.1	16.4	±0.5
O K	0.9	±0.1	6.4	±0.6
Mg K	0.3	±0.1	1.5	±0.5
Pd L	43.3	±2.9	45.3	±3.1
Au M	53.7	±2.2	30.4	±1.3

**Figure 76:** Image of a fairly large spherical microparticle on one of the fleece fibers. The orange cross marks the point that was targeted for the EDX measurement.**Table 25:** EDX results of the fairly large spherical microparticle on one of the fleece fibers in figure 76.

	Mass %	Mass % Error	Atom %	Atom % Error
C K	4.1	±0.2	28.3	±1.1
O K	3.2	±0.2	16.4	±1.1
Mg K	0.4	±0.1	1.3	±0.4
Pd L	43.6	±4.6	33.7	±3.5
Au M	48.6	±2.1	20.3	±0.9

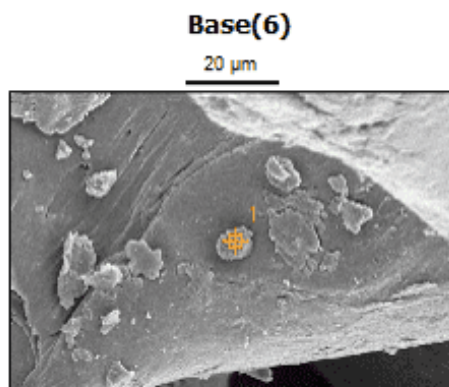


Figure 77: Image of an interesting round flake amongst others, it is unclear if the particle was actually more three dimensional or really just a flat flake. The orange cross marks the point that was targeted for the [EDX](#) measurement.

Table 26: [EDX](#) results of the round flake on one of the fleece fibers in figure 77.

	Mass %	Mass % Error	Atom %	Atom % Error
C K	4.4	± 0.1	24.9	± 0.5
N K	2.0	± 0.4	9.9	± 1.9
O K	3.8	± 0.3	16.2	± 1.1
Ti L	5.7	± 3.4	8.1	± 4.9
Pd L	39.5	± 4.0	25.4	± 2.6
Au M	44.6	± 1.8	15.5	± 0.6

A.2 Passive Air Samplers

A.2.1 Sample PS.B.P.1

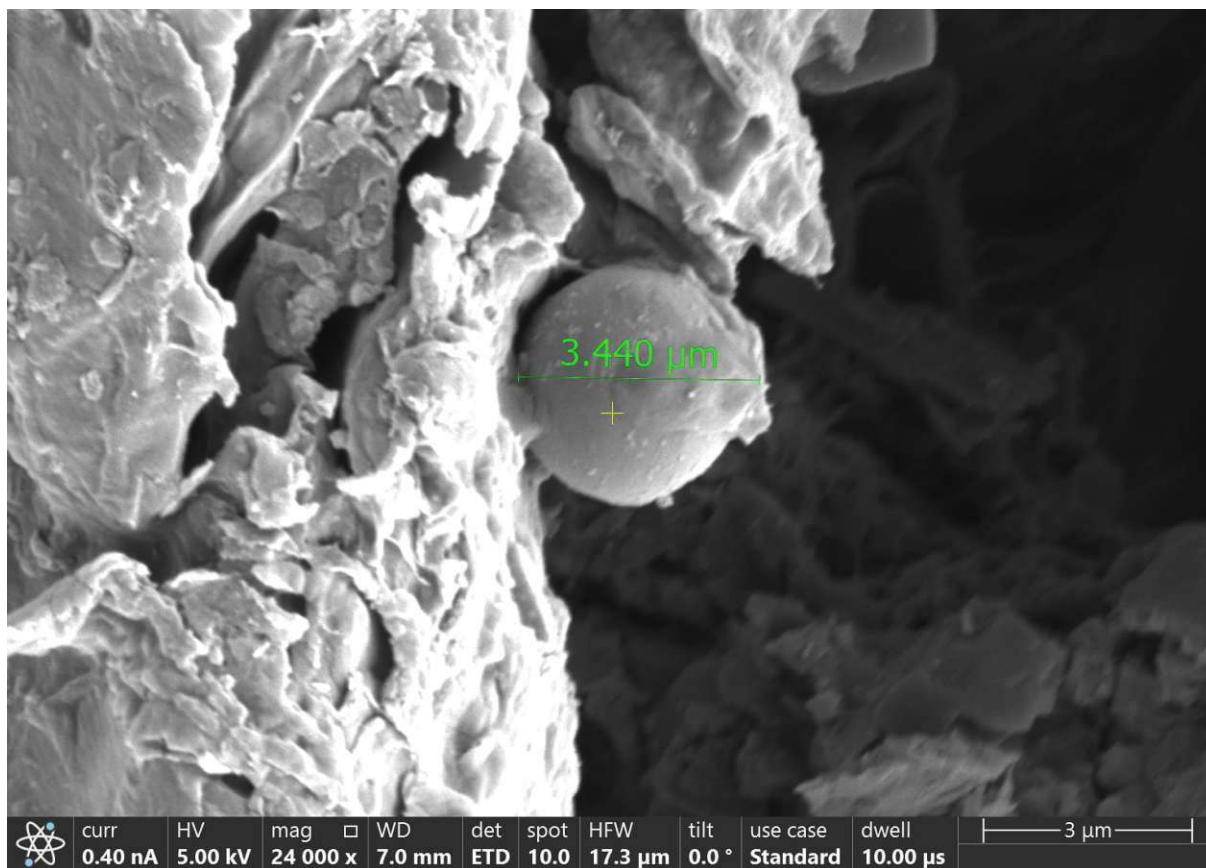


Figure 78: Image of a promising spherical microparticle, it seems to be fused or stuck to the other debris around it. Morphologically speaking, this particle would be another candidate for a CsMP.

Table 27: EDX results of the spherical particle amongst the debris in figure 78. It is quite rich in Al with less of an Si content and no other of the expected elements, which is why it was not extracted.

	Mass %	Mass % Error	Atom %	Atom % Error
C K	4.1	±0.1	15.3	±0.3
N K	2.5	±0.3	7.8	±0.9
O K	13.5	±0.2	37.7	±0.7
Al K	6.5	±0.2	10.8	±0.4
Si K	3.6	±0.2	5.8	±0.3
Pd L	35.1	±2.0	14.8	±0.8
Au M	34.6	±1.4	7.8	±0.3

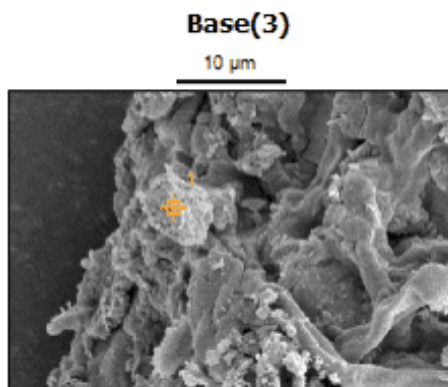


Figure 79: Image of a quite inconspicuous jagged microparticle amongst the other debris. The orange cross marks the point that was targeted for the EDX measurement.

Table 28: EDX results of the inconspicuous jagged microparticle amongst the debris in figure 79. Unexpectedly, it was quite rich in Si, despite its nondescript morphology.

	Mass %	Mass % Error	Atom %	Atom % Error
C K	2.2	± 0.1	11.4	± 0.3
O K	9.9	± 0.3	38.9	± 1.0
Mg K	0.2	± 0.1	0.4	± 0.3
Al K	1.7	± 0.2	3.9	± 0.5
Si K	4.4	± 0.3	9.8	± 0.7
Pd L	34.9	± 3.3	20.6	± 1.9
Au M	46.8	± 1.5	14.9	± 0.5

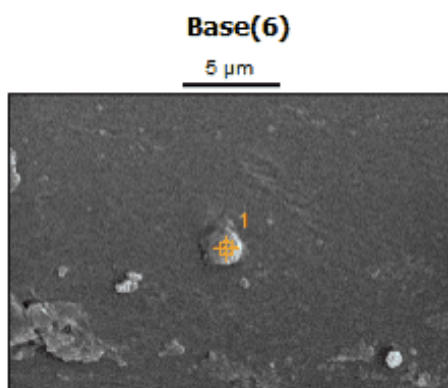


Figure 80: Image of a lone spherical microparticle adhering directly to the glue of the sample holder, away from most of the other debris. The orange cross marks the point that was targeted for the EDX measurement.

Table 29: EDX results of the lone spherical microparticle in figure 80. This one had particularly high Ti contents.

	Mass %	Mass % Error	Atom %	Atom % Error
C K	4.0	±0.1	24.5	±0.4
O K	2.5	±0.2	11.4	±1.0
Na K	0.7	±0.1	2.3	±0.4
Ti L	14.0	±2.5	21.4	±3.8
Pd L	35.5	±3.0	24.4	±2.1
Au M	43.3	±1.4	16.1	±0.5

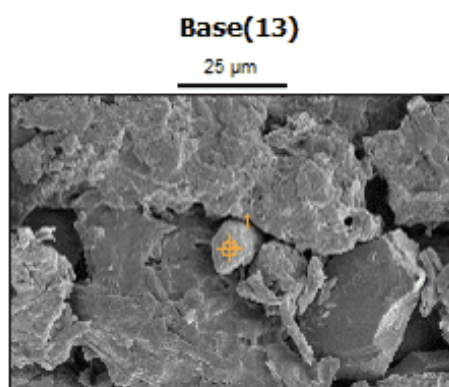


Figure 81: Image of another quite inconspicuous edged microparticle in between all of the other debris from the dirt particle. The orange cross marks the point that was targeted for the EDX measurement.

Table 30: EDX results of the quite inconspicuous edged microparticle in figure 81. This one likely contains a large amount of salt (NaCl) in accordance with the high amounts of Na and Cl.

	Mass %	Mass % Error	Atom %	Atom % Error
C K	2.2	±0.0	12.7	±0.2
O K	1.2	±0.2	5.1	±0.8
Na K	8.1	±0.2	24.3	±0.6
Cl K	9.8	±0.9	19.0	±1.7
Pd L	38.4	±2.7	24.8	±1.7
Au M	40.3	±1.4	14.1	±0.5

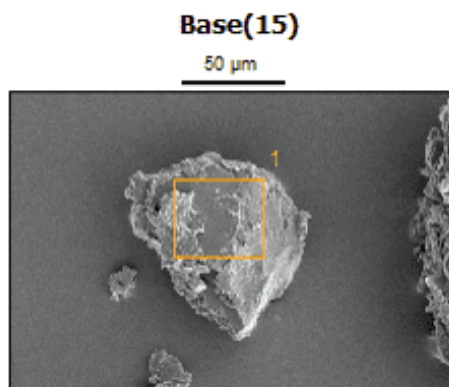


Figure 82: Image of a huge, quite edged microparticle besides the other debris. The orange cross marks the point that was targeted for the EDX measurement.

Table 31: EDX results of the huge, quite edged microparticle in figure 82. It contained a significant amount of Si with some of the more common Al and, interestingly, traces of Mg too.

	Mass %	Mass % Error	Atom %	Atom % Error
C K	2.2	± 0.1	10.8	± 0.3
O K	10.1	± 0.3	37.6	± 1.0
Mg K	1.9	± 0.2	4.7	± 0.4
Al K	1.5	± 0.1	3.4	± 0.3
Si K	4.7	± 0.3	9.9	± 0.6
Pd L	37.6	± 3.3	21.0	± 1.9
Au M	42.0	± 1.5	12.7	± 0.5